### Microscopic Studies of Quantum Phase Transitions in Optical Lattices

A dissertation presented by

Waseem S. Bakr

to

The Department of Physics
in partial fulfillment of the requirements
for the degree of
Doctor of Philosophy
in the subject of

Physics

Harvard University
Cambridge, Massachusetts
May 2011

©2011 - Waseem S. Bakr

All rights reserved.

Thesis advisor Author

Professor Markus Greiner

Waseem S. Bakr

Microscopic Studies of Quantum Phase Transitions in Optical Lattices

Abstract

In this thesis, I report on experiments that microscopically probe quantum phase transitions of ultracold atoms in optical lattices. We have developed a "quantum gas microscope" that allowed, for the first time, optical imaging and manipulation of single atoms in a quantum-degenerate gas on individual sites of an optical lattice. This system acts as a quantum simulator of strongly correlated materials, which are currently the subject of intense research because of the technological potential of high— $T_c$  superconductors and spintronic materials. We have used our microscope to study the superfluid to Mott insulator transition in bosons and a magnetic quantum phase transition in a spin system.

In our microscopic study of the superfluid-insulator transition, we have characterized the on-site number statistics in a space- and time-resolved manner. We observed Mott insulators with fidelities as high as 99%, corresponding to entropies of  $0.06k_B$  per particle. We also measured local quantum dynamics and directly imaged the shell structure of the Mott insulator.

I report on the first quantum magnetism experiments in optical lattices. We have realized a quantum Ising chain in a magnetic field, and observed a quantum phase transition between a paramagnet and antiferromagnet. We achieved strong

iii

Abstract

spin interactions by encoding spins in excitations of a Mott insulator in a tilted lattice. We detected the transition by measuring the total magnetization of the system across the transition using in-situ measurements as well as the Néel ordering in the antiferromagnetic state using noise-correlation techniques. We characterized the dynamics of domain formation in the system. The spin mapping introduced opens up a new path to realizing more exotic states in optical lattices including spin liquids and quantum valence bond solids.

As our system sizes become larger, simulating their physics on classical computers will require exponentially larger resources because of entanglement build-up near a quantum phase transition. We have demonstrated a quantum simulator in which all degrees of freedom can be read out microscopically, allowing the simulation of quantum many-body systems with manageable resources. More generally, the ability to image and manipulate individual atoms in optical lattices opens an avenue towards scalable quantum computation.

#### Contents

		e Page	
		tract	ii
	Tabl	e of Contents	7
	Ackı	nowledgments	vii
	Ded	ication	X
1	Intr	roduction	]
2	Qua	antum phase transitions: a condensed matter perspective	8
	2.1	Classical vs. quantum phase transitions	8
	2.2	Quantum phase transitions in Ising models	1.
	2.3	The superfluid to Mott phase transition in the Bose-Hubbard model .	16
	2.4	Critical phenomena	20
3	Ultı	cacold bosons in optical lattice potentials	22
	3.1	Bose-Einstein condensates in the weakly interacting regime	2
	3.2	Bose-Einstein condensates in the strongly interacting regime	25
		3.2.1 Optical dipole potentials	26
		3.2.2 Theory of non-interacting atoms in an optical lattice	29
		3.2.3 Mapping onto the Bose-Hubbard model	32
		3.2.4 Shell structure in the presence of harmonic confinement	34
4	Exp	perimental apparatus and techniques	36
	4.1	Preparing the Bose-Einstein condensate	3
	4.2	Creation of two dimensional condensates using surface traps	3
		4.2.1 Evanescent wave surface trap	39
		4.2.2 Two-stage standing wave trap	42
		4.2.3 Theory of two dimensional condensates	42
	4.3	Using a dimple for producing small cold clouds	4
	4.4	Incoherent light sources for producing clean optical potentials	4!
	4.5	Quantum gas microscopy	4

*Contents* vi

Mag 6.1 6.2 6.3 6.4 6.5 6.6	Simula 6.1.1 6.1.2 6.1.3 6.1.4 6.1.5 6.1.6 6.1.7 Obser 6.2.1 6.2.2 6.2.3 Doma Prepar 6.4.1 Prospe	quantum phase transition in a spin chain ating an antiferromagnetic Ising chain in an optical lattice  Mapping onto the spin model  The paramagnetic and antiferromagnetic phases  Second order hopping processes  Quantum phase transition and the phase diagram  Extracting spin observables  Exact diagonalization studies of small chains  Beyond the Ising Hamiltonian  vation of the phase transition  In-situ observation of the phase transition and its reversibility  Noise correlation detection of long-range order  Single-site study of the transition  in formation and adiabaticity timescales  ration of the highest energy state  Entropy and thermalization in the spin chains  ects for studying criticality  pulation of individual spins	87 89 92 94 96 98 100 103 104 107 108 110 111 115 117 118 120 121
6.1 6.2 6.3 6.4 6.5	Simula 6.1.1 6.1.2 6.1.3 6.1.4 6.1.5 6.1.6 6.1.7 Obser 6.2.1 6.2.2 6.2.3 Doma Prepar 6.4.1 Prospe	Mapping onto the spin model The paramagnetic and antiferromagnetic phases Second order hopping processes Quantum phase transition and the phase diagram Extracting spin observables Exact diagonalization studies of small chains Beyond the Ising Hamiltonian vation of the phase transition In-situ observation of the phase transition and its reversibility Noise correlation detection of long-range order Single-site study of the transition in formation and adiabaticity timescales ration of the highest energy state Entropy and thermalization in the spin chains ects for studying criticality	89 92 94 96 98 100 103 104 107 108 110 111 115 117 118
6.1 6.2 6.3 6.4	Simula 6.1.1 6.1.2 6.1.3 6.1.4 6.1.5 6.1.6 6.1.7 Obser 6.2.1 6.2.2 6.2.3 Doma Prepar 6.4.1	Mapping onto the spin model The paramagnetic and antiferromagnetic phases Second order hopping processes Quantum phase transition and the phase diagram Extracting spin observables Exact diagonalization studies of small chains Beyond the Ising Hamiltonian vation of the phase transition In-situ observation of the phase transition and its reversibility Noise correlation detection of long-range order Single-site study of the transition in formation and adiabaticity timescales ration of the highest energy state Entropy and thermalization in the spin chains	89 92 94 96 98 100 103 104 107 108 110 111 115 117
<ul><li>6.1</li><li>6.2</li><li>6.3</li></ul>	Simula 6.1.1 6.1.2 6.1.3 6.1.4 6.1.5 6.1.6 6.1.7 Obser 6.2.1 6.2.2 6.2.3 Doma Prepar	Mapping onto the spin model  The paramagnetic and antiferromagnetic phases  Second order hopping processes  Quantum phase transition and the phase diagram  Extracting spin observables  Exact diagonalization studies of small chains  Beyond the Ising Hamiltonian  vation of the phase transition  In-situ observation of the phase transition and its reversibility  Noise correlation detection of long-range order  Single-site study of the transition  in formation and adiabaticity timescales  ration of the highest energy state	89 92 94 96 98 100 103 104 107 108 110 111 115 117
<ul><li>6.1</li><li>6.2</li><li>6.3</li></ul>	Simula 6.1.1 6.1.2 6.1.3 6.1.4 6.1.5 6.1.6 6.1.7 Obser 6.2.1 6.2.2 6.2.3 Doma	Mapping onto the spin model	89 92 94 96 98 100 103 104 107 108 110 111
6.1	Simula 6.1.1 6.1.2 6.1.3 6.1.4 6.1.5 6.1.6 6.1.7 Obser 6.2.1 6.2.2 6.2.3	Mapping onto the spin model  The paramagnetic and antiferromagnetic phases  Second order hopping processes  Quantum phase transition and the phase diagram  Extracting spin observables  Exact diagonalization studies of small chains  Beyond the Ising Hamiltonian  vation of the phase transition  In-situ observation of the phase transition and its reversibility  Noise correlation detection of long-range order  Single-site study of the transition	89 92 94 96 98 100 103 104 107 108 110
6.1	Simula 6.1.1 6.1.2 6.1.3 6.1.4 6.1.5 6.1.6 6.1.7 Obser 6.2.1 6.2.2	Mapping onto the spin model	89 92 94 96 98 100 103 104 107 108 110
6.1	Simula 6.1.1 6.1.2 6.1.3 6.1.4 6.1.5 6.1.6 6.1.7 Obser 6.2.1	Mapping onto the spin model	89 92 94 96 98 100 103 104 107
6.1	Simula 6.1.1 6.1.2 6.1.3 6.1.4 6.1.5 6.1.6 6.1.7 Observa	Mapping onto the spin model	89 92 94 96 98 100 103 104 107
6.1	Simula 6.1.1 6.1.2 6.1.3 6.1.4 6.1.5 6.1.6 6.1.7	Ating an antiferromagnetic Ising chain in an optical lattice Mapping onto the spin model	89 92 94 96 98 100 103 104
	Simula 6.1.1 6.1.2 6.1.3 6.1.4 6.1.5 6.1.6	Mapping onto the spin model	89 92 94 96 98 100 103
	Simula 6.1.1 6.1.2 6.1.3 6.1.4 6.1.5	Ating an antiferromagnetic Ising chain in an optical lattice Mapping onto the spin model	89 92 94 96 98 100
	Simula 6.1.1 6.1.2 6.1.3 6.1.4	Mapping onto the spin model	89 92 94 96 98
	Simula 6.1.1 6.1.2 6.1.3	Mapping onto the spin model	89 92 94 96
	Simula 6.1.1 6.1.2	ating an antiferromagnetic Ising chain in an optical lattice Mapping onto the spin model	89 92 94
	Simula 6.1.1	ating an antiferromagnetic Ising chain in an optical lattice Mapping onto the spin model	89 92
	Simula	ating an antiferromagnetic Ising chain in an optical lattice	89
	_		
		J	
	5.2.5		83
		· ·	81
			79
			78
<b>0.</b> ∠			75 76
5.2			75
			73
			70
			67 69
1.6			66 67
			65 66
D 61			
4.9	Noise	correlation measurements	62
4.8	Site-re	esolved modulation spectroscopy	59
4.7	Arbitr	rary potential landscapes with spatial light modulators	58
4.6	Image	analysis for extracting the density distribution	56
	4.5.3	Fluorescence imaging of single atoms	51
	4.5.2	Optical lattice projection	50
	4.5.1	High numerical aperture imaging	47
	4.7 4.8 4.9	4.5.3 4.6 Image 4.7 Arbita 4.8 Site-re 4.9 Noise  Microscop 5.1 Numb 5.1.1 5.1.2 5.1.3 5.1.4 5.2 Micros 5.2.1 5.2.2 5.2.3 5.2.4	4.5.3 Fluorescence imaging of single atoms  4.6 Image analysis for extracting the density distribution  4.7 Arbitrary potential landscapes with spatial light modulators  4.8 Site-resolved modulation spectroscopy  4.9 Noise correlation measurements  Microscopy of the superfluid-insulator quantum phase transition  5.1 Number squeezing across the phase transition  5.1.1 Gutzwiller prediction for number squeezing  5.1.2 Parity detection of number squeezing  5.1.3 Squeezing dynamics in the mean-field  5.1.4 Mott insulators at finite temperature  5.2 Microscopic study of the phase transition  5.2.1 Single-site imaging of atom number fluctuations  5.2.2 Thermometry down to zero temperature  5.2.3 Measurement of local adiabaticity timescales  5.2.4 Imaging the Mott insulator shell structure

	••
Contents	V11
Contection	V 11

Bi	bliog	raphy	128
$\mathbf{A}$	$\mathbf{Bey}$	ond hyperfine encoding of spins	145
	A.1	Double well ladder systems	146
	A.2	Encoding spin in vibrational states	148

#### Acknowledgments

It has been a great pleasure to be advised by Markus Greiner over the course of my doctorate. In addition to being an inspiring scientist with a contagious passion and enthusiasm for his work, he is also an exceptional advisor able to achieve the delicate balance between guiding his students and allowing them the freedom to pursue their own ideas. Under his supervision, I have grown as a scientist and as a person, and of course, acquired a small fraction of his intuition for optics along the way.

When I arrived at Harvard, Jonathon Gillen took me under his wing and has been a great mentor ever since. His work ethic and technical expertise were crucial to realizing the quantum gas microscope. I look forward to congratulating him on the new addition to his family soon. I owe a lot of my theoretical knowledge of ultracold gases to Amy Peng. Her methodical approach towards everything from theoretical calculations to data collection provided a thread of organization to a sprawling experiment. I wish her every success in her new research in the life sciences.

I have had the fortune of working with two very talented post-docs: Simon Foelling and Jonathan Simon. Simon brought to the lab much needed expertise in optical lattices and more importantly, taught me how to survive on the ski slopes as a beginner. I am confident the ytterbium experiment he started will produce many ground-breaking results within the next few years. Arriving soon after we imaged the first Mott insulators in a somewhat unreliable apparatus, Jonathan transformed our microscope into a veritable results-churning machine. He also provided a different perspective from quantum optics, and our discussions generated many fruitful ideas.

The apparatus is now in the hands of three very capable graduate students, Eric Tai, Alex Ma and Philipp Preiss. I look forward to hearing about many more exciting

Acknowledgments ix

results as they push the experiment forwards. The members of the fermion lab, Widagdo Setiawan, Kate Wooley-Brown and Florian Huber have made the lab an enjoyable workplace and provided countless memorable and humorous moments. I am also grateful for the contributions and friendship of many visiting students, including Hannes Brachmann, Tobias Schuster, Gregor Jotzu and Dylan Cotta and wish them the best in the doctorates they have started elsewhere.

The work described in this thesis has benefited greatly from collaborations with theorists at Harvard. In particular, I thank Prof. Subir Sachdev and Susanne Pielawa for their theoretical proposals on realizing quantum magnets and for enhancing our understanding of the experimental system. I also thank Prof. Eugene Demler and members of his group, including Takuya Kitagawa, David Pekker and Bernhard Wunsch for their insights and calculations on various dynamical processes in our experiments. Lode Pollet kindly carried out many quantum-Monte Carlo simulations for our group, and Michael Gullans did calculations on the feasibility of implementing superexchange-based transverse Ising models.

The MIT-Harvard Center for Ultracold Atoms is a wonderful place to carry out research in this field. I have been inspired by many discussions with the professors here including Profs. Wolfgang Ketterle, Mikhail Lukin and Vladan Vuletic. I thank Prof. Vuletic in particular for convincing us that polarization gradient cooling would work in a lattice. Prof. David Weiss at Penn State graciously provided the design for the microscope objective we used and our research has benefited tremendously from his pioneering work on imaging single atoms in a lattice.

Finally, I thank my friends at Harvard and MIT for making my time in Cam-

Acknowledgments

bridge a very enjoyable one. Most importantly, I thank my family for their love and encouragement over the years.

To my family

#### Chapter 1

#### Introduction

Over the past few decades, a wide range of materials with unusual, and often technologically useful, properties has been discovered. The unifying aspect of these materials is that they exhibit strong correlations between the electrons [196, 10] that cannot be adequately described using Fermi liquid theory [121]. Examples include high-temperature superconductors [117], colossal magnetoresistance materials [152], heavy-fermion metals [88] and quasi-low dimensional materials [182]. The strong correlations in these materials is a consequence of Coulomb or effective spin-spin interactions that dominate the kinetic energy. The theoretical understanding of strongly correlated materials is still in its infancy and there are many open questions, particularly in high- $T_c$  superconductors. Many so-called minimal models have been proposed to explain the behaviour of strongly correlated materials, including the Hubbard [89], t-J [39] and the Anderson models [7]. Despite the apparent simplicity of such models, exact solutions are not available in more than one dimension and numerical simulations of large systems require enormous resources.

The simulation challenge was already anticipated by R. Feynman in 1981, who pointed out that the simulation of quantum systems on classical computers is in general a hard problem [55]. To understand why this is the case, we consider as an example the most general state of a quantum system of N interacting spin- $\frac{1}{2}$  particles, which can be written as

$$|\Psi\rangle = \sum_{i_1 \in \{\uparrow,\downarrow\}} \dots \sum_{i_n \in \{\uparrow,\downarrow\}} c_{i_1,i_2,\dots,i_n} |i_1,i_2,\dots i_n\rangle, \tag{1.1}$$

requiring the specification of  $2^N$  amplitudes. This is to be compared with the state of a classical system, which requires the specification of only N parameters. This means that for a fixed system size, a computation on a classical computer takes an exponentially longer time for a quantum system than for the corresponding classical system. The simulations we refer to here can either be computations to determine equilibrium properties such as expectation values of observables or n-point correlators, or even more challenging, simulations of the dynamics. The exponential resources are only required if the quantum system is not separable into smaller systems, i.e. the constituents of the system are linked and any part of the system cannot be described without reference to the rest of the system. This is the concept of entanglement first pointed out in the famous EPR paradox [51]. Entangled states play an important role in some very interesting collective condensed matter states such as the Laughlin [115] or BCS [18] states. The other context they appear in is in the study of quantum phase transitions, the focus of this work. The state of the the system undergoing the transition exhibits an increasing degree of entanglement as the critical regime is approached [161, 186].

As a solution to the problem of simulating quantum systems, Feynman introduced the idea of a quantum simulator: a physical quantum system that is easily controlled and probed can be used to simulate another less accessible quantum system that is governed by the same physics. In recent years, ultracold atoms in optical lattices have emerged as a powerful quantum simulator of condensed matter systems [27, 119]. Ultracold atom systems can be brought into the strongly correlated regime using Feshbach resonances [93] or optical lattices [78], and can have long coherence times, necessary prerequisites for generating and preserving entanglement that makes quantum simulation useful. On the other hand, they are more accessible than condensed matter systems in several ways. First, many parameters of optical lattice systems can be dynamically varied such as interaction strengths or lattice geometry. Second, in comparison to real materials, these systems can be made very clean and impurities or disorder can be added back in a controlled way. Third, the lattice spacings are about four orders of magnitude larger than in a solid, allowing the possibility of probing and manipulating at the smallest length-scale using optical techniques as demonstrated in this work. Fourth, the dynamics are much slower than in a real solid, making real-time observations of dynamical processes possible. Finally, the individual components of these systems are understood from first principles and complexity can be built up from these components in a controlled way.

We will focus on studying quantum phase transitions of ultracold atoms in optical lattices. We investigate the transition from a superfluid to a Mott insulator in a bosonic system and the transition from a paramagnet to an antiferromagnet in a quantum spin system. We look at both equilibrium and dynamical properties of the

resulting many-body states as we cross the phase transition. While the system sizes are still relatively small, they can be in principle scaled up to the sizes where classical simulation becomes infeasible.

Until this work, ultracold atoms in optical lattices were studied using bulk measurements. For example, the superfluid to Mott insulator transition has been detected using global phase coherence, measurements of energy gaps and compressibility measurements [78, 101, 165]. In a sense, this approach is similar to traditional bulk measurement techniques used in condensed matter such as transport measurements or determinations of heat capacities and susceptibilities. However, over the last few decades, microscopy techniques that are able to resolve individual atoms in solids, such as scanning tunneling microscopy [25] or aberration-corrected electron microscopy [52], have revolutionized experimental work in condensed matter. We have developed the analogue of these microscopy techniques for ultracold atoms in an optical lattice: the ability to image and manipulate single atoms on individual lattice sites, which we refer to as "quantum gas microscopy". The realization of this microscopy technique has involved the development a new set of tools in our laboratory [14, 13], including the preparation of strongly interacting, single layer twodimensional ultracold atom systems that are combined with high resolution optics, as well as techniques to keep the atoms in place during the imaging process.

Quantum gas microscopy opens up three distinct capabilities: (i) imaging the many-body quantum state with high fidelity and single site resolution, (ii) engineering the potential landscape of the atoms at a similar length-scale and finally (iii) manipulating the state of individual atoms. We shows examples of all these applica-



Figure 1.1: Concept of the quantum gas microscope. A degenerate gas of ultracold atoms resides in a two-dimensional lattice, a few microns away from the final lens of a high resolution imaging system. The lattice spacing is small enough ( $\approx 0.5 \mu m$ ) to achieve a strongly correlated quantum gas which can be used to simulate the physics of condensed matter systems. The high resolution system allows the imaging and addressing of individual atoms in the lattice, capabilities similar to those provided by scanning tunneling microscopy of solids.

tions in this work. In-situ imaging of many-body states gives direct access to local observables and correlation functions, and allows the study of local dynamics. The ability to engineer potential landscapes almost arbitrarily should open the path towards engineering many complex Hamiltonians. Finally, the ability to manipulate the state should allow the initialization of the system in out of equilibrium states and perhaps more importantly, opens the door to optical lattice-based quantum computation. The general concept of the quantum gas microscope is shown in Figure 1.

We apply quantum gas microscopy to the study of quantum phase transitions,

revealing phenomena that were not amenable to study with bulk measurements. The first quantum phase transition we study is the superfluid to Mott transition in a bosonic system, which had been previously observed [78], but we present the first microscopic study of the transition, including direct observation of the suppression of atom number fluctuations on lattice sites across the transition as well as local dynamics. The second phase transition is a simulation of a magnetic transition in a quantum spin chain. The results presented are the first time quantum magnetism has been explored in optical lattices. We hope that the microscopic study of these two phase transitions, important in their own right, demonstrates more generally the power of quantum gas microscopy in performing condensed matter quantum simulations.

The general outline of this thesis is as follows:

- The second chapter gives a general introduction to quantum phase transitions and critical phenomena from a condensed matter perspective. It provides theoretical descriptions of the superfluid to Mott insulator transition and magnetic quantum phase transitions in spin systems, using the transverse Ising model as an example.
- The third chapter is an overview of Bose-Einstein condensates in both the weakly and strongly interacting regimes, with the latter achieved in optical lattices. The topics covered include band structure in an optical lattice and the mapping to the Bose-Hubbard model. The onsite and global density distributions are studied as parameters of the model are tuned to induce the phase transition from the superfluid to Mott insulator.
- The fourth chapter deals with the experimental techniques used throughout the

rest of this work. These include the creation of two-dimensional condensates near an optical surface, techniques to control the atom number and reduce the temperature in the condensate and measures to reduce the disorder in the light potentials. We delve into the details of quantum gas microscopy including fluorescence imaging of the atoms and the projection of arbitrary light patterns onto the atoms with high resolution optics. Other techniques that became possible in our system are also described such as site-resolved modulation spectroscopy.

- The fifth chapter presents results on the microscopic observation of the superfluid to Mott insulator transition. The results include single site measurements of atom number fluctuations across the transition, thermometry down to zero temperature, high resolution imaging of the shell structure of the insulator, measurements of local adiabaticity timescales and finally studies of density correlations in the insulator.
- The sixth chapter presents results on the microscopic observation of a magnetic quantum phase transition from a paramagnet to an antiferromagnet in a one-dimensional chain of quantum pseudospins. The results include single site studies of magnetization across the transition and verification of Neel ordering through noise correlation measurements, studies of domain formation and adiabaticity timescales, preparation of the highest energy many-body state of the system and manipulation of individual spins in the chain.
- The seventh chapter is an outlook for future work.

#### Chapter 2

# Quantum phase transitions: a condensed matter perspective

#### 2.1 Classical vs. quantum phase transitions

A classical phase transition is a transformation of a thermodynamic system between different phases that is induced by a change in the system's temperature. Examples include transitions between a solid and a liquid at the melting point, between a ferromagnet and a paramagnet at the Curie point, and between a thermal cloud and a Bose-Einstein condensate at the critical temperature of an ultracold dilute gas of atoms [142]. These transitions can only happen at finite temperature because thermal fluctuations are needed to drive the reorganization of the atoms or spins in the system into the new phase. In contrast, quantum phase transitions (QPTs) are induced by varying a physical parameter of the system other than its temperature, e.g. a magnetic field or the pressure applied to a solid [161]. Such transitions can

occur even at zero temperature where all thermal fluctuations are frozen out, because the reorganization of the system is driven by quantum fluctuations.

Quantum phase transitions can be understood in terms of the energy spectrum of a many-body quantum system. This spectrum has a ground state and a first excited state separated by some gap  $\Delta$ . This gap depends on the value of the physical parameter g used to induce the transition. As g is varied, there is an avoided level crossing between the lowest two states at a critical value  $g_c$  where the gap reaches its smallest value. In a thermodynamic system, this gap vanishes, and we have a phase transition. The properties of the many-body ground state are different on the two sides of the transition. This difference is reflected in the order parameter of the transition which is zero on one side and finite on the other. An example of an order parameter is the magnetization along a particular axis in certain magnetic transitions. Order parameters usually exhibit a spontaneously broken symmetry in the ordered phase, e.g. the magnetization breaks rotational symmetry by pointing in a particular direction in a ferromagnet.

Figure 2.1 shows the phase diagram for a generic quantum phase transition [161]. Strictly speaking, a quantum phase transition happens only at zero temperature. At T=0, there is a critical point  $g_c$  separating a quantum disordered phase from an ordered phase that is characterized by a finite order parameter. It is important to note that the quantum disordered phase is only "disordered" in the sense that the order parameter vanishes in that phase and there is no spontaneously broken symmetry, i.e. it still has zero entropy at T=0. As the temperature is increased, the ordered phase will undergo a classical phase transition to a disordered phase at a critical

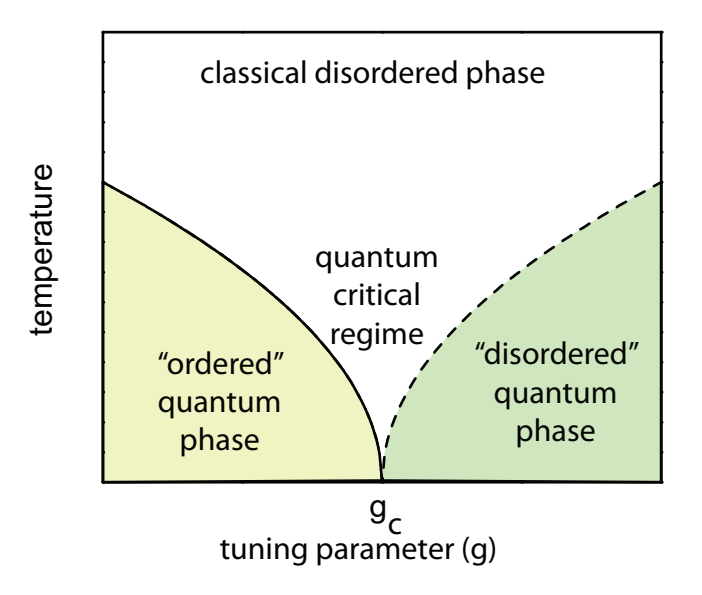


Figure 2.1: Generic phase diagram for a quantum phase transition. At zero temperature, a critical point separates the ordered and disordered quantum phases. These phases persist at finite temperature, with the solid curve indicating the phase transition boundary between the ordered quantum phase and the classical disordered phase at a critical temperature that depends on the value of the tuning parameter g. A finite temperature quantum critical region extends above the zero-temperature critical point.

temperature  $T_c$ , which goes to zero at the quantum critical point. We can still detect signatures of a quantum phase transition even for systems at finite temperature if the characteristic energy scale of the quantum fluctuations  $\hbar\omega$  dominates  $k_BT$ . At finite temperature, we can talk about a quantum critical region above the quantum critical point, and this is the region that is perhaps most interesting to study theoretically. Such a phase diagram has been recently explored in the field of ultracold atoms by looking at the finite temperature superfluid to Mott transition [184] and examples illustrating this phase diagram are given in Table 2.1.

Model	Order parameter	Broken symme-	Ordered	Quantum dis-
		try	phase	ordered phase
Transverse	z-magnetization	up/down spin	ferromagnet	quantum
Ising	$\langle S_z \rangle$	symmetry $Z_2$		paramagnet
Bose-	global phase $\langle a \rangle$	gauge symmetry	superfluid	Mott insula-
Hubbard		U(1)		tor

Table 2.1: Examples of the phase diagram in Figure 2.1. These examples are discussed in more detail in the following two sections.

Quantum phase transitions have only been studied in a handful of strongly correlated electron systems (Table 2.2), in part because of the difficulty of finding materials that are experimentally tunable into the quantum critical regime. In recent years, there have been many observations of quantum phase transitions with cold atoms including the superfluid to Mott insulator transitions with bosons [78] and fermions [101], the transition to an itinerant ferromagnet in a Fermi gas [99] and the pinning transition for a Luttinger liquid of bosons [84]. In the next two sections, we will discuss in detail two specific examples of quantum phase transitions that are relevant to our cold atom experiments: magnetic phase transitions in Ising models and the superfluid to Mott insulator phase transition.

#### 2.2 Quantum phase transitions in Ising models

In this section, we will consider systems of localized spins on a lattice that interact with each other. In a solid, the interactions can be magnetic dipole interactions between atoms with unpaired spins, spin-dependent electrostatic interactions (direct exchange), or even anion-mediated magnetic interactions between two transition metal ions (superexchange) [111, 6]. Spin systems can exhibit different orderings in

Material	Classification	Experimental	Competing orders	Reference
		tuning		
$CoNb_2O_6$	magnetic in-	magnetic	quasi-1D Ising ferromagnet,	ref. [42]
	sulator	field	quantum paramagnet	
TlCuCl <sub>3</sub>	magnetic in-	pressure	dimer antiferromagnet,	ref. [158]
	sulator		dimer spin-liquid	
$CePd_2Si_2$	heavy	pressure	antiferromagnet, paramag-	ref. [173]
	fermion		net	
	metal			
$\mathrm{Sr_3Ru_2O_7}$	metallic	magnetic	possible electronic nematic	ref. [81]
	metamagnet	field	order, drives polarization of	
			spin Fermi seas	

Table 2.2: Examples of quantum phase transitions studied in solids. These systems are strongly correlated insulators or metals that also exhibit competing magnetic orderings near the quantum critical point. The material is typically brought to the quantum critical regime by tuning a magnetic field, doping level, or the pressure applied to the solid to change ratios of exchange couplings.

their ground states. Ferromagnetic states have a non-zero magnetization because the intrinsic interactions prefer the alignment of the spins in the same direction picked by spontaneously breaking rotational symmetry. Paramagnetic states also have a finite magnetization, but in this case due to the alignment of spins with an external field. On the other hand, antiferromagnetic states have zero net magnetization, but finite and opposite magnetizations on two sublattices, e.g. in a chain, this would correspond to spins alternately pointing in opposite directions.

The behaviour of spin systems with low effective dimensionality or spin is often dominated by quantum fluctuations, making a quantum treatment of these systems necessary and yielding much richer physics than classical spin systems. In classical magnetism, the spin is an n-component vector of fixed magnitude, and models with n=1,2 and 3 are known as Ising, XY and Heisenberg models respectively. The spin interactions have the form  $\vec{S}_i \cdot \vec{S}_j$  where i and j denote nearest neighbour sites on the

lattice. On the other hand, in quantum magnetism, the classical vectors are replaced with quantum spins. For example, in the classical Ising model, each site of the lattice is associated with a variable that can have values of  $\pm 1$ . In the quantum Ising model, we have a quantum spin-1/2 on each site. Each spin can be in an "up" state, "down" state or any superposition of these two states. The quantum system with N sites has a Hilbert space with  $2^N$  dimensions. The Hamiltonian has the classical spin vectors replaced with Pauli matrices for spin-1/2 particles

$$\sigma_x = \begin{pmatrix} 0 & 1 \\ 1 & 0 \end{pmatrix}, \sigma_y = \begin{pmatrix} 0 & -i \\ i & 0 \end{pmatrix}, \sigma_z = \begin{pmatrix} 1 & 0 \\ 0 & -1 \end{pmatrix}, \tag{2.1}$$

which obey the usual commutation relations  $[\sigma_i, \sigma_j] = 2\epsilon_{ijk}i\hbar\sigma_k$ . The coupling of spin operators in the Hamiltonian determines the classification of the quantum model, e.g. Ising models have  $\sigma_z^i \sigma_z^j$  terms, while Heisenberg models have  $\sigma_x^i \sigma_x^j$ ,  $\sigma_y^i \sigma_y^j$  and  $\sigma_z^i \sigma_z^j$  terms. For the XY and Heisenberg models, the interactions are said be isotropic if they are the same in all spatial directions and anisotropic otherwise.

In order to study magnetic quantum phase transitions, we will need a Hamiltonian with non-commuting terms, a necessary requirement to drive the phase transition, and the terms should favor ground states with different symmetries. One example of a simple Hamiltonian that satisfies these properties is the quantum Ising model in a transverse field [161]. For a one-dimensional chain, this Hamiltonian is

$$H = \sum_{i} -J\sigma_z^i \sigma_z^{i+1} - h\sigma_x^i \tag{2.2}$$

where J>0 is the spin-spin coupling and h is the external field along the x direction. We define a dimensionless parameter g=h/J. For  $g\longrightarrow\infty$ , the ground state has all the spins aligned with the field pointing along the x direction:  $|\to\to\to\to...\rangle$ . For  $g\longrightarrow0$ , the ferromagnetic interactions align all the spins together either along the positive or negative z direction, with the symmetry being spontaneously broken, i.e.  $|\uparrow\uparrow\uparrow\uparrow...\rangle$  or  $|\downarrow\downarrow\downarrow\downarrow...\rangle$ .

The two extremes of g are connected by a phase transition that occurs exactly at the critical point  $g = g_c = 1$ . To understand what this means, we need to define an order parameter for the transition, which we take to be the magnetization along the z-direction given by  $m = \langle \sigma_z \rangle$ . The order parameter m is non-zero only in the ferromagnetic state where  $g < g_c$ . As indicated before, we expect an avoided level crossing between the many-body ground state and the first-excited state at the critical point, with a gap that shrinks with the chain length. This can be verified by studying the single particle excitation spectrum. For this particular Hamiltonian, the Jordan-Wigner transformation can be used to obtain the spectrum exactly [161], and the zero-momentum single particle excitations have energy

$$\Delta = 2J|1 - g|,\tag{2.3}$$

and the gap vanishes at  $g = g_c$  as expected.

In Chapter 6, we shall experimentally investigate a close cousin of the transverse Ising model, where the interactions are antiferromagnetic and the applied field can have both transverse and longitudinal components. We find a phase transition between an antiferromagnetic and paramagnetic phase, and in fact the two models are in the same universality class, meaning that their behaviour is identical near the critical point [163].

An interesting feature of this general class of quantum magnetic models, known as quantum rotor models [161], is that their physics formally maps onto that of classical models in one higher spatial dimension [161]. For example, a zero-temperature quantum Ising chain in a transverse field maps onto a finite temperature classical zero-field Ising model on a square lattice, where the temperature in the classical system corresponds to the transverse field in the quantum system. This allows us to use a lot of our intuition from classical statistical mechanics to understand such quantum phase transitions. In this case, it is well known that a 2D classical Ising model exhibits a phase transition between an ordered and disordered phase at some critical temperature. The energy gap  $\Delta$  of the quantum system is related to the correlation length  $\xi$  in classical system through  $\Delta \sim 1/\xi$ , i.e. the vanishing energy gap corresponds to a diverging length-scale.

Finally, we note that magnetic quantum phase transitions have been the subject of experimental studies in solid-state systems [161, 162], e.g. transverse Ising models have been investigated in LiHoF<sub>4</sub> [26] and in CoNb<sub>2</sub>O<sub>6</sub> [42] by tuning the transverse field, and pressure-induced quantum phase transitions of dimer spin liquids have been studied in TlCuCl<sub>3</sub> [158]. While traditional applications of magnetic materials, such as in hard-disks, have relied on classical spin systems, low temperature properties of magnetic materials in a quantum regime are being investigated in many labs, including industrial ones, because of potential applications in future devices [17].

## 2.3 The superfluid to Mott phase transition in the Bose-Hubbard model

So far, we have focused our attention on magnetic models of spins localized on a lattice. Another interesting class of phase transitions involves a redistribution of the charge, or in a neutral system, the density, degree of freedom. Such phase transitions appear in describing transitions between conducting and insulating states in solids. The Hubbard model, a simple model of particles (bosons or fermions) interacting on a lattice, exhibits a phase transition of this class. In this model, the particles can either tunnel between neighbouring lattice sites or interact when they are on the same site.

The Fermi-Hubbard model has been the subject of intense research because it might be a minimal model for understanding high-temperature superconductivity in the cuprates [9]. Nevertheless, we will immediately specialize to the better understood Bose-Hubbard model [56], where the particles are spinless bosons on a lattice. These bosons could be Cooper pairs in a quantum-regime Josephson-junction array [64], helium atoms adsorbed on a porous substrate such as Vycor [45] or rubidium atoms in an optical lattice [78].

Introducing operators to create (destroy) a boson on the *i*th lattice site,  $\hat{a}_i^{\dagger}(\hat{a}_i)$ , we write down the Hamiltonian describing the dynamics of the system

$$H = -J\sum_{\langle ij\rangle} \left( \hat{a}_i^{\dagger} \hat{a}_j + \hat{a}_j^{\dagger} \hat{a}_i \right) + U/2\sum_i \hat{n}_i (\hat{n}_i - 1) - \mu \sum_i \hat{n}_i$$
 (2.4)

where  $\hat{n}_i = \hat{a}_i^{\dagger} \hat{a}_i$  is the number of bosons on the *i*th lattice site, J is the tunneling matrix element between neighbouring lattice sites, U is the onsite interaction energy

and  $\mu$  is the chemical potential, which can be used as a constraint to fix the total atom number  $N = \sum_i \hat{n}_i$ . This Hamiltonian is a valid description in the tight-binding regime, where nearest neighbour tunneling is much faster than next-nearest neighbour tunneling and when the interactions are short-range, so that they are non-negligible only for particles on the same site. For example, for atoms in an optical lattice, the interaction is a contact interaction arising from the underlying van der Waals potential [142].

The quantum phase transition in this model is induced by tuning the interaction to tunneling ratio U/J. For large J, the ground state particles are delocalized over the entire lattice in a superfluid state given by

$$|\Psi\rangle = \left(\sum_{i} a_{i}^{\dagger}\right)^{N} |0\rangle \tag{2.5}$$

where  $|0\rangle$  is the vacuum. On any particular lattice site, the particle number is not fixed and exhibits Poissonian number fluctuations (Fig. 2.2(b)). The phase  $\hat{\phi}_i$  and particle number  $\hat{n}_i$  on a site are conjugate variables obeying  $\left[\hat{\phi}_i, \hat{n}_i\right] = i$ . This leads to a well defined phase on each lattice site, and the tunneling locks these phases together across the lattice. On the other extreme of large U, number fluctuations are suppressed. For a given chemical potential  $\mu$ , the particle number per site is fixed and constant across the lattice, forming a state known as a Mott insulator (Fig. 2.2(a))

$$|\Psi\rangle = \prod_{i} \left(a_i^{\dagger}\right)^n |0\rangle \tag{2.6}$$

where n is the particle number per site. The insulating property arises as a result of

a many-body energy gap on order U that suppresses charge transport.

A first attempt at understanding the phase diagram of the system can be obtained using a mean field approach [161], by introducing a complex field  $\Psi_{MF}$  representing the "mean field" that replaces operators on nearest neighbours. The mean field Hamiltonian is

$$H_{MF} = \sum_{i} \left( -J\Psi_{MF} \hat{a}_{i}^{\dagger} - J\Psi_{MF}^{*} \hat{a}_{i} + U/2 \sum_{i} \hat{n}_{i} (\hat{n}_{i} - 1) - \mu \sum_{i} \hat{n}_{i} \right)$$
(2.7)

The ground state is found by minimizing the energy over  $\Psi_{MF}$ . It turns out, as with the magnetic phase transitions considered in the previous section, that this transition can be described in the Landau framework of second order phase transitions, with  $\Psi_{MF} = \langle \hat{a} \rangle$  as the order parameter. In the Mott insulator, the order parameter is zero as there is no well defined phase, while in the superfluid, there is a broken U (1) symmetry and  $\Psi_{MF} \neq 0$ . The mean field phase diagram in  $zJ/U - \mu$  space is shown in Figure 2.2(c), where z is the coordination number of the lattice. It exhibits a series of Mott insulating lobes with an increasing number of particles per site for increasing chemical potential given by  $n = \lceil \mu/U \rceil$ . The lobes shrink for higher particle number per site, a consequence of Bose enhancement that enhances quantum fluctuations that destroy the Mott state. It is important to note that, in a homogeneous system (constant chemical potential), the Mott state cannot be reached from the superfluid state by reducing J/U unless the ratio of particle number to number of lattice sites is an integer.

Besides the lack of broken symmetry, the Mott phase is distinguished from the superfluid phase by two other properties. The first is the existence of a many-body

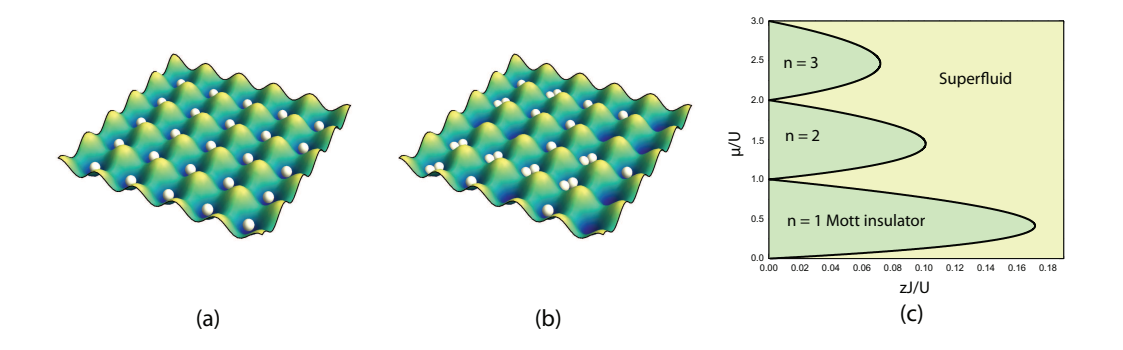


Figure 2.2: Mott insulating and superfluid phases in a lattice. (a) When the interactions dominate the tunneling, the system is in a Mott insulating state with atoms localized on lattice sites and a fixed atom number per site. (b) On the other extreme of dominant tunneling, each atom is delocalized over the entire lattice and the onsite atom number exhibits Poissonian number fluctuations. (c) Mean field phase diagram of the Bose-Hubbard model as a function of the tunneling to interaction ratio (zJ/U) and the chemical potential  $(\mu/U)$ , both in units of the interaction. The phase diagram has a series of Mott insulating lobes at low zJ/U, indicating that the atom number per site is fixed but depends on the local chemical potential.

energy gap, that becomes U in the limit of vanishing tunneling. The superfluid phase on the other hand can be excited at any energy due to the existence of continuum of spin wave modes where the phase slowly varies from ones site to the next. A related characteristic of the Mott insulator is that it is incompressible. The compressiblity,  $\kappa$  is defined by the response of the density to a change in the chemical potential

$$\kappa = \frac{\partial \hat{\rho}}{\partial \mu} \tag{2.8}$$

and is zero only in the Mott phase.

It is interesting to note that, unlike the magnetic models considered in Sec. 2.2, the superfluid to Mott transition, in general, cannot be mapped onto a classical model in one higher dimension. However, there is a particular case in which this works,

namely a transition at fixed density that occurs when crossing the phase diagram orthogonally to a Mott lobe tip. In that case, the transition is the universality class of the d+1 XY model [56].

#### 2.4 Critical phenomena

The behaviour of many-body systems near quantum critical points is a subject of intense research [162, 160]. Near a critical point, the correlation length of the system diverges and its dynamics slow down. Response functions of the system, such as the susceptibility of a magnetic system, also diverge, making for example magnetic systems very sensitive to small fields.

Near a critical point, diverging or vanishing observables are characterized by parameters known as critical exponents, which describe a power low scaling with the tuning parameter. For example the correlation length  $\xi$  diverges as  $\xi \sim |g - g_c|^{-\nu}$  where  $\nu$  is a critical exponent, while the gap  $\Delta$  vanishes as  $\Delta \sim |g - g_c|^{z\nu}$  where  $z\nu$  is another critical exponent. Renormalization group theory predicts that many different physical systems have the same behaviour near their critical points, meaning that they have the same critical exponents [192]. Such systems are said to be in the same universality class.

In order to study critical phenomena, the system should be homogeneous and sufficiently large; inhomogeneous systems will have different critical points for different parts of the system, effectively smearing out the transition, while small systems will not exhibit sharp features in the transition. The local probing capability in our experiments allows us to avoid averaging over inhomogeneities which are typically present

in cold atom systems because of trapping potentials. Ref. [197] discusses various ways to probe critical physics in the superfluid-to-Mott transition including the scaling of density profiles, quantum critical transport and investigations of the Kibble-Zurek mechanism in these systems. In the magnetic system considered in Chapter 6, we have demonstrated that we can achieve a simultaneous phase transition across the whole magnet by making the applied fields as homogeneous as possible, but larger systems will be necessary for explorations of critical phenomena in that system.

#### Chapter 3

## Ultracold bosons in optical lattice potentials

The experiments we will describe use ultracold bosons in optical lattices to simulate quantum phase transitions studied in condensed matter physics. At first glance, dilute atomic gases are a curious system to try to simulate phenomena that happen in solids. For example, the neutral atoms do not interact via Coulomb interactions and the interatomic spacings are about four orders of magnitude larger than in a solid. Nevertheless, dilute atomic gases can be cooled to the quantum degenerate regime that characterizes electrons in a solid at room temperature. Band structure can be introduced through periodic potentials created with optical lattices, and a variety of interactions can be engineered, ranging from simple contact interactions to long-range dipolar interactions with cold molecules [134]. The issue of large interatomic spacings does not matter as long as interactions can be made to dominate the behaviour of the system so that it is in a strongly correlated regime; in fact the large spacings open

up the possibility to optically probe and manipulate the atoms and slows down the dynamics, making them more amenable to study.

Our experiments use rubidium-87, a bosonic species. While ultracold fermions give rise to the Fermi sea structure of electrons in a solid, they are experimentally more difficult to cool than bosons. Ultracold bosons are interesting in their own right: Cooper pairs in superconductors and superfluids are effectively bosonic, and their behaviour is captured quite well by interacting Bose-Einstein condensates. For simulating magnetism with localized spins, the nature of the particles is not as important, although the traditional superexchange mechanism for producing interactions [49] naturally produces interactions of different signs for fermions and bosons.

Our experiments will simulate electron systems in which interactions play a dominant role. Often, the kinetic energy of the atoms in an ultracold system, both due to the finite temperature of the atoms and their quantum delocalization, competes with interactions. One approach to bringing a cold atom system to a strongly interacting regime is to increase the interaction strength. For example, the contact interaction that is naturally present can be enhanced through a Feshbach resonance in certain atomic species [93]. In bosons, the resonance also enhances three-body losses which complicates this route. Alternatively, it might be possible to utilize another kind of stronger interaction such as the electric dipole interaction between Rydberg atoms [187]. A second approach is to reduce the kinetic energy, by cooling the system to very low temperatures where thermal fluctuations are negligible and by increasing the effective mass of the atoms. The latter is easily accomplished by putting the atoms in an optical lattice. In the following sections, we review the theory

of Bose-Einstein condensates in both the weakly interacting regime and in a strongly interacting regime achieved through the optical lattice route.

## 3.1 Bose-Einstein condensates in the weakly interacting regime

Bose-Einstein condensation in a dilute gas of alkali atoms was first experimentally achieved in 1995 [5, 47]. In a condensate, a macroscopic number of atoms occupies the motional ground state. Interactions are typically weak, as characterized by the quantum depletion fraction [28]  $\sim \sqrt{na_s^3} \ll 1$  which measures the reduction of ground state occupation due to the interactions. Here n is the mean density of the sample and  $a_s$  is the s-wave scattering length quantifying the interaction strength. Therefore, the wavefunction of the condensate can be approximated as a product of identical single particle wavefunctions, or in other words, the whole condensate can be regarded as a "superparticle" which is described by a Schroedinger equation. When the interactions are included in a mean field picture, this Schroedinger equation is known as the Gross-Pitaevskii equation [142]

$$\left(-\frac{\hbar^2}{2m}\nabla^2 + V_{ext}(r) + g|\psi(\vec{r},t)|^2\right)\psi(\vec{r},t) = i\hbar\frac{\partial\psi(\vec{r},t)}{\partial t},$$
(3.1)

where  $V_{ext}(r)$  is the external trapping potential and the interaction paramter g is given by

$$g = \frac{4\pi\hbar^2 a_s}{m}. (3.2)$$

. Equation 3.1 correctly predicts the density profile of condensates in parabolic traps (see Sec. 4.2.3 for the case of a 2D condensate), as well as many dynamical properties of condensates. The ratio of the interaction to kinetic energy in this system is given by

$$\frac{\epsilon_{int}}{\epsilon_{kin}} \sim \frac{gn}{\hbar^2/m \ n^{2/D}} \approx 4\pi \ n^{\frac{D-2}{D}} a_s \tag{3.3}$$

where D is the dimensionality of the system. This quantity is typically small, and increases only weakly with density for 3D systems. Interestingly in 1D systems, the system gets more strongly interacting for lower densities, leading to the formation of strongly interacting states such as the Tonks gas [104, 139].

## 3.2 Bose-Einstein condensates in the strongly interacting regime

The technique we use to bring ultracold atoms into the strongly interacting regime is to put them in an optical lattice, which reduces their kinetic energy relative to their interaction energy. Optical lattices are periodic light intensity patterns that result from the interference of light beams with a fixed phase relationship. The light patterns can be used to trap atoms through the AC Stark effect at the nodes or antinodes of the intensity pattern. Bose condensed atoms are already in a many-body ground state and by adiabatically turning on the optical lattice potential, the atoms can be loaded into the many-body ground state of the periodic potential. In the following sections, we discuss how these potentials are created and the behaviour of a single atom as well as weakly and strongly interacting atoms in such potentials.

#### 3.2.1 Optical dipole potentials

Optical potentials are created by illuminating atoms with light having a spatially varying intensity. If the light is far-detuned from the atomic resonance, the light-matter interaction is mostly conservative [82, 130]. The electric field of the light creates a rapidly oscillating dipole moment  $\mathbf{d}$  for the atom. For an atom with complex polarizability  $\alpha(\omega)$  in an oscillating field  $\mathbf{E}$ , the dipole is given by  $\mathbf{d} = \alpha \mathbf{E}$ . This induced dipole interacts with the field, which lowers its energy V:

$$V = -\langle \mathbf{d} \cdot \mathbf{E} \rangle = -\frac{1}{2} \operatorname{Re}(\alpha(\omega)) |\mathbf{E}|^2 = -\frac{1}{2\epsilon_0 c} \operatorname{Re}(\alpha(\omega)) I$$
 (3.4)

where the brackets denote a time-average and I is the light intensity. The atomic polarizability can be approximated by the simple Lorentz model of a classical oscillator with natural frequency  $\omega_0$  being driven at frequency  $\omega$ 

$$\alpha(\omega) = 6\pi\epsilon_0 c^3 \frac{\Gamma/\omega_0^2}{\omega_0^2 - \omega^2 - i(\omega^3/\omega_0^2)\Gamma}.$$
 (3.5)

The on-resonance damping rate  $\Gamma$  can be related to the matrix-element  $\mu = -e\mathbf{r}$  that connects the ground  $(|g\rangle)$  and excited  $(|e\rangle)$  states

$$\Gamma = \frac{\omega_0^3}{3\pi\epsilon_0\hbar c^3} |\langle e|\mu|g\rangle|^2. \tag{3.6}$$

For light with large detuning from the atomic resonance  $\Delta = \omega - \omega_0$ , a rotating wave approximation yields a simplified expression for the dipole potential

$$V \approx \frac{3\pi c^2}{2\omega_0^3} \frac{\Gamma}{\Delta} I. \tag{3.7}$$

Using a spatially varying light intensity, almost arbitrary potential landscapes can be engineered. For example, a focused Gaussian beam confines the atoms at its waist for light red-detuned with respect to the atomic resonance and repels them from that region for blue detuning. A one-dimensional optical lattice can be created by interfering a light beam with its retroreflection, creating a sinusoidally varying light intensity pattern with period  $\lambda/2$  where  $\lambda$  is the wavelength of the light (Fig. 3.1(a)). This standing wave pattern can be created in all three directions to obtain an egg-carton potential for the atoms (Fig. 3.1(c)), although care has to be taken that the beams along the different axes do not interfere, for example by having a sufficient detuning between them to time-average the interference. In Sec. 4.5.2, we describe a different way of creating optical lattices by projecting an intensity pattern onto the atoms using an imaging system.

Although the light-atom interaction is mostly conservative, there is residual light scattering in a lattice. The scattering rate  $\Gamma_{sc}$  is related to the potential V through

$$\Gamma_{sc} = \frac{\Gamma}{\Delta} \frac{V}{\hbar}.\tag{3.8}$$

This scattering leads to heating of the many-body state in the lattice [68, 144]. The heating can be either due to ground-band heating or interband transitions (Fig. 3.2).

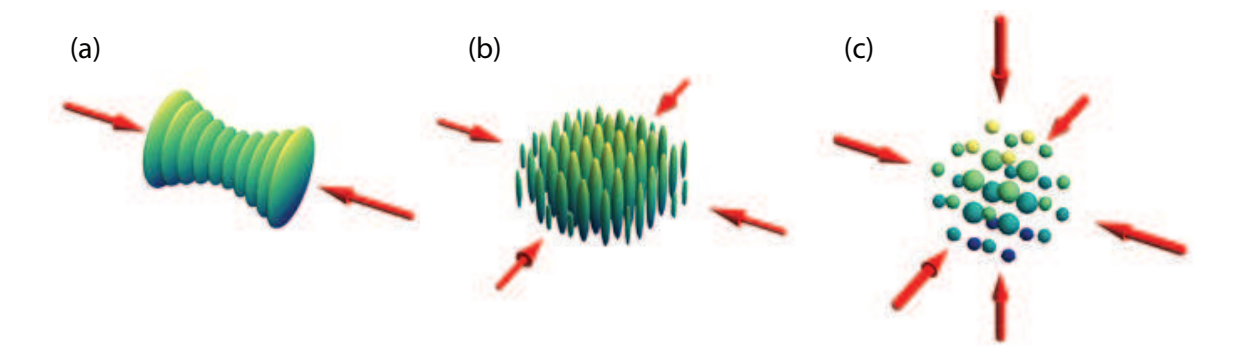


Figure 3.1: Atom density distributions for different lattice geometries. (a) Two counterpropagating beams produce a one-dimensional lattice where the atoms reside as "pancakes" at the nodes (anti-nodes) for a blue-detuned (red-detuned) lattice. (b) Two-dimensional lattice created with two sets of orthogonal beams. The beams in each set are prevented from interfering with the other set, e.g. by picking orthogonal polarizations. The atoms reside in one dimensional tubes. (c) Three-dimensional lattice created with three sets of orthogonal beams.

The first mechanism for heating involves an optical transition to an excited state followed by a decay back the ground band but with a change in the quasi-momentum. The resulting spread in quasi-momentum leads to decoherence of the wavefunction. In the second mechanism, the atom decays to a higher band. Which transitions are preferred depends on the Lamb-Dicke parameter describing the transition and whether the atoms sit at the nodes or antinodes of the intensity pattern. In a deep lattice, it can be shown that the interband heating rates for equal red and blue detunings are identical [68]. The reason for this surprising observation is that while the scattering rate in a blue lattice is smaller because the atoms sit at the nodes rather than the antinodes, each decay leads to an increase in the vibrational level, whereas in a red lattice interband transitions are suppressed by the Lamb-Dicke effect.

In our work, we use blue detuned lattices for two reasons. First, for a *shallow* lattice, the blue detuning leads to lower heating rates compared to an equal red

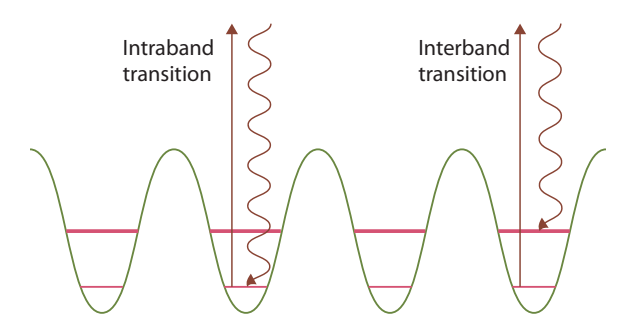


Figure 3.2: Heating in a lattice by spontaneous emission. The atoms are excited to a higher electronic state by absorbing a photon from the lattice beams. The heating occurs due to a spontaneous emission event where the atoms fall back to the lower electronic state. In an interband transition, the atoms decay to a higher band, while in an intraband transition, the atoms decay back to the same band, but with a larger spread in quasimomentum.

detuning. Second, blue lattices should have less disorder than red lattices. Disorder arises because of the interference of stray scattered light with the lattice light. This interference effect happens at the antinodes of the light intensity pattern. In a red lattice, the atoms sit at the antinodes, so the interference leads to offsets proportional to the lattice depth modulation  $\delta V$ . On the other hand, in a blue lattice, the atoms sit at the nodes, so the primary source of disorder is due to a change in the zero point energy of the atoms, an effect on order of  $(\hbar \omega_l/V)\delta V$ . Here  $\omega_l$  is onsite trap frequency, and  $\hbar \omega_l/V$  is usually a fraction of unity in a deep lattice.

#### 3.2.2 Theory of non-interacting atoms in an optical lattice

We consider the physics of a single atom moving an optical lattice. The Hamiltonian for the atom in a one-dimensional retroreflected lattice is

$$H = \frac{\hat{p}^2}{2m} + V_0 \cos^2(kx) \tag{3.9}$$

where  $\hat{p}$  is the linear momentum,  $V_0$  is the lattice depth and k is the wavevector of the lattice potential. It is well known that the eigenstates of the Hamiltonian in such a periodic potential are Bloch wavefunctions [11] that can be written as

$$\psi_a^{(n)}(x) = e^{iqx/\hbar} \cdot u_a^{(n)}(x) \tag{3.10}$$

where u is a function with the same periodicity as the potential. The wavefunctions are labelled with two indices, the band index n and the quasimomentum q. The quasimomentum plays a role very similar to a linear momentum in a non-periodic potential, except that it only makes sense to define it within what is known as a "Brillouin zone". The conventionally taken first Brillouin zone covers the range between  $q = -\hbar k$  and  $q = \hbar k$ . Intuitively, this restriction can be understood to be a result of Bragg reflection: a particle that travels at a momentum corresponding to the edge of the zone will be perfectly reflected.

The energy spectrum, known as the band structure, can be obtained by decomposing both the potential and the periodic part of the wavefunction into Fourier sums

$$V(x) = \sum V_r e^{i2rkx} \tag{3.11}$$

$$V(x) = \sum_{n} V_r e^{i2rkx}$$

$$u_q^{(n)}(x) = \sum_{s} c_s^{(n,q)} e^{i2skx}$$
(3.11)

Using these forms in 3.9, the band structure can be numerically obtained, and is shown for different depths in Figure 3.3. The bands get flatter with increasing lattice depth, corresponding to an increase in the effective mass of the particle, given by the inverse curvature of the band. In fact, in the tight-binding limit, we can define a

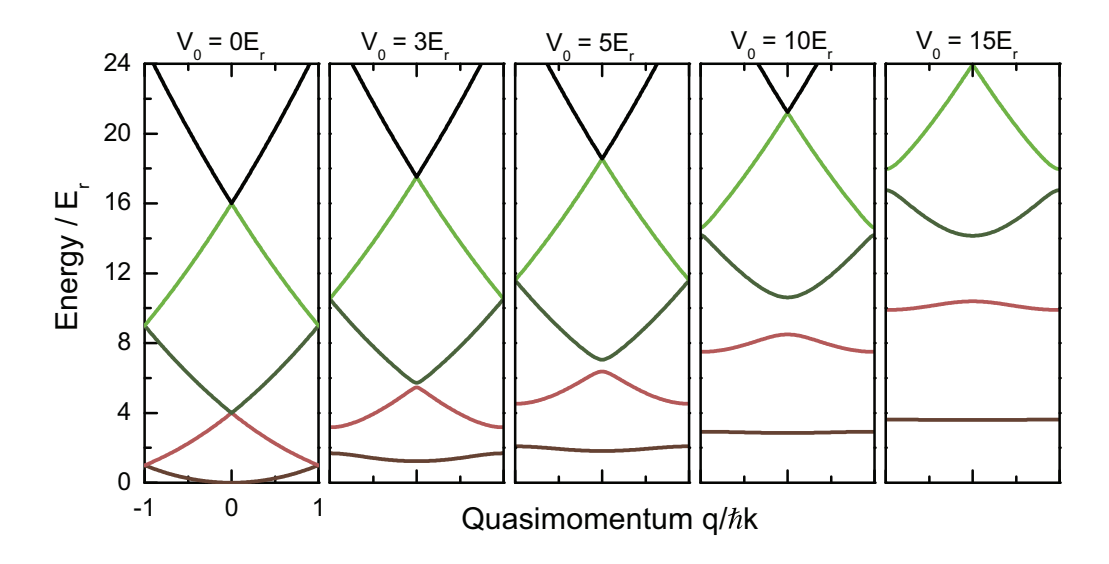


Figure 3.3: Band structure in an optical lattice. Shown are the first five bands in the lattice for increasing lattice depth. As the depth increases, gaps open up between the bands.

tunneling matrix element between neighbouring lattice sites, and this turns out to be simply a quarter of the ground-band energy width [96].

The Bloch wavefunctions describe delocalized atoms in a lattice and are a valid description in the absence of interactions. As we will see in the next section, strong enough interactions will drive a localization of the atoms on lattice sites, and at that point, it makes more sense to use a localized set of basis wavefunctions, known as Wannier wavefunctions, that are created as a superposition of Bloch functions at all quasimomenta. For an atom on site i in the nth band, the Wannier wavefunction is given by [106]

$$w_n(x - x_i) = \mathcal{N}^{-1/2} \sum_q e^{iqx_i/\hbar} \phi_q^{(n)}(x)$$
 (3.13)

where  $\mathcal{N}$  is a normalization factor. In a deep lattice, these wavefunction look very similar to the harmonic oscillator wavefunctions, except with fatter tails that increase

the tunneling matrix elements to neighbouring sites.

#### 3.2.3 Mapping onto the Bose-Hubbard model

A many-body state of atoms in a shallow lattice is in a superfluid state where each atom is delocalized over the entire lattice. The many-body wavefunction can be thought of as an array of coupled mini-condensates on the lattice sites, and tunneling locks the phases of the condensates to each other. With increasing lattice depth, the tunneling drops exponentially, and the interactions play an increasingly important role in the description of the system. The atoms localize forming a Mott insulator as described in Sec. 2.3. The Bose-Hubbard Hamiltonian that was used in that section to capture the essence of this phase transition

$$H = -J\sum_{\langle ij\rangle} \left( \hat{a}_i^{\dagger} \hat{a}_j + \hat{a}_j^{\dagger} \hat{a}_i \right) + U/2\sum_i \hat{n}_i (\hat{n}_i - 1) - \mu \sum_i \hat{n}_i$$
 (3.14)

has two microscopic parameters, J and U, that can be calculated from first principles using the ground state wavefunctions deduced from the band structure calculation described in the previous section. The tunneling J along any axis is given by

$$J = -\int dx w(x - x_i) \left( -\frac{\hbar^2}{2m} \frac{\partial^2}{\partial x^2} + V_{lat}(x) \right) w(x - x_j)$$
 (3.15)

for any neighbouring sites i and j. The tunneling dependence on the depth can be expressed in a universal way for any separable lattice potential if these quantities are expressed in lattice recoil energies, and such a plot is shown in Figure 3.2.3(a). The

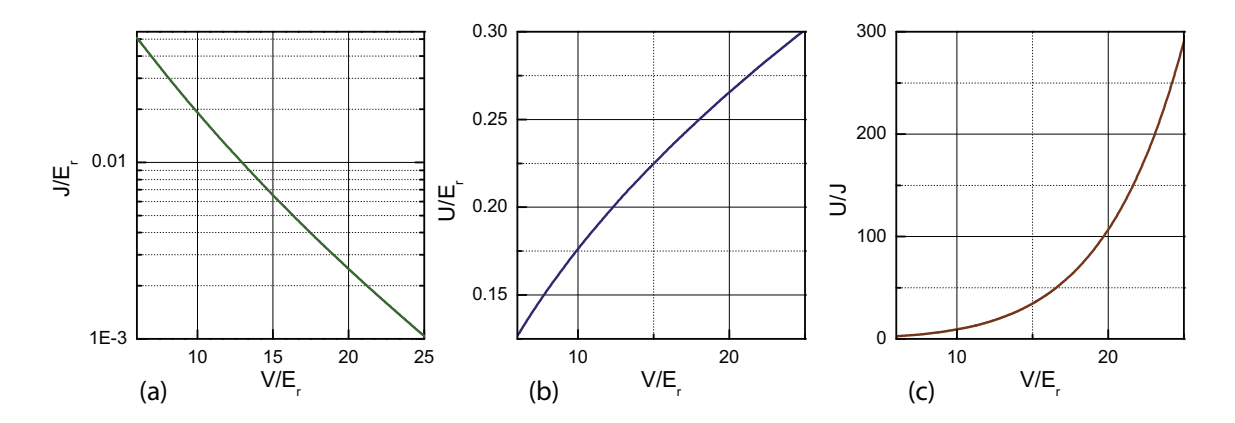


Figure 3.4: Dependence of the microscopic Bose-Hubbard parameters on the lattice depth. (a) The tunneling between neighbouring lattice sites falls exponentially with increasing lattice depth, while (b) the interaction increases weakly. (c) The ratio of the interaction to the tunneling can be easily varied over several orders of magnitude.

interaction can be written as

$$U = \frac{4\pi\hbar^2 a_s}{m} \int |\psi(\mathbf{r})|^4 d\mathbf{r}.$$
 (3.16)

In the two dimensional lattices we use, the onsite wavefunction factorizes into

$$\psi(\mathbf{r}) = w_x(x)w_y(y)\psi_{HO}(z) \tag{3.17}$$

where  $\psi_{HO}$  is the ground state of a harmonic oscillator. In a square lattice, this reduces to

$$U = \frac{4\pi\hbar^2 a_s}{m} \sqrt{\frac{m\omega_z}{2\pi\hbar}} \left( \int |w_x(x)|^4 dx \right)^2, \tag{3.18}$$

and is shown vs. the lattice depth in Figure 3.2.3(b), along with its ratio to J (Fig. 3.2.3(c)).

### 3.2.4 Shell structure in the presence of harmonic confinement

The Hamiltonian in Eq. 3.14 describes atoms in a spatially homogeneous periodic lattice potential. Experimentally, lattices are usually created with beams with a Gaussian profile. Near the center of the beam, where the atoms reside, the potential is well-approximated by a harmonic trapping potential on top of the lattice. If the site to site variation of this potential is slow compared to the lattice spacing, the local density approximation (LDA) can be invoked [20, 154, 155, 108]. In this approximation, the system is treated as being locally homogeneous, so we can define an effective local chemical potential on the *i*th site  $\mu_i = \mu - \epsilon_i$ , where  $\mu$  is the global chemical potential and  $\epsilon_i$  is the local energy offset due the harmonic confinement given by  $\epsilon_i = \frac{1}{2}m\omega^2 a^2 i^2$ , with a the lattice spacing.

In the LDA, the harmonically trapped lattice gas samples a line of constant zJ/U in the phase  $zJ/U - \mu$  phase diagram, that extends from the global  $\mu$  at the center of the trap to zero at the edge of the trap. In the Mott regime, this leads to the celebrated shell structure that has been experimentally verified [61, 35, 66].

In Sec. 5.2.4 we present high-contrast, high-resolution images of this shell structure as the atom number is varied. The number of shells observed depends on the interaction energy between the atoms, the transverse trapping frequency and the atom number. In the zero tunnelling limit, there are n shells and the (n + 1)th shell just starts to appear when

$$N = \frac{\pi U}{m\omega^2 a^2} \tag{3.19}$$

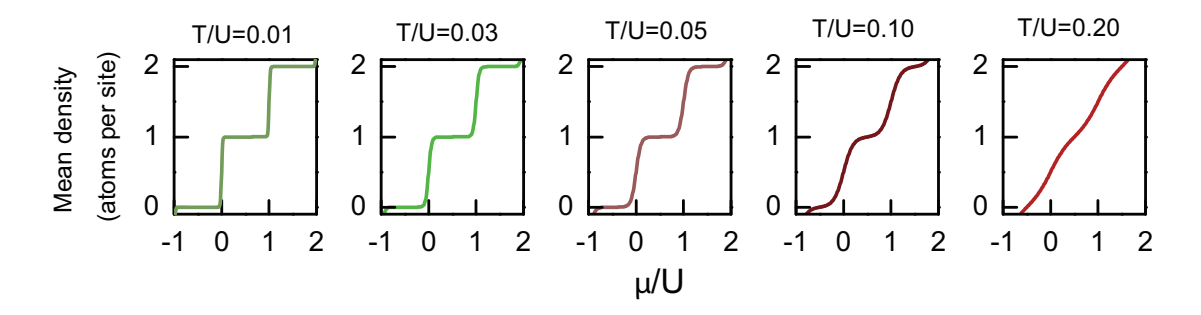


Figure 3.5: Shell structure at finite temperature in the zero-tunneling limit. The boundaries between the shells are sharp at low temperature, and become progressively smoother at higher temperatures. Eventually, the shell structure is completely washed out at  $T/U \approx 0.2$ .

where  $\omega$  is the transverse trapping frequency. Finite tunneling and temperature smoothes the shell boundaries. Most of the entropy in a Mott insulator is actually stored in the layers between the Mott shells because excitations are easiest to create there. The entropy distribution within the shell structure is discussed in Refs. [67, 148]. Figure 3.5 shows the shell structure for increasing temperature T/U in the zero-tunnelling limit. At  $T/U \approx 0.2$ , this structure is almost completely smeared out, setting an upper bound on temperatures required to observe it.

#### Chapter 4

# Experimental apparatus and techniques

Publications based on the work described in this chapter:

"A quantum gas microscope for detecting single atoms in a Hubbard-regime optical lattice", W. Bakr, J. Gillen, A. Peng, S. Foelling and M. Greiner, Nature **462**, 74-77 (2009)

"Two-dimensional quantum gas in a hybrid surface trap", J. Gillen, W. Bakr, A. Peng, P. Unterwaditzer, S. Foelling and M. Greiner, Phys. Rev. A 80, 021602(R) (2009)

The quantum phase transitions described in this work are studied using a Bose-condensed gas loaded into a two-dimensional optical lattice that resides at the focus of a high numerical aperture system able to resolve individual sites of the lattice. In this chapter, we briefly discuss the different parts of this "quantum gas microscope" and the techniques we use to prepare samples studied with the microscope as well as to probe and engineer those samples. Further details on the experimental apparatus can be found in these theses [72, 141].

A typical experimental cycle consists of preparing a 3D condensate in a magnetic trap, extracting atoms from the condensate to prepare a monolayer at the focus of the objective, adiabatically bringing the cloud into a strongly correlated regime using an optical lattice, performing the desired experiment and finally imaging the density/spin profile at the atomic level. The imaging process is destructive and provides a snapshot of the system, i.e. it projects the wavefunction onto a particular realization. Repetitions of this cycle are then used to extract statistical properties of the wavefunction such as the distribution functions of observables or various correlators.

#### 4.1 Preparing the Bose-Einstein condensate

Our experiments start with a 3D BEC of  $\approx 5 \times 10^4$  <sup>87</sup>Rb atoms prepared in the  $|F=1,m_f=-1\rangle$  state. The BEC is created by loading a magneto-optical trap for 8 seconds, resulting in  $10^9$  atoms at a temperature of  $40\mu$ k after optical molasses cooling. We then magnetically transport the atoms into a glass cell with very good vacuum (sim40s atom lifetime) [77] where we perform forced RF evaporation in a tightly confining QUIC trap [53]. The Thomas-Fermi radii of the trapped condensate are  $(3.1,3.1,27)\mu$ m.

### 4.2 Creation of two dimensional condensates using surface traps

To obtain a strongly interacting system in an optical lattice, it is desirable to have the smallest lattice spacing possible. This ensures that the interaction energy is large compared to other energy scales such as the temperature of the cloud and that the experiments can be performed quickly compared to the time-scale for decoherence processes. The smallest possible lattice spacing is half the wavelength of the light used to create the lattice. Resolving individual sites in a lattice with such a spacing requires an imaging system whose depth of focus is also on the order of a wavelength of light. Therefore, it is not possible to have multiple atom planes loaded in a 3D lattice appear in focus simultaneously. Light collected from out-of-focus atom planes "washes out" the image of the in-focus plane. There are two solutions to this problem. The first is to illuminate only one plane of the 3D sample at a time. The second is use an atomic monolayer as the sample, which is the solution we adopted.

Monolayers are gases in the 2D regime characterized by a strong confinement  $\hbar\omega_z$  in one direction that sets an energy scale much larger than that given by either the temperature  $k_BT$  or interactions U ( $\hbar\omega_z\gg k_BT,U$ ), and a weak confinement along the other two axes [75, 159, 181, 174, 107]. Such systems are of intrinsic interest, for example in studying the Berezinskii-Kosterlitz-Thouless (BKT) transition [110] recently observed in ultracold atoms [83, 168, 40]. By adding lattice potentials in the plane [107, 179], these systems are also anticipated to be useful for investigations of 2D antiferromagnets and d-wave superfluid states [117].

Different approaches for the preparation of 2D gases have been realized [27], including evanescent wave traps and RF slicing. Repulsive evanescent wave (EW) potentials were originally introduced to reflect atoms from surfaces [16, 113]. They were combined with gravity to form a gravito-optical surface trap [138, 85] in which a 2D BEC was observed [159]. The strongest axial confinement in 2D systems has

been achieved in optical dipole standing wave (SW) traps where a stack of 2D planes is populated by a BEC [181, 107, 179]. It is possible to empty all but a few planes by a radio-frequency "knife" [181, 170], but precisely controlling the population remains a challenge, in particular for traps with small periodicity.

We have investigated two different approaches to preparing 2D clouds. The first utilized a hybrid trapping potential based on an evanescent wave and magnetic fields (Fig. 4.1(a)). The second is based on a two-stage loading into standing waves with progressively smaller spacings.

#### 4.2.1 Evanescent wave surface trap

The hybrid surface trap [73] is loaded in a two-step sequence shown in Figure 4.1(b-d). First, the cigar trap in which the condensate is created is converted to a spherical trap with trap frequencies of  $2\pi(17, 20, 20)$ Hz. This trap is moved against a flat, superpolished glass surface that resides inside the vacuum chamber and is part of the final lens of the imaging system. Close to the glass, the cloud experiences a repulsive dipole potential due to an evanescent wave (EW) from a 767nm blue detuned beam with a spectral width of 2nm which is incident at an angle  $\theta_{EW}$ , 12mrad from the critical angle  $\theta_c$  and is totally internally reflected inside the glass [82, 21]. The EW that appears on the vacuum side creates an exponentially decaying potential  $V_{EW}(z) = V_0 \exp(-2z/\Lambda)$ , where z is the distance to the surface,  $\Lambda$  the decay length of the EW and  $V_0$  the potential height at the surface given by the total incoming intensity. The decay length  $\Lambda$  is given by  $\lambda_{trap}/2\pi/(n^2 \sin^2(\theta_{EW}) - 1)^{1/2} \approx 800$ nm where n is the index of refraction of fused silica. The EW potential has a maximum

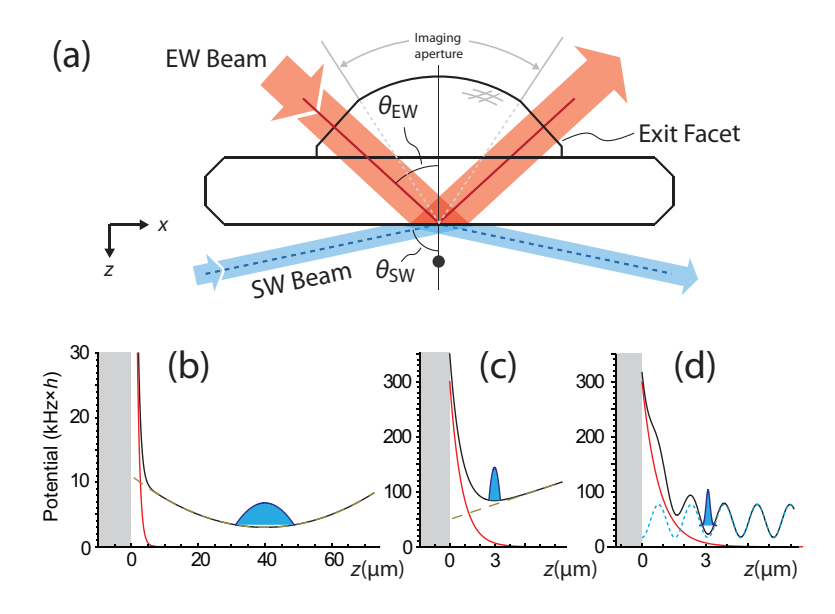


Figure 4.1: Evanescent wave trap. (a) The trap is based on a dielectric surface formed by the superpolished bottom face of a fused silica substrate. Fused to the top of the substrate is a hemispherical lens designed to be part of a high NA imaging system. Three potentials form the trap: an EW beam from the top (red dash-dotted lines), a beam reflected off the bottom side of the surface creates a standing wave (SW, blue dotted lines) and a parabolic magnetic trap (green dashed lines). (b) Schematic of magnetic trap potential with BEC closely below surface. The black line denotes the combined potential. (c) EW configuration loaded by shifting the magnetic trap minimum inside the glass generating confinement between the magnetic gradient and the EW. (d) Atoms loaded into single plane of SW trap, 1.5  $\mu$ m from the surface.

at a distance of 200nm from the surface, below which the attractive van der Waals potential dominates. The short decay length of the EW gives rise to large curvatures that allow tight confinement along the direction of the decay. Trap frequencies of up to  $2\pi \times 1 \text{kHz}$ , measured by parametric excitation, can be reached in this configuration. The weak axial confinement of 20Hz is provided by the magnetic trap.

To further increase the vertical confinement, we use an additional standing wave (SW) potential. The standing wave potential is generated by reflecting a blue-detuned

beam off the glass surface from the vacuum side [57]. Incident at an angle  $\theta_{SW}=76^{\circ}$  from the normal, the trap minima in the resulting potential are planes parallel to the surface and are spaced by  $\sim 1.5 \mu \text{m}$ . We reliably load all of the atoms into a single node of the standing wave, as the spread of the wavefunction ( $z_{ho}=250 \text{nm}$ ) in the pure EW trap is much smaller than the spacing of the SW planes. The axial trap frequency, verified by parametric excitation measurements, is increased to  $7 \pm 0.1 \text{kHz}$  in this trap, taking us deep into the 2D regime. We populate the second node of the SW at a distance of  $\approx 3 \mu \text{m}$  from the surface.

One problem encountered with the evanescent wave surface trap was the change of the barrier height over time due to adsorption of condensates onto the glass surface. Adsorbed metal atoms on the surface form small electric dipoles. Inhomogeneities in the distribution of these dipoles generate potential gradients which can be stronger than the inherent van der Waals force of the substrate. This process is quite well understood [127] and the fields generated decay very rapidly away from the surface. However, at the distance we operated at, the potentials were strong enough to cause a significant change in the trap characteristics after loading several hundred clouds.

The diffusion time-scale of these adsorbates has been shown in previous experiments to be on the scale of days to weeks and can be strongly decreased by an increase in surface temperature [136]. However since heating is impractical for our purposes, we opted to switch to a different method of preparing a two-dimensional cloud that still utilizes the surface for referencing the trapping potentials relative to each other and to the imaging system, but allows us to have the cloud at a much larger distance from the surface, where the effect of the adsorbates is negligible.

#### 4.2.2 Two-stage standing wave trap

The second generation method for creating 2D condensates begins by transferring the cloud from the cigar trap into a single well of a 1D standing wave with periodicity  $9.2\mu m$  created by a beam reflected off the glass substrate. The light for this standing wave is centered at 755nm, has a 3nm spectral width and is incident at an angle of  $2.3^{\circ}$  relative to the surface. The condensate is loaded into the first nodal plane from the surface. The harmonic oscillator width of the condensate at full lattice depth along the direction perpendicular to the surface is 360nm. By increasing the bias field the confinement in the 2D plane is relaxed, resulting in an elliptic cloud with Thomas-Fermi radii  $(18, 36)\mu m$  in the 2D plane.

The next stage further increases the axial confinement by transferring into the  $1.5\mu$ m lattice described in the previous section. However, the condensate now resides in the sixth well from the surface. At this point, the  $9.2\mu$ m standing wave is ramped down. The surface provides a reproducible way to overlap the nodes of these two standing waves as well as enhancing the numerical aperture of the imaging system as described in Sec. 4.5.

#### 4.2.3 Theory of two dimensional condensates

In this section, we briefly summarize the theory of two-dimensional condensates relevant to our work. In an infinite two-dimensional spatially homogeneous system, a Bose-Einstein condensate can only exist at T=0 because long-wavelength phase fluctuations destroy the condensate at any finite temperature [122]. However, in a trapped system, there is a lower momentum cut-off for the fluctuations due to the

finite size of the cloud, and true Bose-Einstein condensation at finite temperature is possible [143]. The transition temperature  $T_c$  is on the order of  $N^{1/2}\hbar\omega_r$ , where N is the number of atoms and  $\omega_r$  is the trapping frequency in the plane of the condensate.

A two-dimensional condensate forms in the regime  $\omega_z \gg U \gg \omega_r$  where  $\omega_z$  is the axial trap frequency and U is the interaction energy. In a harmonic trap, the condensate wavefunction can be factorized into radial and axial parts  $\psi(r,z) = \psi_r(r)\psi_z(z)$ . The condensate occupies the lowest energy eigenstate of the axial potential given by the usual harmonic oscillator wavefunction

$$\psi_z(z) = \left(\frac{1}{\pi z_0^2}\right)^{\frac{1}{4}} e^{-\frac{z^2}{2z_0^2}} \tag{4.1}$$

with  $z_0 = \sqrt{\hbar/m\omega_z}$ . In the radial direction, the Thomas-Fermi approximation of neglecting the kinetic energy compared to the interactions is justified, and the Gross-Pitaevskii equation reduces to

$$\left(g|\psi_r(r)|^2|\psi_z(z)|^2 + \frac{1}{2}m\omega_r^2 r^2\right)\psi_r(r)\psi_z(z) = \mu\psi_r(r)\psi_z(z) \tag{4.2}$$

where  $\mu$  is the radial chemical potential and g is the interaction strength given by  $4\pi\hbar^2 a_s/m$ , with  $a_s$  being the s-wave scattering length. Applying  $\int dz \ \psi_z^*$  to both sides, we obtain an effective 2D interaction  $g_{2D} = g/\left(\sqrt{2\pi}z_0\right)$ . The Thomas-Fermi profile of the 2D density is  $n_{2D}(r) = |\psi_r(r)|^2$ 

$$n_{2D} = \max\left(\frac{\mu - \frac{1}{2}m\omega_r^2 r^2}{g_{2D}}, 0\right)$$
 (4.3)

The chemical potential is set by the condition  $\int dxdy \ n_{2D}(r) = N$  where N is the atom number:

$$\mu = \sqrt{\frac{m\omega_r^2 N g_{2D}}{\pi}}. (4.4)$$

The Thomas-Fermi radius of the cloud defined through  $\mu = \frac{1}{2} m \omega_r^2 R_{TF}^2$  is

$$R_{TF} = \left(\frac{4Ng_{2D}}{\pi m\omega_r^2}\right)^{1/4}.\tag{4.5}$$

For typical parameters of N=1000,  $\omega_z=2\pi\times7\mathrm{kHz}$ ,  $\omega_r=2\pi\times10\mathrm{Hz}$ , this yields a Thomas-Fermi radius of  $14\mu\mathrm{m}$  or  $\sim20$  lattice sites at a lattice spacing of 680nm.

#### 4.3 Using a dimple for producing small cold clouds

In order to obtain a suitable initial density for creating a Mott insulator, the atom number in the 2D plane must be reduced to a few thousand atoms in a reproducible way. With RF evaporation, it is hard to achieve small, reproducible atom numbers because of the difficulty of controlling fluctuations of the magnetic trap bottom to much better than chemical potential of the condensate. Instead, we use the "dimple trick" introduced in [146, 86, 180], where atoms from the center of the condensate are trapped in small volume dipole beam and the rest of the atoms are discarded. A red-detuned ( $\lambda = 840$ nm) beam is focused through the objective to an  $8\mu$ m waist centered on the cloud, creating a dimple potential in the magnetically confined cloud as shown in Figure 4.2. The magnetic confinement is then removed and the number of atoms remaining in the dimple trap is proportional to its depth, with a residual RMS fluctuation of 6%. A second collinear 840nm beam with a 27 $\mu$ m waist and 12nm

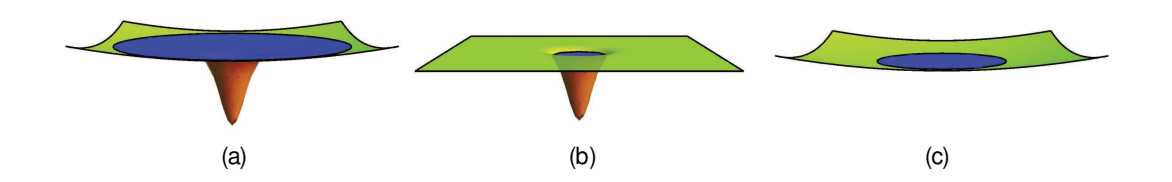


Figure 4.2: Control of atom number and temperature with a dimple potential. A small focused beam creates a dimple potential in the center of a large magnetically trapped condensate. A small fraction of the atoms are loaded into this potential, controlled by the depth of the potential. The magnetic trap is then switched off, and after a short time, only the cold atoms within the dimple remain. A large waist optical dipole trap is ramped up and the dimple is ramped down, allowing the condensate to adiabatically expand, providing a suitable initial density for further experiments.

spectral width is then turned on, and the dimple is adiabatically ramped down to expand the cloud into the larger beam. The transverse confinement of the condensate provided by this beam is 9.5Hz.

If the dimple trap is aligned such that it selects atoms out of the center of the condensate, entropy is removed when the magnetic trap is switched off because the coldest atoms are at the center. If the dimple is then adiabatically converted into the larger dipole trap, the temperature of the final cloud should be lower than that of the initial condensate.

## 4.4 Incoherent light sources for producing clean optical potentials

Uncontrolled spatial fluctuations of the potential experienced by atoms are often present in optical traps. In optical lattices, disorder is a concern when the RMS site to site fluctuations  $\delta$  are on the order of U (Sec. 5.2.4), or in some experiments, even

on order of the tunneling (Sec. 6.2.3). Disorder can be either due to onsite offsets or variations of the vibrational frequencies. Typically, the lattice depth and frequencies are several 10kHz, while U is several hundreds Hertz. This dictates potential uniformity on the percent level. Most lattice experiments use coherent light for creating the potentials. In this case, stray light on the  $10^{-4}$  level leads to 4% peak-to-peak corrugations due to the heterodyning effect of light interference, which makes creation of clean lattice potentials challenging. These issues are of particular relevance in our experiment because of in-vacuum glass surfaces that are close to that atoms, as well as the new projection technique (Sec. 4.5.2) we use to create the lattice.

We preclude the possibility of interference between the lattice light and most of the stray light from reflections, dust and surface imperfections by using "white" light with a very short coherence length. The desired interference used in creating the lattices is still present because of the particular techniques we use to create the lattices. The 2D lattice is created by projection through the high NA imaging system, which automatically ensures that the path lengths for the interfering beams is the same. In the case of the standing wave traps created by reflecting beams off the surface, the remaining coherence length of the broadband light is still larger than the interfering distance  $2d/\cos\theta_{SW}$  for atoms located a distance d from the surface.

We have investigated two different sources for generating high power temporally incoherent light. The first is a tapered amplifier system (Eagleyard Photonics) seeded with light from a fiber coupled amplified spontaneous emission (ASE) source (Exalos, Superlum). Interference filters are used to control the bandwidth of the white light source as well as to suppress resonant ASE components. For the 1D standing wave

traps, the light is blue-detuned, centered around a wavelength of  $\lambda_{trap} = 755$ nm with a spectral width of 3nm, corresponding to a coherence length of about  $100\mu$ m. This is short enough to suppress the interference effects of stray light from multiple reflections and other parts within the setup, e.g. from the curved surface of the hemispheric lens or from glass cell surfaces. The red detuned beams used in creating the dimple trap and transverse confinement dipole trap are centered at 840nm with a spectral width of 1nm.

A second source we have also used is a mode-locked laser (Coherent MIRA-HP) which is used to generate a similar spectrum to the tapered amplifiers. A pulse-stretcher is required after the laser to avoid non-linear broadening of the spectrum after passing through a single-mode fiber.

#### 4.5 Quantum gas microscopy

In this section, we describe our technique for fluorescence imaging of atoms on resolved sites of a Hubbard regime optical lattice. Similar optical imaging of single thermal atoms has been demonstrated in lattices with large spacings ( $5\mu$ m period) [131] and in sparsely populated one-dimensional arrays [102]. Imaging of 2D arrays of "tubes" with large occupations has been shown for smaller spacings with an electron microscope [71] and optical imaging [95] systems.

#### 4.5.1 High numerical aperture imaging

The central part of the set-up is the high resolution optical imaging system integrated with the 2D atom trap. The imaging system consists of a long working distance microscope objective located outside the vacuum chamber which covers a numerical aperture of NA=0.55. As an additional front lens of this imaging system, a hemispheric lens (4mm radius) is placed inside the vacuum. With the quantum gas placed only a few micrometers from the superpolished flat bottom surface of the hemisphere, a "solid-immersion" [126] effect occurs, which increases the numerical aperture by the index of refraction of the hemisphere lens to NA=0.8, yielding a diffraction limit of  $\sim 600$ nm (FWHM) at an imaging wavelength of 780nm. A drawing of the lens configuration is shown in Figure 4.3(a). The objective was aligned interferometrically to the in-vacuum hemisphere by sending a plane wave through the objective and interfering the returning plane wave reflected from hemisphere with the incoming beam. The resulting interferogram is shown in Figure 4.3(b) showing wavefront distortion less than  $\lambda/4$ .

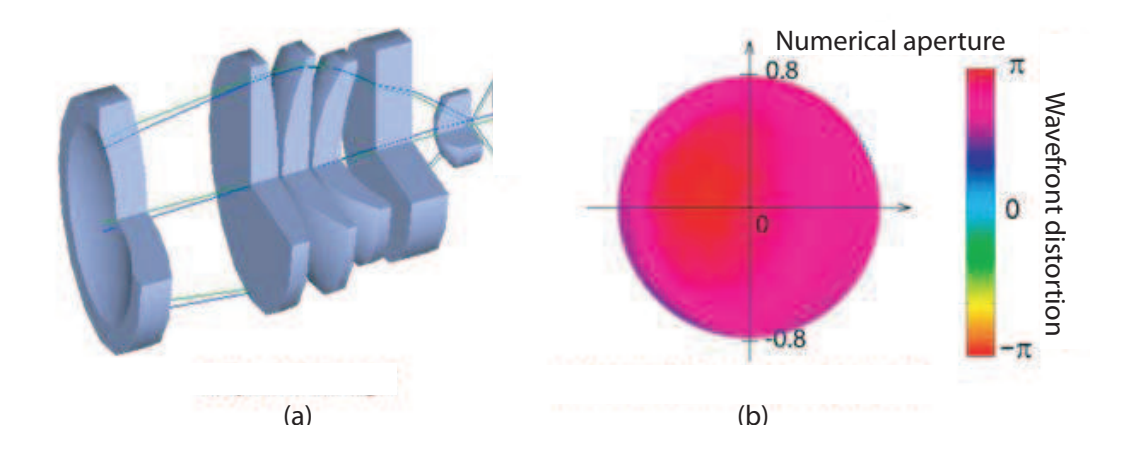


Figure 4.3: High resolution optics for single atom imaging. (a) Five element custom objective that is corrected for a 5mm thick glass cell window, combined with a hemispheric in-vacuum lens to obtain an imaging system with NA = 0.8. (b) Interferogram characterizing aberrations of the imaging system.

The objective is designed to be diffraction-limited for an object point at the center

of the in-vacuum hemispheric lens. In the case of the evanescent wave trap, the atoms reside  $3\mu$ m from the surface. At this position, the geometric spot size due to aberrations is roughly half the diffraction-limited spot size of 600nm at  $\lambda=780$ nm. However at  $10\mu$ m from the surface, as is the case with the two-stage standing wave trap, the geometric spot size is double the diffraction-limited spot size. To address this issue, we calculated the wavefront aberration using a raytracing program (OSLO, Lambda Research) and decomposed it into its Zernike polynomials.  $Z_2$  aberrations can be corrected by changing the distance between the imaging lens and the CCD, but higher order aberrations ( $Z_4=0.30, Z_6=0.03$ ) cannot be corrected this way. We designed a 0.5mm thick fused silica correction plate with a thickness profile, shown in Figure 4.4, that corrects the higher order aberrations when inserted right after the objective. The plate was manufactured by LightMachinery Inc. using fluid jet polishing.

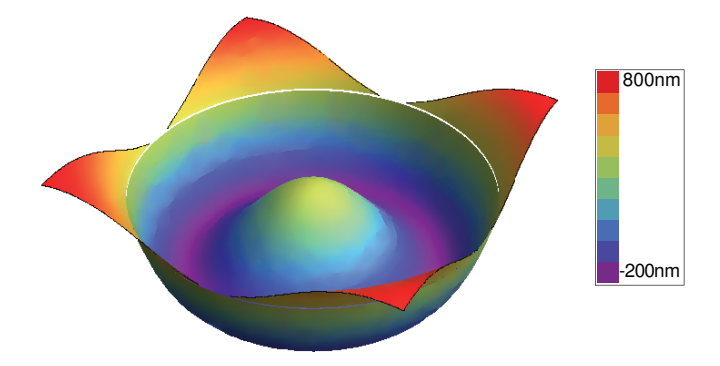


Figure 4.4: Aberration correction plate. The imaging system is designed for atoms positioned at the glass surface. In our second generation trap, the atoms reside  $10\mu m$  from the surface, and a corrector plate is need to compensate for aberrations described by fourth and sixth order Zernike polynomials.

#### 4.5.2 Optical lattice projection

The periodic potentials in the 2D plane are created by using the microscope optics to make a direct projection of a lithographically produced periodic mask that contains the lattice structure in the form of a phase hologram [80, 132, 22, 31]. This is in contrast to conventional optical lattice experiments in which lattice potentials are created by superimposing separate laser beams to create optical standing waves. The advantage of the new method is that the geometry of the lattice is directly given by the pattern on the mask. The imaged light pattern, and hence the potential landscape, can be arbitrary within the limits set by the available imaging aperture and by polarization effects that can arise due to the large aperture imaging beyond the paraxial limit. In this work, we have used the projection to create a blue detuned square lattice potentials with a periodicity a = 680nm. A major additional advantage is the fact that the lattice geometry is not dependent on the wavelength [31], apart from diffraction limits and chromatic aberrations in the lens for large wavelength changes. This allows us to use the broadband light sources we have previously described. It also enables us to dynamically change the wavelength of the lattice light without changing the lattice geometry.

For the experiments in this work, we use two binary phase holograms to create sinusoidal potentials along the x and y axes respectively (Fig. 4.5). The holograms are illuminated with linearly polarized light, polarized perpendicular to the plane of diffraction. The two light paths are combined with a polarizing beam splitter cube. The far off-resonant lattice is created with light from a femtosecond laser, with a spectral width of 3nm centred at 758nm. The lattice potential produced by the

holograms is given by  $V(x,y) = V_0 \left( \sin^2(kx) + \sin^2(ky) \right)$ , where the periodicity of the lattice is given by  $a = \pi/k = 640$ nm and  $V_0$ , the depth of the potential, can reach up to  $50E_r$ .

For imaging, we increase the lattice depth to  $5500E_r$  (0.38mK) by illuminating the lattice holograms with light from a continuous wave Ti:sapphire laser detuned 32GHz to the blue of the D1 transition of  $^{87}$ Rb, without changing the lattice geometry. This pinning lattice is linearly polarized everywhere to avoid effective magnetic fields that interfere with the polarization gradient cooling during imaging. This is achieved using the proper choice of polarizations and by introducing frequency differences of at least 80MHz between lattice axes to time average the interference between them. Near resonant light from the same source is used to simultaneously increase the lattice depth in the axial direction to 3mK.

#### 4.5.3 Fluorescence imaging of single atoms

The main use of the microscope set-up is the collection of fluorescence light and high-resolution imaging of the atoms. With the atoms pinned in the deep lattice, we illuminate the sample with red detuned near-resonant light in an optical molasses configuration, which simultaneously provides sub-Doppler cooling [193, 194, 172]. The molasses beams are detuned 80MHz to the red of the F=2 to F'=3 transition of the D2 line, where F and F' denote the hyperfine manifold in the ground and excited state, respectively. One beam enters from the y axis and is reflected off the trapping surface at an angle of  $15\mu$ m and then retroreflected with perpendicular polarization along the same path. This results in polarization and intensity gradients along the

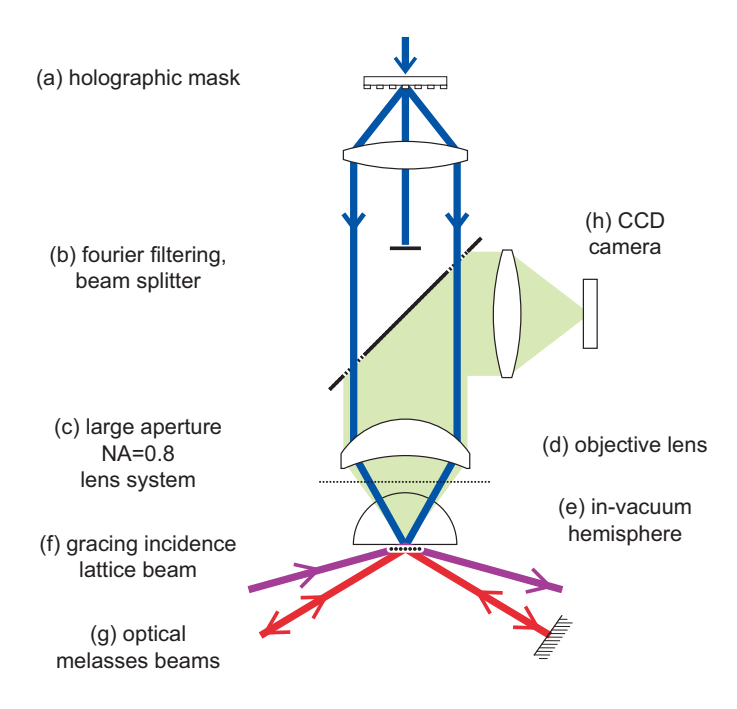


Figure 4.5: Diagram of the quantum gas microscope. The 2D atom sample (a) is located a few microns below the lower surface of an in-vacuum hemispheric lens. This lens serves to increase the numerical aperture of the objective lens outside the vacuum (b). The atoms are illuminated from the side by the molasses beams (c) and the scattered fluorescence light is collected by the objective and projected onto a CCD (d). A 2D optical lattice is generated by projecting a periodic mask (e) onto the atoms through the same objective via a beam splitter (f). The mask is a periodic phase hologram, and a beam stop (g) blocks the residual zeroth order, leaving only the first orders to form a sinusoidal potential.

y direction and the vertical. An additional beam enters along the x axis which generates polarization gradient components along this axis by interference with the retroreflected beam. In addition, to avoid cooling inefficiencies due to low polarization gradients on some lattice sites, we frequency offset the molasses beams by 7kHz for temporal averaging of the cooling pattern. The photons scattered by the optical molasses are collected for fluorescence detection of the atoms. The solid angle of the imaging system leads to a collection efficiency of 20%, such that we expect a total

photon collection efficiency of  $\sim 10\%$  including the quantum efficiency of the CCD camera (Andor Ixon DU888). The effective pixel size in the object plane is 167nm.

Figure 4.6(a) shows a typical image obtained by loading the lattice with a very dilute cloud, showing the response of individual atoms. The spot function of a single atom can be directly obtained from such images. We measure a typical single atom emission FWHM size as 570nm and 630nm along the x and y direction, respectively, which is close to the theoretical minimum value of 520nm (Fig. 4.6(b)). This minimum is given by the diffraction limit from the objective combined with the finite size of the camera pixels and the expected extent of the atom's on-site probability distribution within the lattice site during the imaging process. As the same high-resolution optics are used to generate both the lattice and the image of the atoms on the CCD camera, the imaging system is very stable with respect to the lattice, which is important for single-site addressing [195, 188]. The observed drifts in the 2D plane are very low, less than 10% of the lattice spacing in one hour with shot to shot fluctuations of less than 15% r.m.s.

Pair densities within multiply occupied lattice sites are very high due to the strong confinement in the lattice. When resonantly illuminated, such pairs undergo light assisted collisions and leave the trap within a time of the order of  $100\mu$ s, long before they emit sufficient photons to be detected [48]. Therefore the remaining number of atoms per site is equal to the parity of the original atom number before illumination, as long as the initial occupation is small. For our molasses parameters, the collected number of photons can be up to  $2 \times 10^4$  per atom per second, and the exposure times are typically between 200 and 1000ms, limited by the loss of single atoms from

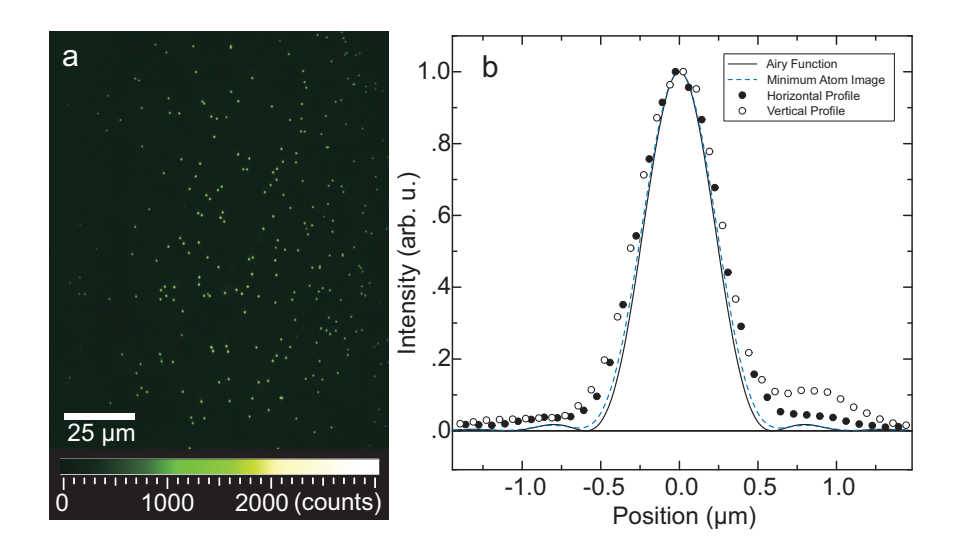


Figure 4.6: Imaging single atoms. (a) Field of view with sparse site occupation. (b) Response of a single atom, derived from sparse images: shown are horizontal (filled circles) and vertical (open circles) profiles through the centre of the image generated by a single atom. The black line shows the expected Airy function for a perfect imaging system with a NA = 0.8. The blue dashed line denotes the profile expected from a single atom, taking into account only the finite width of the CCD pixels and the finite extension of the probability distribution of the atom's location. The data are from the responses of 20 atoms in different locations within the field of view which have been precisely superimposed by subpixel shifting before averaging.

the trap which reduces the detection fidelity. The 1/e lifetime is  $\sim 30$  s, which is consistent with loss due to collisions with hot atoms in the background gas.

Figure 4.7 shows an image obtained by loading a dense Bose-Einstein condensate. The fast ramp-up of the pinning lattice within 1.5ms switches off tunnelling and projects the superfluid state wavefunction onto Poisson distributed on-site occupations with more than one atom per lattice site in the center of the trap. Owing to the removal of pairs the occupation detected is lowered, typically 42%. Figure 4.8 is a large field of view image, illustrating the capability to image tens of thousands of atoms simultaneously over an area of more than  $100\mu$ m without degradation of the

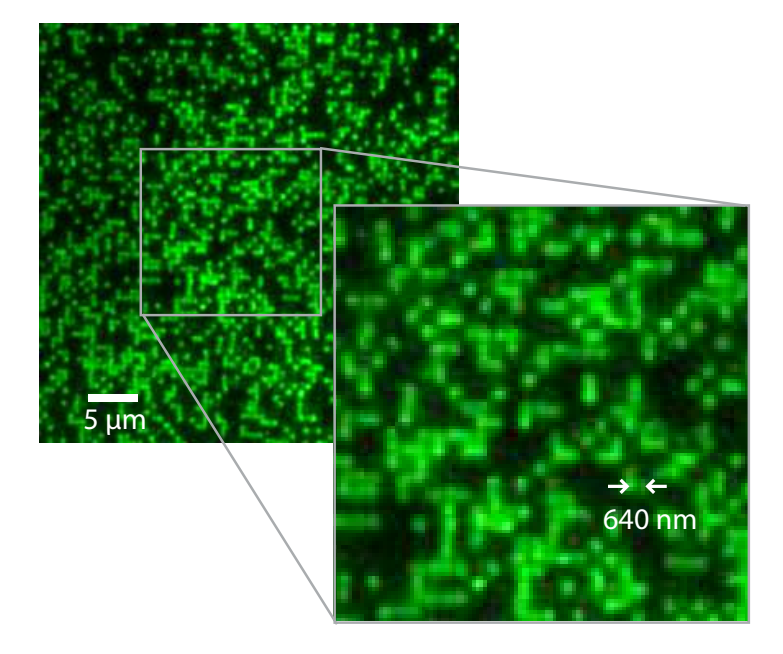


Figure 4.7: Site-resolved imaging of single atoms on a 640nm period optical lattice, loaded with a high density BoseEinstein condensate. Inset, magnified view of the central section of the picture. The lattice structure and the discrete atoms are clearly visible. Owing to light-assisted collisions and molecule formation on multiply occupied sites during imaging, only empty and singly occupied sites can be seen in the image.

resolution. The images are analyzed by identifying the lattice geometry and fitting point spread functions (obtained separately by analyzing images from sparsely filled lattices) to each lattice point. As the background signal is weak and smooth due to the 2D geometry, we thus obtain the total number of scattered photons per lattice site as a simple way of determining the presence of an atom.

Figure 4.9 shows the histogram of photon counts for the central region of several images with an average filling of 34%. For these pictures with long exposure times, the fidelity of identifying atoms at a given lattice site is 98%, limited by the losses occurring during the integration time. To verify that the atom distribution is preserved during imaging, we have recorded sequences of consecutive images spanning a



Figure 4.8: Large field of view image of a thermal cloud in a 640nm spacing lattice. The ability to identify individual atoms over the whole field of view shows that the resolution is good over an area of more than  $100\mu m$ .

total detection period of several seconds, during which no significant hopping occurs.

### 4.6 Image analysis for extracting the density distribution

The data extracted from the images is a digital 0/1 matrix with entries corresponding to whether we observe an atom on a site or not. In the section, we describe the image processing algorithms we use to obtain such a matrix.

First, a sparse atom cloud image is used to extract the point spread function of the imaging system (PSF). The geometry of the lattice is then extracted from such an image. The lattice spacing is obtained and then the region of interest is fitted in

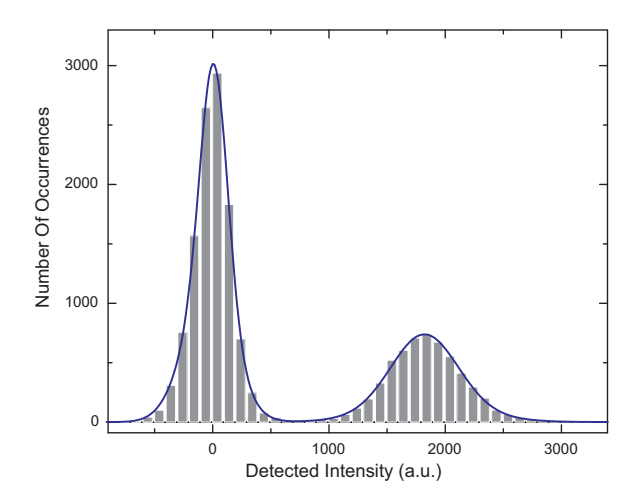


Figure 4.9: Histogram showing the brightness distribution of lattice sites for an exposure time of 1 s. The left peak corresponds to empty sites (background subtracted), the right peak to those occupied by a single atom. The blue line denotes a fit to the data using a double Gaussian function for each of the two peaks. a.u., arbitrary units.

blocks of 10 by 10 lattice sites. The block centers are allowed to vary to extract any distortions of the lattice pattern due to imaging aberration over the field of view. A histogram of atom brightness is used to set a threshold that identifies the presence or absence of an atom on a site. The information about the PSF, lattice geometry and threshold obtained from these sparse images is then used to fit other images with much higher lattice filling, only allowing for a single global offset in the lattice phase determined by fitting atoms at the edges of the cloud.

During imaging, a small fraction of the atoms are lost due to background gas collisions. If this occurs before they scatter enough photons to surpass the detection threshold, they are not counted. For a 1s exposure, the mean fraction of such uncounted atoms is  $1.75 \pm 0.02\%$ , determined from 15 movies (30 frames, 0.5s exposure per frame) of the atom population decay in the near-resonant lattice.

In some cases, we are not interested in the in-situ lattice occupations, but rather the total atom number in the cloud. The parity imaging does not allow extraction of atom number from in-situ images. Instead, atom numbers are measured by switching off the transverse confinement and letting the cloud expand in the 2D plane before turning on the deep lattice used for fluorescence imaging. This ensures that the probability of two atoms being on the same site is negligible, avoiding photo-assisted losses for very accurate atom number determination.

### 4.7 Arbitrary potential landscapes with spatial light modulators

In addition to imaging, we have also used the high NA optics to project light patterns onto the cloud. This allows both manipulation of the atoms (Sec. 6.6) as well as engineering the potential landscape with high spatial resolution (Sec. 5.2.4). In particular, for landscape engineering, we illuminate a digital micromirror device (DLP Discovery 4100, Texas Instruments) with incoherent light of spectral width 1nm, centered at 840nm. The light pattern after the DLP is imaged onto the atoms. A block of  $14 \times 14$  mirrors maps onto a single lattice site in the plane of the atoms, allowing the creation of grayscale patterns, with the aperture of the objective providing Fourier filtering. An error diffusion algorithm [120] is used to convert the desired grayscale image to a binary pattern. Potential corrections of either sign are possible by operating the micromirror device with a bias light level produced by flattening the profile of the Gaussian illumination beam.

#### 4.8 Site-resolved modulation spectroscopy

Lattice modulation spectroscopy involves sinusoidal modulation of the depth of an optical lattice to probe the excitation spectrum of an atomic many-body system that resides in the lattice (see for example [78, 166, 54, 169]). The modulation mainly changes the tunneling J rather than the interaction U. The dependence of tunneling on lattice depth can be approximated by

$$J \sim E_r \left(\frac{V}{E_r}\right)^{3/4} e^{-2\sqrt{\frac{V}{E_r}}} \tag{4.6}$$

For a time dependent potential depth  $V(t) = V_0 + \delta V \sin \omega t$ , tunneling also varies sinusoidally for small  $\delta V$ :  $J(t) = J_0 + \delta J \sin \omega t$ , with  $\delta J$  given by

$$\delta J = J_0 \delta V \left( \frac{3}{4V_0} - \frac{1}{\sqrt{V_0 E_r}} \right). \tag{4.7}$$

If the many-body state we are studying with lattice modulation is, for example, a Mott insulator, the tunneling modulation above provides a matrix element connecting the lowest Hubbard band containing no excitations to the first band with a single doublon/hole excitation. Deep in the Mott regime, the excitation is induced by modulating at  $\omega = U/\hbar$ . More usefully, modulation spectroscopy can measure the many-body energy gap all the way across a phase transition.

In most experiments to date, the excitations introduced by modulation spectroscopy are probed as a broadening of the diffraction peaks for states with global coherence such as superfluids, or by adiabatically transferring the system to such a state after the modulation if the initial state is different (e.g. a Mott state or Bose glass). Site resolved imaging allows us to directly study the excitation spectrum of states with density or spin spatial ordering. In addition, spectrum features obtained from *in-situ* modulation spectroscopy can be much narrower than traditional techniques by focusing on a small part of the cloud to avoid averaging over large scale potential inhomogeneities.

As an example, we show a spectrum (Fig. 4.10(a)) obtained by modulation spectroscopy of a Mott insulator with one atom per site in a linear gradient characterized by a potential difference E between neighbouring lattice sites. Excitations are introduced into the system at frequencies U + E and U - E corresponding to creating single excitations by hopping up or down the gradient. The excitations are observed as a reduction in the averaged probability of observing an atom on a site during the imaging  $(p_{\text{odd}})$ , because the doublons and holes produced are both not detected by parity imaging.

Such spectra were used in calibrating the gradients applied in the experiments of Chapter 6. In a harmonic trap, the local gradient E varies across the cloud, which usually leads to broadening the peaks to several hundred Hertz for traditional modulation spectroscopy (e.g. [78]). In this case, by doing the spectroscopy on a few sites, the features observed are much narrower, with residual power broadening.

Figure 4.10(b) shows data illustrating the precision measurement capability of *in-situ* modulation spectroscopy. The three modulation spectra shown were all taken using atoms in the same region at the center of the trap. For the different spectra, the atom number was changed to have shells with 1, 2 or 3 atoms per site in that region. In this case, the resonances curiously occur at different center frequencies in

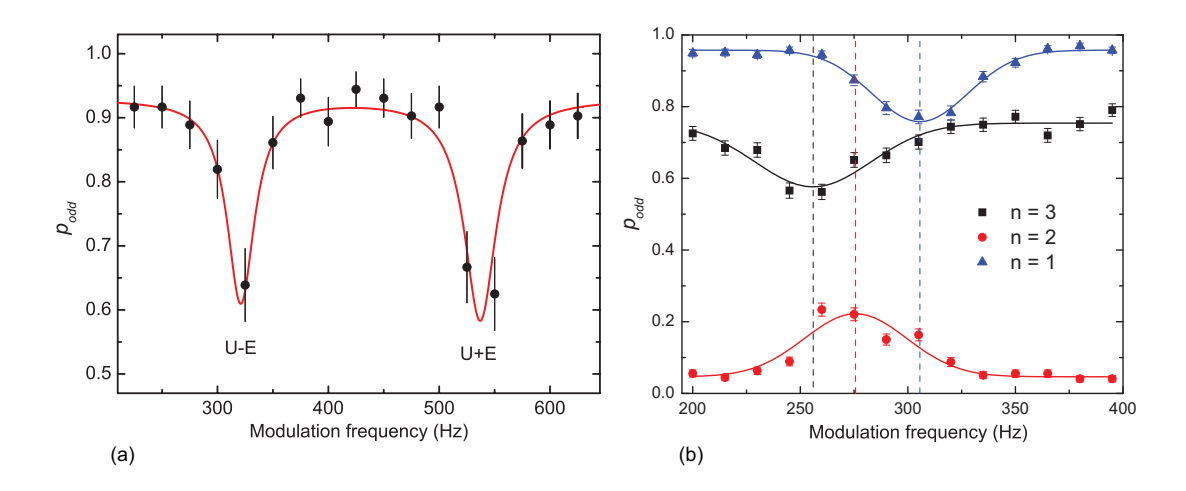


Figure 4.10: Site-resolved modulation spectroscopy. (a) Modulation spectroscopy in a tilted lattice. The occupation probability, plotted versus the modulation frequency, for  $16E_r$  longitudinal lattice modulated by  $\pm 23\%$ , corresponding to a Bose-enhanced resonant tunneling rate of  $2\pi \times 4$  Hz. Because the experiment is performed in a lattice tilted by E per site, the peak at zero tilt which appears at the interaction energy U is split out into two peaks, one corresponding to an atom tunneling up the tilt at an energy cost of U + E, and one to tunneling down the tilt a cost of U - E. Fitting these peaks allows us to extract both U and E. The peak width arises from a combination of power broadening (approximately  $2\pi \times 14$  Hz, complicated by Rabi hopping), and residual lattice disorder. (b) Three-body interaction shifts observed in the modulation spectra in a tilted lattice. The peaks for n = 1, 2, 3 are at 307 Hz, 276 Hz and 256 Hz respectively.

the different shells. One expects that an excitation in a shell with n atoms per site produces n+1 and n-1 atoms on two lattice sites. The final state has an energy of  $\frac{1}{2}U(n+1)n+\frac{1}{2}U(n-1)(n-2)$ , while the initial state has an energy Un(n-1) for the two sites of interest. In this simple picture, the energy difference is U in any shell. There are many corrections to this picture that contribute to the shift of the resonances in the different shells, but the dominant one is multi-orbital effects [191, 100]. For example, when three atoms are on the same site, the presence of interactions broadens their Wannier wavefunctions which reduces their pairwise interaction energy relative

to having just two atoms on the same site. This can be understood in terms of virtual transitions to higher bands which are not included in the single-band Hubbard model. The corrections to the onsite energy can be written as

$$E_n = \frac{1}{2}U_2n(n-1) + \frac{1}{6}U_3n(n-1)(n-2) + \frac{1}{24}U_4n(n-1)(n-2)(n-3) + \dots$$
 (4.8)

where  $U_n$  is an effective *n*-body interaction. To first order, this predicts that the second and third Mott shells would shift relative to the first by  $U_3$  and  $2U_3$ , with  $U_3 \approx -20$ Hz for our parameters.

#### 4.9 Noise correlation measurements

Phases with density or spin ordering can be detected in time of flight by measuring higher order correlations of the momentum distribution [2]. This technique has been used to detect pair correlations between atoms in a Fermi gas [76] as well as bosonic bunching [60] and fermionic antibunching [157] in a lattice, to study the superfluid to Mott transition in 2D [179] and has been suggested as way to detect antiferromagnetic ordering in a lattice [32]. In principle, resolved-site measurements make noise-correlations measurements obsolete, but the parity detection in our experiment has made the use of noise correlations necessary in some cases to detect density wave ordering where the parity is constant throughout the density wave (Sec. 6.2.2).

We explain noise correlations in the context of the experiments described in Chapter 6 and highlight the advantage of high resolution imaging in obtaining noise correlation data. In those experiments, a 1D density wave was prepared with alternating 0 and 2 occupancy in a lattice. A 1D expansion was performed by allowing the atoms to expand in the tubes while they remained confined in the other two directions. The atoms were pinned after the time of flight and imaged in fluorescence. The noise correlation signal is given by a normalized density-density correlation

$$C(d) = \frac{\int \langle n(x)n(x+d)\rangle dx}{\int \langle n(x)\rangle \langle n(x+d)\rangle dx}$$
(4.9)

where n(x) is the density at position x after time of flight and the brackets denote averaging over many images. This signal is 1 for uncorrelated atoms. After obtaining the occupation 0/1 vector of the 1D expanded system, we extract the noise correlation signal as described in Ref. [60]. We compute autocorrelation function by Fourier-transforming the individual vectors, taking the absolute square to obtain the power spectral density and Fourier-transforming back. We then average the autocorrelation over realizations to obtain the numerator of Eq. 4.9. Finally, we then compute the denominator from the autocorrelation of the average of all the vectors.

With bosons, the noise correlation experiment yields a signal that is enhanced above 1 because of a two-particle wavefunction interference. Each pair of atoms can be detected by a pair of detectors in two ways, which interfere constructively for bosons leading to bunching. The "detectors" in this case are the lattice sites of the pinning lattice in which the atoms are imaged. The signal directly probes correlators of the form  $\langle a_k^{\dagger} a_m^{\dagger} a_l a_n \rangle$  where  $a_k^{\dagger} (a_k)$  creates (destroys) a boson on site k. In a Mott state with occupany  $n_k$  on the kth site, this correlator evalutes to

$$\langle a_k^{\dagger} a_m^{\dagger} a_l a_n \rangle = n_k n_m \delta_{kl} \delta_{mn} + n_k n_m \delta_{kn} \delta_{lm} \tag{4.10}$$

where the two terms correspond to the two detection paths.

The correlation signal can be shown to scale as

$$C(d) - 1 \sim \frac{1}{N} \left(\frac{l}{\sigma}\right)^D$$
 (4.11)

where N is the number of atoms, D is the number of dimensions in which the measurement is done,  $\sigma$  is the size of the noise correlation bins, usually limited by the point spread function of the imaging system and  $l = \frac{ht_{TOF}}{ma}$ . Here  $t_{TOF}$  is the time of flight and a is the wavelength of the density wave. With our technique, the atom number can be precisely obtained after expansion with single atom precision, allowing post-selection against atom number fluctuations. More importantly,  $\sigma$  is a single site in our system, greatly enhancing the noise correlation signal and reducing the number of shots required to obtain it. Previous experiments have observed C(d)-1 are below the  $10^{-3}$  level [60]. The signals we observe in Sec. 6.2.2 are  $\sim 500$  times larger.

# Chapter 5

# Microscopy of the

# superfluid-insulator quantum phase

### transition

Publications based on the work described in this chapter:

"Probing the Superfluid-to-Mott Insulator Transition at the Single-Atom Level", W. Bakr, A. Peng, M. Tai, R. Ma, J. Simon, J. Gillen, S. Foelling, L. Pollet and M. Greiner, Science **329**, 547-550 (2010)

Microscopic measurements can reveal properties of complex systems that are not accessible through statistical ensemble measurements. Previous ultracold quantum gas experiments have studied the superfluid to Mott transition in an optical lattice using bulk measurements [78, 101, 165] that probe global properties such as coherence and compressibility, or local measurements that are coarse-grained over several lattice sites [66]. We present the first single atom-single site study of this quantum phase transition [56]. The microscopic measurements provide direct access to the evolution

of the onsite number distribution across the phase transition, and allow us to study local adiabaticity timescales for the formation of the Mott insulator. In addition, we identify particularly low entropy domains in the Mott insulator and obtain high contrast images of the shell structure.

#### 5.1 Number squeezing across the phase transition

In the weakly interacting superfluid regime, the many-body wavefunction factorizes into a product of states with well-defined phase on each lattice site, known as coherent states [74], with Poissonian number fluctuations. A coherent state on the jth site is an eigenvector of the annihilation operator on that site:  $a_j |\alpha_j\rangle = \alpha_j |\alpha_j\rangle$ , where the classical field  $\alpha_j$  is given by

$$\alpha_j = \sqrt{\overline{n}_j} e^{i\phi_j}. \tag{5.1}$$

Here  $\overline{n_j}$  is the mean atom number of the site and  $\phi_j$  is the macroscopic phase. The state can be expressed in a basis of Fock states as

$$|\alpha\rangle = e^{-|\alpha|^2/2} \sum_{n} \frac{\alpha^n}{\sqrt{n!}} |n\rangle$$
 (5.2)

from which the Poissonian atom number distribution immediately follows.

As the strength of the interaction increases, the number distribution is narrowed, resulting in a fixed atom number state on each site deep in the Mott insulator regime. This narrowing of the distribution is known as number squeezing [37], in analogy to

squeezing of the photon field encountered in quantum optics [124]. Number squeezing was previously studied indirectly in experiments [79, 69, 101], with the measurements averaged over several shells of superfluid and Mott insulating domains in the inhomogeneous system, complicating quantitative interpretation.

#### 5.1.1 Gutzwiller prediction for number squeezing

A prediction for the dependence of the onsite atom number distribution on the tuning parameter U/J can be obtained in the weakly interacting regime using a Gutzwiller approach [156, 112, 171]. The Gutzwiller ansatz is that the many-body wavefunction can be written as a product of wavefunctions on individual lattice sites

$$|\Psi\rangle = \prod_{i} |\psi_{i}\rangle \tag{5.3}$$

thus ignoring any possible correlations between lattice sites. The onsite wavefunctions are expanded in the atom number basis

$$|\psi_i\rangle = \sum_i f_n^{(i)}|n\rangle \tag{5.4}$$

where the amplitudes  $f_n^{(i)}$  for having n bosons on the ith lattice site are constrained by the normalization condition  $\sum_{n=0}^{\infty} |f_n|^2 = 1$ . The expectation value of the Bose-Hubbard Hamiltonian in the Gutzwiller wavefunction (eq. 5.3) is given by

$$\langle H \rangle = -Jz \left| \sum_{n} f_{n}^{*} f_{n+1} \sqrt{n+1} \right|^{2} + \frac{U}{2} \sum_{n} |f_{n}|^{2} n(n-1) - \mu \sum_{n} |f_{n}|^{2} n$$
 (5.5)

The number distribution is obtained by truncating  $f_n$  for atom numbers much larger than the mean atom number on a site and then minimizing the energy with the remaining amplitudes. Ref. [156] makes a further assumption that the amplitudes can be assumed to take a particular form

$$f_n = g^{n(n-1)/2} \frac{\overline{n}^{n/2}}{\sqrt{n!}} \tag{5.6}$$

where g is a variational "squeezing parameter", with the claim that any function that suppresses multiple occupancy for progressively higher atom numbers should produce similar results. Under this assumption and in the weakly interacting regime, the result obtained for the squeezing parameter g is

$$g \approx \frac{1}{1 + \frac{U}{2zJ}} \tag{5.7}$$

Figure 5.1(a) shows the theoretically calculated squeezing parameter as a function of U/J corresponding to various mean occupations in the superfluid phase, measured in atoms per lattice sites. The squeezing parameter starts at unity in the superfluid state since that corresponds to a coherent state and goes down as the distribution gets narrowed. At a given U/J, the squeezing parameter is higher for  $\langle n \rangle = 2$  than for  $\langle n \rangle = 1$  because quantum fluctuations are stronger in that case due to bosonic enhancement.

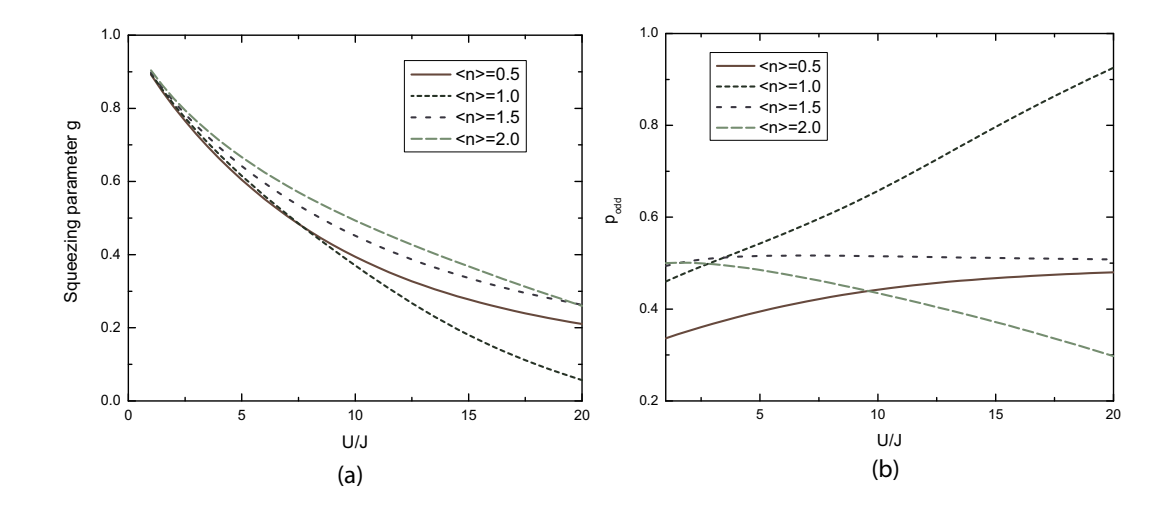


Figure 5.1: Gutzwiller prediction for atom number squeezing in a homogeneous system. (a) Squeezing parameter g and (b) probability of odd occupation on a lattice site plotted vs. U/J for various initial mean occupations in the superfluid. If the initial mean occupation in the superfluid is one (two) atoms per site with Poissonian fluctuations, the Mott insulating state at large U/J has exactly one (two) atoms per site with no fluctuations. Therefore, the  $p_{\rm odd}$  is one (zero).

#### 5.1.2 Parity detection of number squeezing

 $p_{\rm odd}$ .

Experimentally, the onsite number distribution can be probed by repeatedly preparing a sample in the lattice under identical conditions and measuring the atom number on that site. As a result of the measurement process, the many-body wavefunction is projected onto number states on each lattice site. In our experiments, we detect the parity of the atom number on a site (as described in Sec. 4.5.3) and repeated measurements can be used to deduce the probability of the site being oddly occupied,

For a coherent state on a lattice site with mean atom number  $\overline{n}$ ,  $p_{\text{odd}}$  is given by

$$p_{\text{odd}} = \sum_{n \text{ odd}} e^{-\overline{n}} \frac{\overline{n}^n}{n!} = \frac{1}{2} (1 - e^{-2\overline{n}}).$$
 (5.8)

This quantity is always less than 1/2, and therefore  $p_{\text{odd}} > 1/2$  is an indication of a non-Poissonian atom number distribution. On the other hand, in a Mott-insulating region in the zero temperature and zero tunneling limit,  $p_{\text{odd}}$  is 1 (0) for shells with an odd (even) atom number per site. Figure 5.1(b) shows  $p_{\text{odd}}$  as a function of U/J for various initial occupations in the superfluid based on the Gutzwiller calculation described in the previous section.

#### 5.1.3 Squeezing dynamics in the mean-field

Although the equilibrium properties of the Bose-Hubbard model are well understood, a theoretical understanding of the dynamics of the quantum phase transition, especially for a non-adiabatic change of the parameters, is still an active area of investigation. Studies of quenches from the superfluid to the insulator [109, 41] and vice versa have predicted interesting dynamics, including, in the latter case, order parameter oscillations due to the excitation of a gapped mode in the superfluid [1] and formation of topological defects realizing a quantum version of the Kibble-Zurek mechanism [46].

In this section, we will focus on the dynamics of the atom number distribution for non-adiabatic changes of the tuning parameter U/J. The calculation is done using a time-dependent Gutzwiller wavefunction truncated for onsite atom numbers larger than two [178]. The state of the system is assumed to be close to a Mott insulator with one atom per site so that the probabilities for having zero or two atoms per site are small and approximately the same by symmetry. The properly normalized wavefunction on a site is then written as

$$|\Psi\rangle = e^{-i\phi/2}\sin\theta \frac{|0\rangle + |2\rangle}{\sqrt{2}} + e^{i\phi/2}\cos\theta |1\rangle$$
 (5.9)

where  $\theta$  and  $\phi$  represent the remaining amplitude and phase degrees of freedom. The symmetric choice of phase between  $|0\rangle$  and  $|2\rangle$  lowers the energy. The mean-field Bose-Hubbard Hamiltonian on the *i*th lattice site is

$$H_{i} = -Jz \left( a_{i}^{\dagger} \langle a_{j} \rangle + \langle a_{j}^{\dagger} \rangle a_{i} \right) + \frac{1}{2} U n_{i} \left( n_{i} - 1 \right).$$
 (5.10)

Taking the expectation value of the annihilation operator a in the wavefunction described by Eq. 5.9, we obtain

$$\langle a \rangle = \frac{1}{\sqrt{2}} \cos \theta \sin \theta \left( e^{i\phi} + \sqrt{2}e^{-i\phi} \right)$$
 (5.11)

To find the values of the variational parameters that minimize the ground state energy, we minimize the expectation value of the self-consistent Hamiltonian in the variational wavefunction, which leads to  $\phi = 0$  and

$$Jz\left(3+2\sqrt{2}\right)\cos 2\theta = U. \tag{5.12}$$

The mean field transition point, defined by the interaction to tunneling ratio where

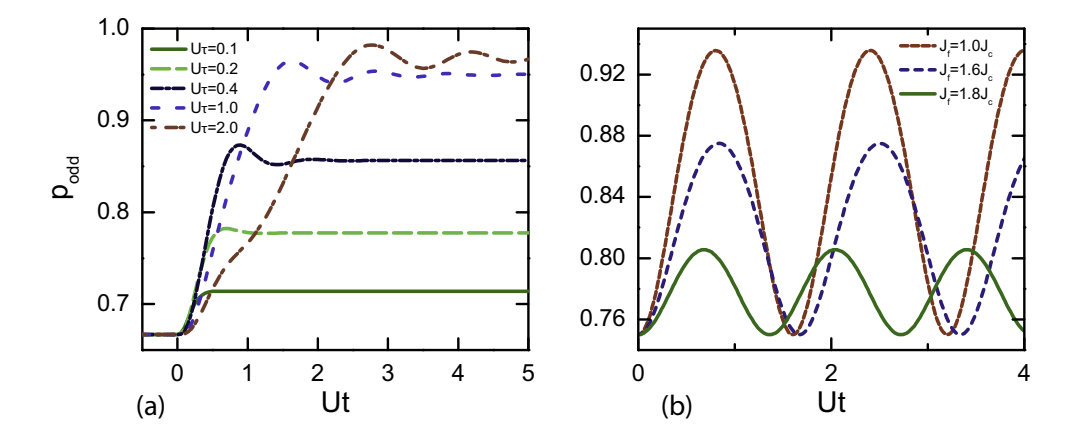


Figure 5.2: Atom number squeezing dynamics. The time evolution of  $p_{\text{odd}}$  is shown for (a) exponential ramps of U/J with various time constants  $\tau$  and (b) sudden quenches from  $J=2J_c$  to different lower values of the tunneling. Here  $J_c$  is the tunneling at the critical point. All calculations are done in the mean-field.

the onsite distribution is non-zero only for unit occupancy is given by

$$U/zJ_c = 3 + 2\sqrt{2}. (5.13)$$

We obtain the dynamics of the number distribution by solving the time-dependent Schroedinger equation  $id|\Psi\rangle/dt = H|\Psi\rangle$  using the mean-field Hamiltonian above. This leads to coupled differential equations for  $\theta$  and  $\phi$ 

$$\hbar \frac{d\phi}{dt} = -zJ(3 + 2\sqrt{2}\cos\phi)\cos 2\theta + U \tag{5.14}$$

$$\hbar \frac{d\phi}{dt} = -zJ(3 + 2\sqrt{2}\cos\phi)\cos 2\theta + U$$

$$\hbar \frac{d\theta}{dt} = -zJ\frac{\sin 2\theta}{\sqrt{2}}\sin\phi$$
(5.14)

which have the same stationary solution as Eq. 5.12. The probability of having one

atom on a lattice site (equivalent to  $p_{\text{odd}}$  in this case) is  $\cos^2 \theta$ . Figure 5.2(a) shows a plot of the time evolution of  $p_{\text{odd}}$  for an exponential ramp of J at fixed U while figure 5.2(b) shows oscillations of  $p_{\text{odd}}$  resulting from a sudden quench that reduces the tunneling. The latter case can be obtained by jumping the lattice depth.

#### 5.1.4 Mott insulators at finite temperature

At zero temperature, onsite atom number fluctuations arise from coherent quantum fluctuations that lead to the squeezed number distributions described in Sec. 5.1.1. However, at finite temperature, there are also thermal fluctuations. To elucidate the difference between the two kinds of fluctuations, we will focus on a Mott insulator with unit mean onsite occupation. At zero temperature and for small tunneling, we can write a perturbative many-body wavefunction

$$|\Psi\rangle \approx |\Psi\rangle_{MI} + \frac{J}{U} \sum_{\langle i,j\rangle} \hat{a}_i^{\dagger} \hat{a}_j |\Psi\rangle_{MI}$$
 (5.16)

where  $|\Psi\rangle_{MI}$  is a Mott state with one atom on every site. The tunneling creates an admixture of localized doublon-hole pairs. These have been shown [70] to contribute to residual coherence in the Mott insulator that manifests itself as a finite visibility of the interference pattern observed after free expansion. It is important to note that in this limit, the doublon-hole pairs are localized in the sense that an observation of a missing atom on a lattice site means that an extra atom has to appear on one of the neighbouring lattice sites.

Thermal fluctuations also lead to the appearance of doublons and holes on top

of an n=1 Mott insulator, but these are free to move around and are not paired. We can obtain the expected number distribution arising from thermal fluctuations by focusing on a Mott insulator in the atomic limit (J=0) at temperature T. In this limit, the energy per lattice site is given by  $E=\frac{1}{2}Un(n-1)$  and the grand canonical partition function truncated for onsite occupations above two is

$$Z = 1 + e^{\beta\mu} + e^{\beta(2\mu - U)} \tag{5.17}$$

where  $\mu$  is the chemical potential and  $\beta=1/k_BT$ , with  $k_B$  denoting Boltzmann's constant. From this, we immediately obtain  $p_{\text{odd}}=e^{\beta\mu}/Z$ . Near the tip of the Mott lobe where  $\mu\approx U/2$ , the defect ratio d in the Mott insulator, is d=2/Z, and can be used as an accurate thermometer down to zero temperature. Figure 5.3(a) is a plot  $p_{\text{odd}}$  vs. T/U which shows that Mott insulators with less that 1% defect ratios can be obtained for temperatures below T/U=0.08.

In many cases, entropy is a more useful concept than temperature when dealing with ultracold gases because most of the manipulations of the gas are isentropic rather than isothermal. For example, loading into an optical lattice, in the ideal case, preserves the entropy of the bulk gas while the temperature changes. The entropy S of the Mott insulator in the atomic limit can be obtained as the temperature derivative of the free energy  $S/k_B = \partial_T (T \ln Z)$  and  $p_{\text{odd}}$  is plotted vs. the entropy in figure 5.3(b).

The effect of introducing tunneling back to the finite temperature Mott insulator can be considered perturbatively. The results of such a calculation [67] show that the leading order effect is to add to the free energy terms describing a Bose gas of

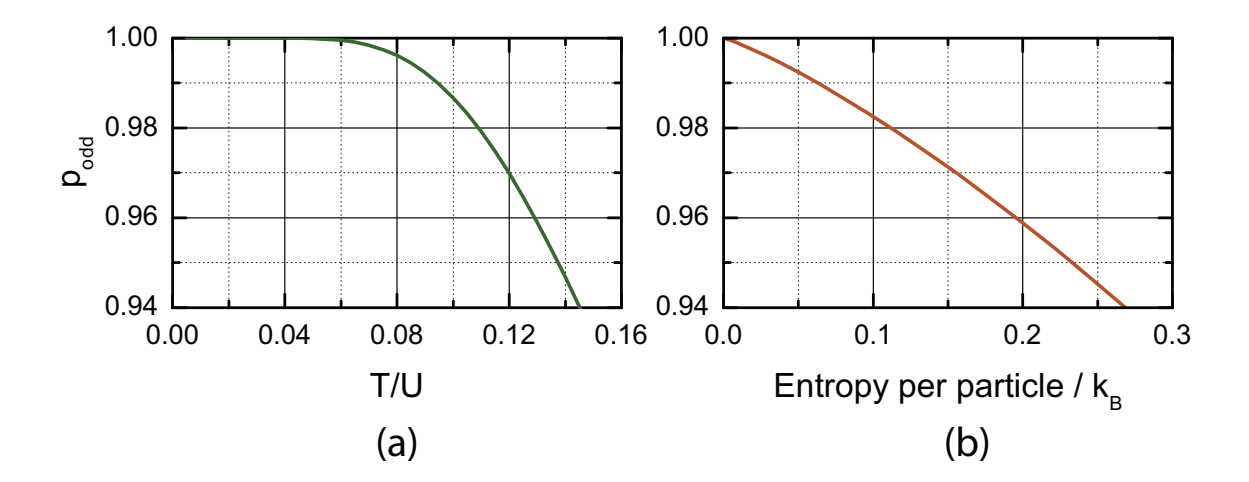


Figure 5.3: Mott insulators at finite temperature in the zero tunneling limit. The fidelity of the Mott insulator, quantified by  $p_{\text{odd}}$ , is shown vs. (a) the temperature T/U and (b) the entropy per particle.

quasiparticles and quasiholes that are mobile through the lattice. For two-dimensional lattices with a depth of about  $16E_r$  corresponding to the experimental regime we investigate, these effects are negligible.

#### 5.2 Microscopic study of the phase transition

We now proceed to describe the results of experiments in which we have used the quantum gas microscope to probe local phenomena in the superfluid to Mott insulator transition that have been described in the previous section. Our experiments start with a two-dimensional <sup>87</sup>Rb Bose-Einstein condensate of a few thousand atoms confined in a single well of a standing wave, with a harmonic oscillator length of 130nm. The condensate resides  $9\mu$ m from an in-vacuum lens that is part of an imaging system with a resolution of  $\sim 600$ nm. This high resolution system is used to project a square lattice potential onto the pancake cloud with a periodicity of

a=680nm. The lattice depth is increased linearly to  $0.4E_r$  in 50ms, and from there ramped exponentially to its final value ( $16E_r$  for most experiments) with a time constant of 81ms. In a homogeneous system in two dimensions, the transition to a Mott insulator with one atom per site occurs at a ratio of interaction energy to tunneling of U/J=16.7 [107, 179, 38], corresponding to a lattice depth of  $12.2E_r$ . During the ramp, the initial transverse confinement of 9.5Hz is increased such that the cloud size remains approximately constant, compensating for the increasing interatomic interaction and deconfinement due to the blue lattice. This allows for faster ramps while maintaining adiabaticity, because the density redistribution during the lattice ramp is minimized. After preparing the many-body state, we image the atoms by increasing the lattice depth several hundred-fold, and then illuminate the atoms with an optical molasses that serves to localize the atoms while fluorescence photons are collected by the high resolution optics.

#### 5.2.1 Single-site imaging of atom number fluctuations

As discussed previously, the presence of light-assisted collisions means that the imaged atom number is  $n \mod(2)$  where n is the projected atom number before the collisions. Figure 5.4 shows fluorescence images in a region of the cloud as the final depth of the lattice is increased. The initial superfluid density is chosen to obtain an insulator with two shells on the Mott side of the transition, and the region shown is in the outer shell containing one atom per site. For high filling fractions, the lattice sites in the images are barely resolved, but the known geometry of the lattice and imaging system point spread function obtained from images at sparser fillings allow

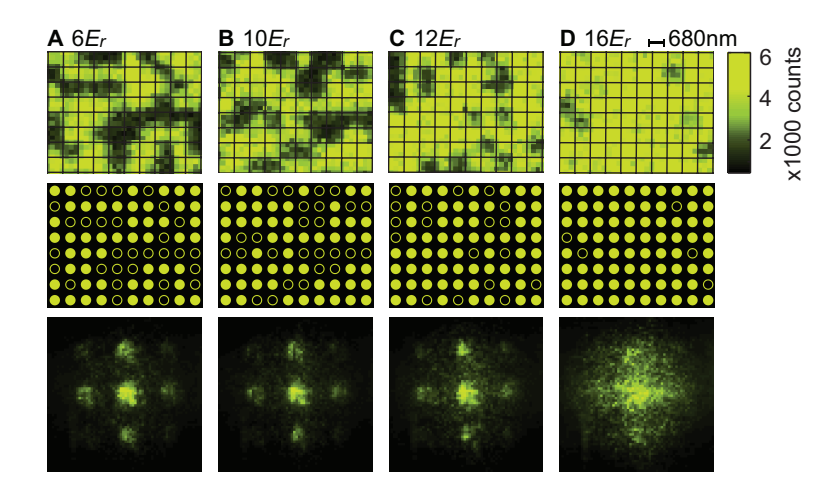


Figure 5.4: Single-site imaging of atom number fluctuations across the superfluid to Mott insulator transition. Images within each column are taken at the same final 2D lattice depth of  $6E_r$  (A),  $10E_r$  (B),  $12E_r$  (C), and  $16E_r$  (D). Top row: In-situ fluorescence images from a region of 10 by 8 lattice sites within the n=1 Mott shell that forms in a deep lattice. In the superfluid regime [(A) and (B)], sites can be occupied with odd or even atom numbers, which appear as full or empty sites, respectively, in the images. In the Mott insulator, occupancies other than 1 are highly suppressed (D). Middle row: results of the atom detection algorithm for images in the top row. Solid and open circles indicate the presence and absence, respectively, of an atom on a site. Bottom row: Time-of-flight fluorescence images after 8-ms expansion of the cloud in the 2D plane as a result of nonadiabatically turning off the lattice and the transverse confinement (averaged over five shots and binned over 5 by 5 lattice sites).

reliable extraction of site occupations.

We determine  $p_{\text{odd}}$  for each site using 24 images at each final lattice depth. The transverse confining potential varies slowly compared to the lattice spacing and the system is to good approximation locally homogeneous. We make use of this to improve the error in our determination of  $p_{\text{odd}}$ , by averaging over a group of lattice sites, in this case 51 (30) sites for regions in the first (second) shell (Fig. 5.5). In the n=1 shell, we detect an atom on a site with probability  $94.9 \pm 0.7\%$  at a lattice depth of  $16E_r$ . We measure the lifetime of the gas in the imaging lattice and determine that

 $1.75\pm0.02\%$  of the occupied sites are detected as unoccupied due to atoms lost during the imaging exposure time of 1s because of background gas collisions. We correct for this effect in the given average occupation numbers and errorbars.

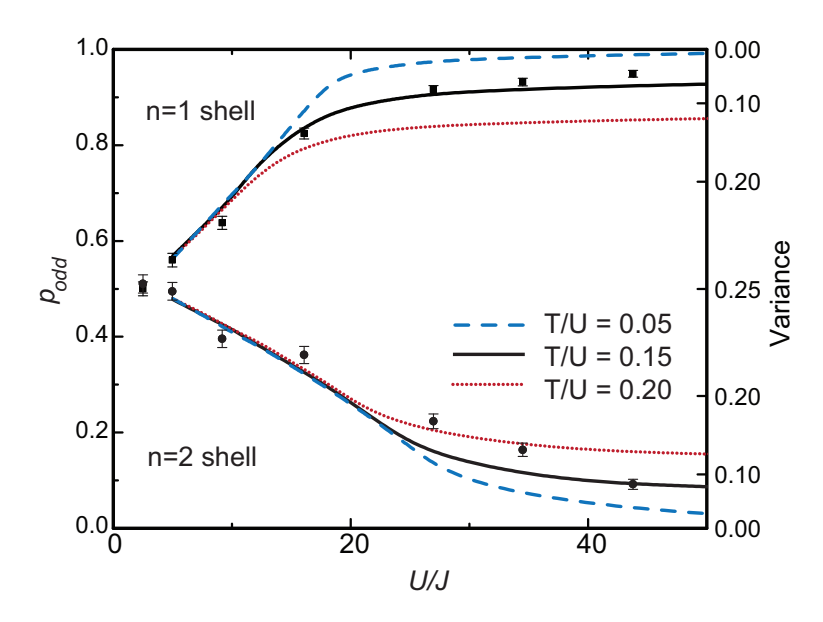


Figure 5.5: Measured value of  $p_{\text{odd}}$  versus the interaction to-tunneling ratio U/J. Data sets, with 1s error bars, are shown for regions that form part of the n=1 (squares) and n=2 (circles) Mott shells in a deep lattice. The lines are based on finite-temperature Monte Carlo simulations in a homogeneous system at constant temperature-to-interaction ratio (T/U) of 0.20 (dotted red line), 0.15 (solid black line), and 0.05 (dashed blue line). The axis on the right is the corresponding odd-even variance given by  $p_{\text{odd}}(1-p_{\text{odd}})$ .

#### 5.2.2 Thermometry down to zero temperature

Measuring the defect density in the Mott insulator provides sensitive local thermometry deep in the Mott regime. Thermometry in the Mott state has been a long-standing experimental challenge [189, 184] and has acquired particular significance as experiments approach the regime of quantum magnetism [49, 3, 183] where

the temperature scale should be on the order of the superexchange interaction energy. We directly image excitations of the n=1 Mott insulator, holes and doublons, as they both appear as missing atoms in the images. Similarly, for Mott insulators with higher fillings n, sites with excitations (n+1,n-1) can be detected through their opposite parity signal. For finite tunneling rate J much smaller than the interaction energy U, the admixture fraction of coherent hole-doublon pairs excitations is  $\sim (J/U)^2$ , whereas any other excitations are due to incoherent thermal fluctuations and are suppressed by a Boltzmann factor  $e^{-U/T}$ .

The theory curves presented in Figure 5.5 are the predicted  $p_{\text{odd}}$  in the two shells for different values of T/U. The curves are obtained using a quantum Monte-Carlo "worm" algorithm [151, 149], and the average temperature extracted using the data points at the three highest U/J ratios is  $T/U \sim 0.16\pm0.03$ . At the transition point for n=1, this corresponds to a temperature of 1.8nK. Assuming this value of T/U to be the overall temperature, the thin layer between the Mott shells should be superfluid, and the transition to a normal gas is expected around a critical temperature of zJ=2.8nK, where z is the number of nearest neighbours in the lattice [67].

#### 5.2.3 Measurement of local adiabaticity timescales

In a second series of experiments, we use on-site number statistics to probe the adiabaticity timescale for the transition, focusing on the local dynamics responsible for narrowing the number distribution. We start by increasing the lattice depth adiabatically to  $11E_r$ , still in the superfluid regime, using the same ramp described previously. Next the depth is ramped linearly to  $16E_r$  where, for an adiabatic ramp,

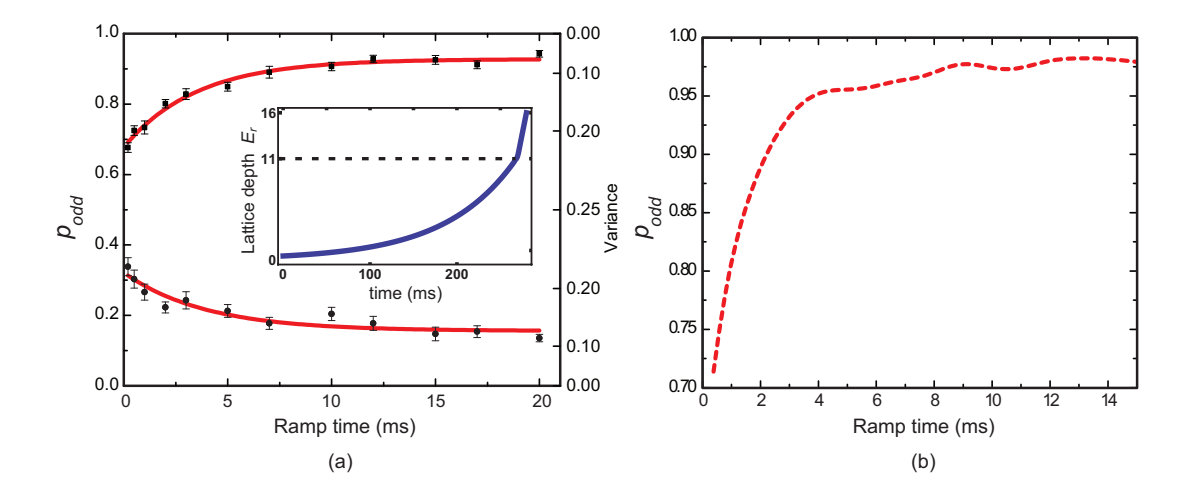


Figure 5.6: Dynamics of on-site number statistics for a fast ramp from the superfluid regime to the Mott regime. (a)  $p_{\text{odd}}$  at the end of the ramp versus ramp time is shown in the n=1 (squares) and n=2 (circles) shells, averaged over 19 data sets with 1s error bars. Red lines are exponential fits. Inset shows the two-part ramp used in this experiment. The first part is a fixed adiabatic exponential ramp (t=81 ms) and the second is a linear ramp starting at  $11E_r$  and ending at  $16E_r$ . The duration of the second ramp is varied in the experiment. (b) Theoretical prediction for the dynamics in the n=1 shell using the mean-field model we have developed, showing a similar characteristic timescale.

a Mott insulator should form. The ramp time is varied from 0.2ms to 20ms, and  $p_{\text{odd}}$  is measured in the first and second shells as before (Fig. 5.6(a)); we find that the data fits well to exponential curves that asymptote to the value of  $p_{\text{odd}}$  obtained in the adiabatic case. The fitted time constant in the first (second) shell is  $3.5 \pm 0.5$ ms  $(3.9 \pm 1.3$ ms).

Compared to the critical value of the tunneling time  $h/J_c = 68$ ms for the first shell, the observed dynamics are fast, but we can reproduce the observed timescale using the mean-field model developed in Sec. 5.1.3, as shown in Figure 5.6(b).

Although the local number statistics change on a fast timescale, entropy redis-

tribution in the inhomogeneous potential should occur on a much slower timescale. Because superfluid and normal domains have a larger specific heat capacity than Mott domains, in an inhomogeneous system, entropy is expelled from the Mott domains and accumulates in the transition regions after crossing the phase transition if the system is in thermal equilibrium [148]. It was found, however, that in bulk Mott regions the insulating behavior makes entropy transport difficult, and global thermalization is slow on experimental timescales [91]. In our system, optical potential corrugations produce sizable potential gradients in some regions, leading to a heterostructure of almost one-dimensional Mott domains, about 1-2 lattice sites thick, surrounded by transition layers (Fig. 5.7). We find remarkably low defect densities and sharp transitions between superfluid and Mott states in these regions. The measured defect probability per site in the domain shown is  $0.8 \pm 0.8\%$ . In these microscopic domains, each site of a Mott domain is in contact with a superfluid region. Such a configuration is likely to lead to fast thermalization, which would explain the low defect density we observe. This suggests that the lowest entropies in a Mott insulator might be obtained under conditions where the chemical potential is engineered so as to obtain alternating stripes (2D) or layers (3D) of insulating and superfluid regions [150, 38].

#### 5.2.4 Imaging the Mott insulator shell structure

While we have mostly focused on microscopy of Mott insulators, the ability to take high resolution images combined with the parity imaging allows us to obtain atomby-atom pictures of the concentric shell structure. Previously, the shell structure was imaged through tomographic [61], spectroscopic [35], and in-situ imaging techniques,

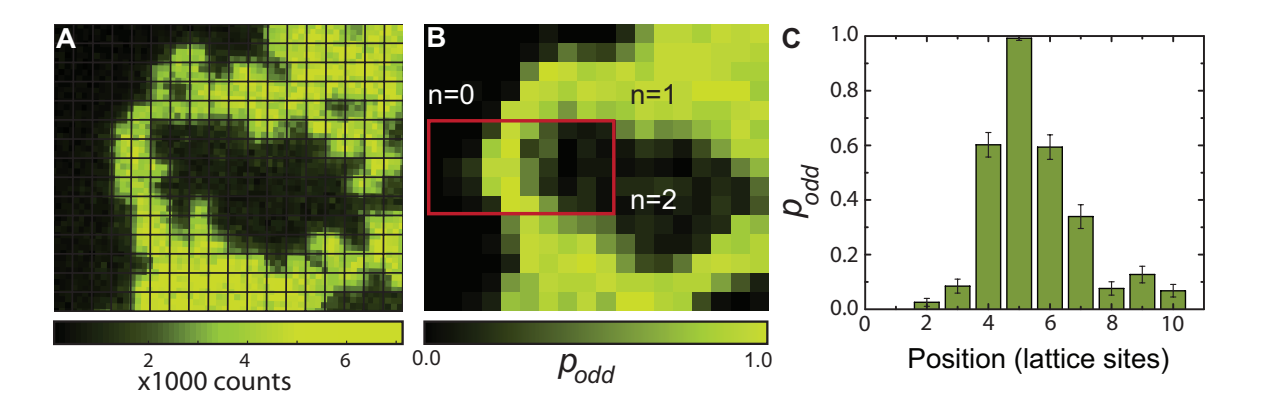


Figure 5.7: Low-entropy Mott domains observed in a steep potential gradient. (A) Single-shot in-situ image of a Mott insulator in a  $16E_r$  deep lattice with 25 Hz transverse confinement. The ring is an n=1 insulator enclosing an n=2 region. (B) Average  $p_{\rm odd}$  over 24 images. Each pixel corresponds to a single lattice site. The red rectangle encloses a region containing a Mott insulator with n=1, a few lattice sites wide. (C) Column average of  $p_{\rm odd}$  over the sites within the red rectangle in (B), with 1s error bars.

coarse-grained over several lattice sites [66]. In Figure 5.8A to D, the formation of the various shells, up to the fourth, is shown as the atom number in the trap is increased. Slowly varying optical potential disorder causes deviation from circular symmetry in the shells. The spatial pattern of the disorder is static in time and for a lattice depth of  $22E_r$ , has an RMS gradient of  $(0.13 \pm 0.01)U$  per lattice site and a characteristic length scale of 10 lattice sites. The contour lines of the potential are directly extracted from the shell structure boundaries in the Mott regime. Different contour lines are obtained by varying the atom number. In Fig. 5.8E and F, we have compensated this disorder by projecting a light pattern generated using a digital micromirror device through the objective (Sec. 4.7), resulting in a nearly circular shell structure. In later experiments, we have used further spatial filtering the lattice beams before the objective to eliminate long wavelength disorder, and the improved shell images are

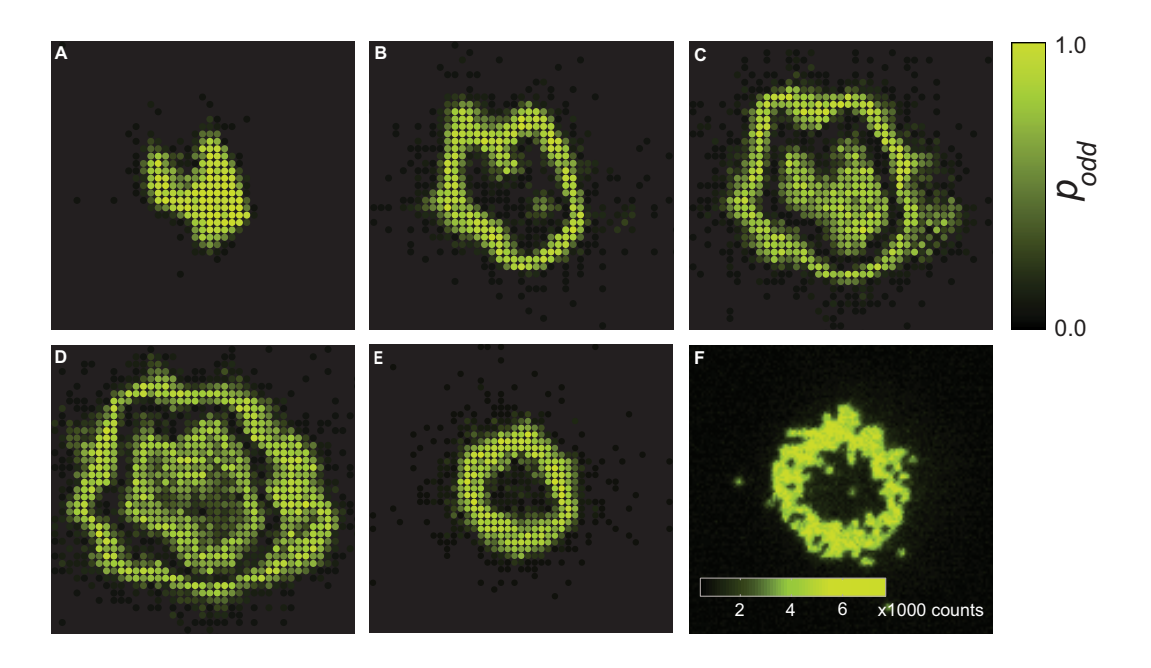


Figure 5.8: Single-site imaging of the shell structure in a Mott insulator. (A to D) The images show  $p_{\rm odd}$  on each site determined by averaging 20 analyzed fluorescence images. The lattice depth is  $22E_r$  and the transverse confinement is 45 Hz. As the atom number is increased, the number of shells in the insulator increases from one to four. The value of  $p_{\rm odd}$  for odd-numbered shells is close to 1; for even-numbered shells, it is close to 0. The atom numbers, determined by in-situ imaging of clouds expanded in the plane, are  $120\pm10$  (A),  $460\pm20$  (B),  $870\pm40$  (C), and  $1350\pm70$  (D). (E and F) Long-wavelength disorder can be corrected by projecting an appropriate compensation light pattern onto the atoms, resulting in nearly circular shells. (E)  $p_{\rm odd}$  (average of 20 analyzed images); (F) a single-shot raw image (arbitrary units).

shown in Figure 5.9.

#### 5.2.5 Density correlations in the Mott insulator

At finite tunneling, a Mott state with one atom per site has tunneling induced quantum fluctuations where an atom hops virtually to a neighbouring site and back. This fluctuation is admixed at order J/U for each pair of neighbouring sites and if

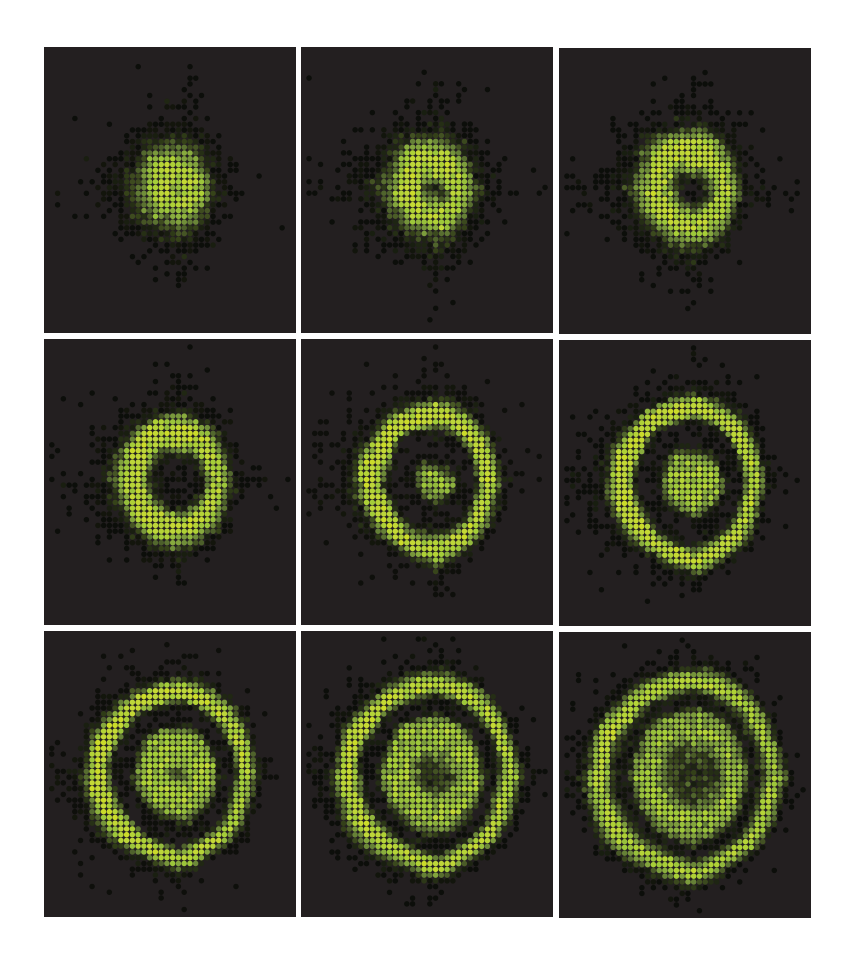


Figure 5.9: Averaged images of the shell structure for increasing atom number. In these images, further spatial filtering of the lattice beams before the high resolution objective reduced long-wavelength disorder.

we image the insulator, we should be able to observe the fluctuation with probability  $\sim (J/U)^2$  for any pair.

We observe the fluctuation as a pair of neighbouring dark sites. Of course, thermal fluctuations also produce defects, but the locations of the defects are uncorrelated. Therefore if the defect probability is d, we can investigate whether we observe neighbouring defects with a probability that is higher that what we would expect for statistically independent thermal defects  $(d^2)$ . This excess is due to quantum

fluctuations.

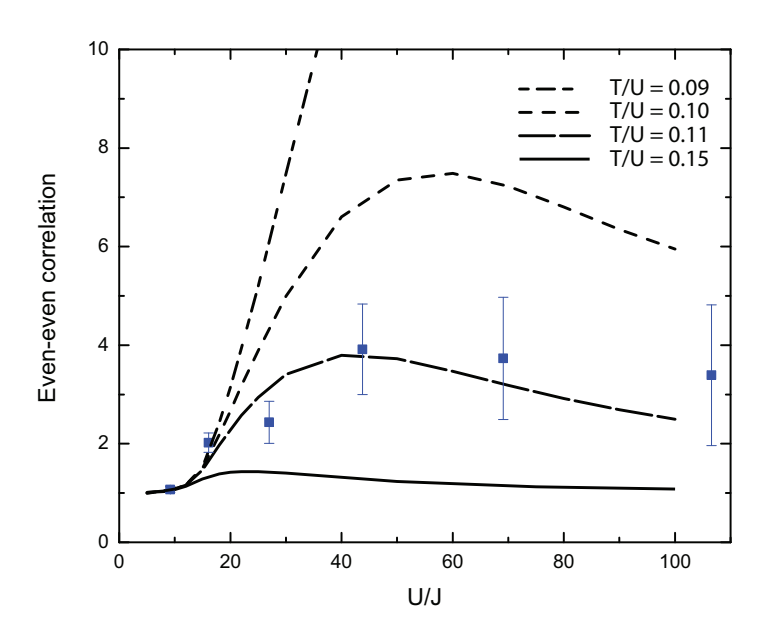


Figure 5.10: Nearest neighbour density correlations in the Mott insulator. The data points indicate how much more likely it is to observe neighbouring pairs with even occupation beyond what is expected if the even occupations appeared in a statistically independent manner. The enhancement in the Mott regime is due to doublon-hole virtual excitations. The theoretical curves are based on quantum Monte-Carlo simulations at different temperatures T/U between 0.09 and 0.15.

We define a correlation function  $g_2$  that captures this concept:  $g_2 = p_{ee}/p_e^2$ , where  $p_{ee}$  is the probability of observing neighbouring defects on any pair and  $p_e$  is the probability of a defect on a site.  $g_2$  is expected to be unity in the superfluid limit (shallow lattice) since a scalar field cannot have density-density correlations and is also unity for an insulator in a very deep lattice because quantum fluctuations vanish in the zero-tunneling limit, leaving only the frozen thermal defects. In between those two limits,  $g_2$  should exceed unity, with a maximum value that depends sensitively on the temperature of the cloud.

Figure 5.10 shows  $g_2$  obtained from the center of an n=1 Mott shell, with quantum Monte-Carlo theory for various temperatures. The data agrees with T/U=0.11. The error bars for data taken at high depths are large because very few events with neighbouring dark sites are recorded.

## Chapter 6

# Magnetic quantum phase transition in a spin chain

Publications based on the work described in this chapter:

"Quantum Simulation of an Antiferromagnetic Spin Chain in an Optical Lattice", J. Simon, W. Bakr, R. Ma, M. Tai, P. Preiss and M. Greiner, Nature **472**, 307-312 (2011)

Understanding exotic forms of magnetism in quantum mechanical systems is a central goal of modern condensed matter physics. A quantum magnet is made of interacting quantum mechanical spins that can be in a superposition of classical many-body states, leading to a Hilbert space of possible states that is exponentially large in the system size [161]. In this chapter, we describe experiments that use our ultracold atom system to simulate a quantum Ising spin chain in the presence of both longitudinal and transverse magnetic fields in the neighbourhood of a multicritical point. We demonstrate a reversible transition between a paramagnetic phase and an

antiferromagnetic phase and use in-situ site-resolved imaging and noise correlation measurements to study domain formation.

Quantum magnetic transitions have been previously explored in other cold atom systems. The Stoner model of itinerant ferromagnetism has been studied in a degenerate Fermi gas [99] and highly connected quantum spin networks have been investigated with short ion chains [103]. Polar molecules [133] and Rydberg atoms [87] have been the subject of preliminary investigations both experimentally and theoretically [187, 33, 123] as alternatives to ground-state atoms with stronger, longer-range interactions. Magnetically ordered states have been artificially prepared through patterned loading [58, 116, 188, 175] and in double-well [59] experiments.

Traditionally, the spins in an optical lattice have been encoded in a ground state hyperfine degree of freedom of the atoms [49]. Direct interactions between atoms on neighbouring lattice sites due to the overlap of Wannier functions are extremely weak (sub-Hertz level). A somewhat stronger interaction (several Hertz level) is achievable through superexchange, which involves virtual tunneling of an atom to a neighbouring site where the interaction occurs before it tunnels back. The timescale for such a process is  $t^2/U$ , where t is the tunneling rate and U is the interaction. Such interactions have been observed in double well systems [183], but many-body ordering through superexchange interactions has not been achieved to date. We follow a different route to achieve stronger interactions. We simulate a 1D chain of interacting Ising spins by mapping doublon-hole excitations of a Mott insulator [78, 97, 56] of spinless bosons in a tilted 1D optical lattice [163] onto a pseudo-spin degree of freedom. This approach has a dynamical timescale set by the tunneling rate t, which is about

ten times larger than superexchange interactions in our system.

# 6.1 Simulating an antiferromagnetic Ising chain in an optical lattice

In the experiments of Greiner  $et\ al.$  [78], a gradient was applied to a Mott insulator in a lattice to study its insulating properties. A resonant response was found near the interaction energy U. Sachdev  $et\ al.$  analyzed the experiments [163] using a one-dimensional model, ignoring the presence of any harmonic trapping potentials. They showed that under the influence of such field gradients, the dynamics of a 1D Mott insulator map onto a quantum Ising Hamiltonian with transverse and longitudinal fields, in the neighbourhood of a multicritical point. We describe this model by first explaining the underlying Bose-Hubbard dynamics, and then turning to the mapping onto the effective spin model.

We will work deep in the Mott insulator regime  $(U \gg t)$  where it is energetically forbidden for the atoms to tunnel as long as the tilt per lattice site, E, differs from the onsite atom-atom interaction U. Hence, the system remains in a state with one atom per lattice site for E < U (Fig. 6.1(a)). As the tilt approaches the interaction strength (E = U), each atom is free to tunnel onto its neighbour, so long as its neighbour has not itself tunneled (Fig. 6.1(b)). This nearest-neighbour constraint is the source of the effective spin-spin interaction. If the tilt E is increased sufficiently slowly through the transition so as to keep the system near its many-body ground state, density wave ordering results (Fig 6.1(c)).

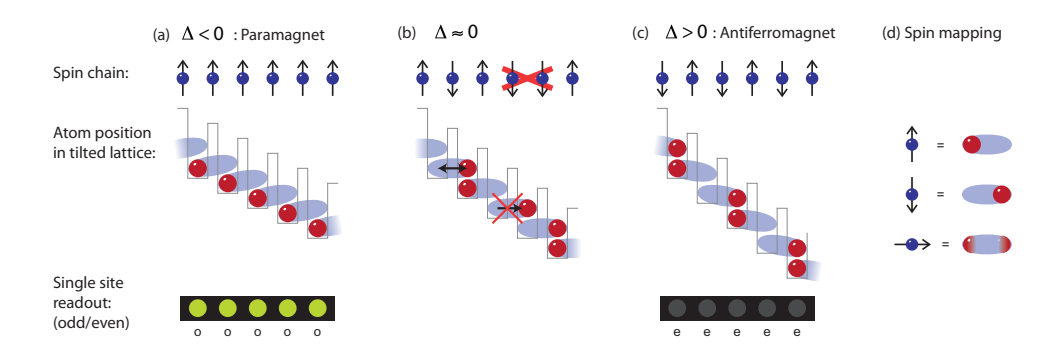


Figure 6.1: Tilted Hubbard model and mapping to spin model. (a) Middle row: When a Mott insulator is placed in a tilted lattice, it remains in a state with one atom per lattice site until the tilt per site E reaches the onsite interaction energy U. (b) At this point the energy cost  $\Delta = E - U$  to move to the neighbouring site vanishes, and the atoms begin to tunnel resonantly to reduce their energy. An atom, however, can only tunnel to a neighbouring site if the atom on that site has not itself tunneled away. If no atom is present on the neighbouring site, the tunneling process is suppressed by the energy gap U. This creates a strong constraint and leads to the formation of entangled states. (c) As the tilt is increased further, the system transitions into a doubly degenerate staggered phase. (d) This system may be mapped onto a model of interacting spin-1/2 particles, where the two spin states correspond to the two possible positions of each atom. In the spin model, the aforementioned constraint forbids adjacent down spins, realizing a spin-spin interaction. The initial Mott insulator now corresponds to a PM phase with all spins aligned upwards to a large magnetic field (see top row), the state at resonant tilt corresponds to a non-trivial (critical) spin configuration, and staggered ordering at even larger tilt corresponds to an AF phase. Bottom row: The phases can be detected by single lattice site imaging. Because the imaging system is sensitive only to the parity of the atom number, PM domains appear bright (a), and AF domains appear dark (c).

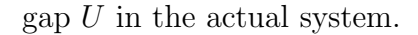
Sachdev et al. describe the tilted-lattice physics in an effective model with dipolar (doublon-hole) excitations, but point out that it also maps to a spin model since each atom has only two possible positions. Figure 6.1(d) shows the spin configurations that correspond to the various atom distributions in the optical lattice. We can define a spin on each link between neighbouring lattice sites, with the spin pointing up if the atom on the left remains there, and pointing down if that atom moves

one site down the gradient. The spin can of course exist in superpositions of the two states. For example, a spin in an equal superposition of being on the left and right sites would correspond to a spin in the x - y plane of a Bloch sphere. The transition from a uniform phase at small tilt to a density wave phase at large tilt corresponds to a transition from a paramagnetic phase with all spins pointing up to an antiferromagnetic phase where spins alternate between pointing up and down.

In the next section, we will formally show that the effective spin Hamiltonian equivalent to the dipole model is that of an antiferromagnetic Ising chain with longitudinal and transverse magnetic fields:

$$H = J \sum_{i} \left( S_z^i S_z^{i+1} - (h_z + \delta_z^i) S_z^i - h_x S_x^i \right)$$
 (6.1)

Here  $S_z^i$  and  $S_x^i$  are spin- $\frac{1}{2}$  operators of the ith spin, and  $S_z^i S_z^{i+1}$  denotes the nearest-neighbour antiferromagnetic spin interaction of strength J. A spin flip is driven by the transverse magnetic field, corresponding to the dimensionless tunneling  $\tilde{t} = t/J$  between sites of the Mott state according to  $h_x = 2^{3/2}\tilde{t}$ . The longitudinal field  $h_z = 1 - \tilde{\Delta}$  orients the spins in the effective model. It is composed of a bias of strength one and the dimensionless tilt offset  $\tilde{\Delta} = \Delta/J$ , where  $\Delta = E - U$  is the difference between the tilt per lattice site, and the interaction U. Additionally,  $\delta_z^i = \delta E_i/J$  is a local z-field inhomogeneity, equivalent to a local tilt inhomogeneity  $\delta E_i$ . Figure 6.2(b) illustrates how the combination of spin interaction and longitudinal magnetic bias field realizes the nearest-neighbour constraint of the tilted Mott insulator, preventing two adjacent spins from both being anti-aligned to the longitudinal field. The energy cost of such an excitation would be the spin interaction J, which is on order of the energy



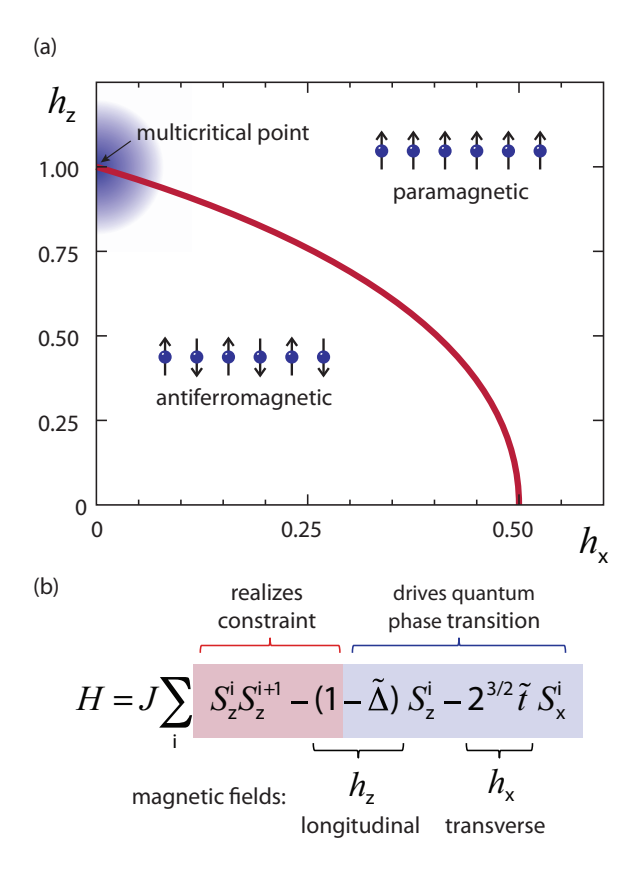


Figure 6.2: Spin model and its phase diagram. (a) An antiferromagnetic 1D Ising chain in longitudinal  $(h_z)$  and transverse  $(h_x)$  magnetic fields exhibits two phases at zero temperature (PM and AFM). These phases are separated by a second order phase transition (red line), except at the multicritical point  $(h_z; h_x) = (1; 0)$ , where the transition is classical and first order. The region that can be accessed in our experiment, in the vicinity of  $(h_z; h_x) = (1; 0)$ , is highlighted in blue. (b) In this neighbourhood the Hamiltonian may be decomposed into a constraint term that prevents adjacent spin-flips (red highlight), and fields that drive the phase transition (blue highlight).

#### 6.1.1 Mapping onto the spin model

We follow Sachdev *et al.* in formally mapping a 1D Mott insulator of spinless bosons in a tilted lattice onto a chain of interacting dipoles, and then onto a chain of

spin-1/2 particles with AF Ising interactions in longitudinal and transverse fields. In a homogeneously tilted lattice, the 1D Bose-Hubbard Hamiltonian reads:

$$H = -t\sum_{j} \left( a_{j}^{\dagger} a_{j+1} + a_{j} a_{j+1}^{\dagger} \right) + \frac{U}{2} \sum_{j} n_{j} \left( n_{j} - 1 \right) - E \sum_{j} j \cdot n_{j}$$
 (6.2)

Here t is the nearest-neighbour tunneling rate, U is the onsite interaction, E is the tilt per lattice site,  $a_j^{\dagger}$  ( $a_j$ ) is the creation (annihilation) operator for a particle on site j, and  $n_j = a_j^{\dagger} a_j$  is the occupation number operator on site j. We will work in a regime where  $t, |E - U| \ll U, E$ . For a tilt near U = E, the onsite interaction energy cost for an atom to tunnel onto its neighbour is almost precisely cancelled by the tilt energy. If one starts in a Mott insulator with M atoms per site, an atom can then resonantly tunnel onto the neighbouring site to produce a dipole excitation with a pair of sites with M+1 and M-1 atoms. The resonance condition is only met if adjacent sites contain equal numbers of atoms, so only one dipole can be created per link and neighbouring links cannot both support dipoles. We define a dipole creation operator  $d_j^{\dagger} = \frac{a_j a_{j+1}^{\dagger}}{\sqrt{M(M+1)}}$ . The Bose-Hubbard Hamiltonian above can hence be mapped onto the dipole Hamiltonian

$$H = -\sqrt{M(M+1)t} \sum_{j} \left( d_j^{\dagger} + d_j \right) + (U - E) \sum_{j} d_j^{\dagger} d_j$$
 (6.3)

subject to the constraints  $d_j^{\dagger}d_j \leq 1$ ,  $d_{j+1}^{\dagger}d_{j+1}d_j^{\dagger}d_j = 0$ . The factor of  $\sqrt{M(M+1)}$  arises due to bosonic enhancement. It is important to note here that there are only two parameters in the Hamiltonian at this point, E-U and t, since U has dropped out of the problem when we restricted our attention to the resonant subspace. Therefore,

the critical point of the quantum phase transition in this Hamiltonian can only depend on the ratio of these two parameters.

To map from the dipole Hamiltonian to the spin-1/2 Hamiltonian, we define a link without (with) a dipole excitation to be an up (down) spin along  $\hat{z}$ . Then the creation/annihilation of dipoles are related to the flipping of spins, and we can write:  $S_z^j = \frac{1}{2} - d_j^{\dagger} d_j$ ,  $S_x^j = \frac{1}{2} \left( d_j^{\dagger} + d_j \right)$ , and  $S_y^j = \frac{i}{2} \left( d_j^{\dagger} - d_j \right)$ . The constraint forbidding adjacent dipoles can be implemented by introducing a positive energy term  $J d_{j+1}^{\dagger} d_{j+1} d_j^{\dagger} d_j = J \left( S_{j+1}^z - \frac{1}{2} \right) \left( S_j^z - \frac{1}{2} \right)$  to the Hamiltonian, where J is of order U. This term gives rise to nearest-neighbour interactions and an effective longitudinal field for the spins.

Defining  $\Delta = E - U$  the Hamiltonian for the spins now reads:

$$H = J \sum_{j} S_{z}^{j} S_{z}^{j+1} - 2\sqrt{M(M+1)}t \sum_{j} S_{x}^{j} - (J-\Delta) \sum_{j} S_{z}^{j}$$
 (6.4)

$$= J \sum_{j} \left( S_{z}^{j} S_{z}^{j+1} - h_{x} S_{x}^{j} - h_{z} S_{z}^{j} \right)$$
 (6.5)

The dimensionless fields are defined as  $h_x = 2^{3/2}t/J = 2^{3/2}\tilde{t}$ ,  $h_z = 1 - \frac{\Delta}{J}$ , with M set to one as in our experiment.

#### 6.1.2 The paramagnetic and antiferromagnetic phases

The Hamiltonian described in the previous section exhibits a quantum phase transition between a paramagnetic and antiferromagnetic state as the parameter  $g = (h_z - 1)/h_x$  is varied across a critical value. Our approach towards understanding this quantum phase transition will start from the two classical ground states on

either side of transition when g is far from its critical value. We will then proceed to understand the effect of quantum fluctuations as we move away from these limiting cases, but remain far from the critical point.

We start with the classical case  $h_x = 0$ , where there are no tunneling-induced quantum fluctuations. There are two competing terms in the Hamiltonian:  $S_z^j S_z^{j+1}$  prefers antiferromagnetic ordering while  $-h_z S_z^j$  prefers alignment with the field. For g > 0, the field-induced ordering overcomes the antiferromagnetic spin-spin interaction and the ground state is a paramagnet with all the spins pointing up along  $h_z$ . For g < 0, the antiferromagnetic term dominates, producing staggered ordering. At precisely g = 0, the Zeeman energy cost of anti-aligning a spin with the field is exactly compensated for by the reduction in energy from the antiferromagnetic spin-spin interaction.

In the antiferromagnetic state, there exists an interesting interplay between the degeneracy of the ground state, the boundary conditions and the length of the chain. For an infinitely long chain, it is clear that there are two possible states, one where the up spins are on the odd sites and the other where they are on the even sites. In the absence of symmetry breaking, the ground state is a symmetric superposition of those two states

$$|\Psi\rangle = |\uparrow\downarrow\uparrow\downarrow\uparrow\downarrow\uparrow\downarrow\uparrow\downarrow\uparrow\downarrow\downarrow...\rangle + |\downarrow\uparrow\downarrow\uparrow\downarrow\uparrow\downarrow\uparrow\downarrow\uparrow\downarrow\uparrow...\rangle \tag{6.6}$$

For exact diagonalization studies, we will often use periodic boundary conditions. Under these conditions, the ground state depends on whether the chain length is even or odd. With an even chain length, the situation is similar to the infinite chain described above with two degenerate ground states. However, for an odd chain, the system is frustrated and a defect has be introduced. This defect can be on any site in the chain, and therefore, for a chain of length N, the ground state is superposition of N states with different positions of the defect. For example, with five sites, the ground state with periodic boundary conditions is

$$|\Psi\rangle = |\uparrow\downarrow\uparrow\downarrow\uparrow\rangle + |\uparrow\uparrow\downarrow\uparrow\downarrow\rangle + |\downarrow\uparrow\uparrow\downarrow\uparrow\rangle + |\uparrow\downarrow\uparrow\uparrow\downarrow\rangle + |\downarrow\uparrow\downarrow\uparrow\uparrow\rangle \tag{6.7}$$

Open boundary conditions, which are more relevant for the experiment, can also produce interesting frustrated states. The boundary conditions of chains in the experiment can be set by thermal defects, superfluid atoms at shell boundaries or disorder in the lattice potential.

#### 6.1.3 Second order hopping processes

In this section, we reintroduce the tunneling (finite  $h_x$ ) but work in the weak tunneling regime ( $|g| \to \infty$ ). This will allow us to obtain the ground and excited states using perturbation theory about the  $h_x = 0$  states. The constraint that there are no neighbouring dipoles translates to never having two neighbouring down spins in a chain. On the other hand, neighbouring up spins are within the resonant subspace. This breaking of up-down symmetry by the  $h_z$  field will lead to the emergence of an effective local spin hopping mechanism in the excited states. This mechanism leads to the delocalization of "spin defects".

The finite-tunneling perturbed ground states contain an admixture of states with a single defect, a down spin on the paramagnetic side or a domain wall on the antiferromagnetic side. Denoting the state with a defect on the ith site as  $|i\rangle$ , the ground state is

$$|\Psi\rangle = |\Psi\rangle_{h_x=0} - \frac{(h_z - 1)}{4g^2} \sum_{i} |i\rangle. \tag{6.8}$$

Next we consider the first excited states on the paramagnetic side of the transition. These have one anti-aligned with the field, for example  $|\uparrow\uparrow\uparrow\downarrow\uparrow\uparrow\uparrow\uparrow...\rangle$ . Relative to the ground states with all spins field-aligned, this state has an energy  $h_z - 1$  (where all energies are in units of J). The following second-order process can occur because the initial and final states have the same energy

$$|\uparrow\uparrow\uparrow\downarrow\uparrow\uparrow\uparrow\uparrow...\rangle \longrightarrow |\uparrow\uparrow\uparrow\uparrow\uparrow\uparrow\uparrow\uparrow...\rangle \longrightarrow |\uparrow\uparrow\uparrow\uparrow\downarrow\uparrow\uparrow...\rangle \tag{6.9}$$

Therefore, the defect can locally hop to a neighbouring site with an effective matrix element  $h_x^2/4(h_z-1)$ . Note that a similar process

$$|\uparrow\uparrow\uparrow\downarrow\uparrow\uparrow\uparrow...\rangle \longrightarrow |\uparrow\uparrow\uparrow\downarrow\downarrow\uparrow\uparrow...\rangle \longrightarrow |\uparrow\uparrow\uparrow\uparrow\downarrow\uparrow\uparrow...\rangle \tag{6.10}$$

is disallowed because the intermediate state is outside the resonant subspace. We can write down an effective Hamiltonian within the subspace of excited states with exactly one spin flipped. The effective Hamiltonian [163] is

$$H_{eff}/J = (h_z - 1) \sum_{i} \left[ |i\rangle\langle i| + \frac{1}{4g^2} (|i\rangle\langle i| + |i\rangle\langle i + 1| + |i + 1\rangle\langle i|) \right]$$
 (6.11)

Diagonalization of this effective Hamiltonian gives rise to a band of states having a single delocalized defect with an energy width on order of the effective hopping matrix element and the states can be labelled with the momentum of the defect, in a manner analogous to the Bloch bands of an atom in a lattice. The lowest energy state has momentum  $\pi$ , anticipating the formation on antiferromagnetic order.

On the antiferromagnetic side of the transition, the ground state has a staggered spin order and the first excited state has one flipped spin, leading to a domain wall, for example  $|\uparrow\downarrow\uparrow\uparrow\uparrow\downarrow\uparrow\downarrow...\rangle$ . Again, an effective local hopping term allows the domain wall to split into two walls that move around and delocalize through a second order process similar to the one described above

$$|\uparrow\downarrow\uparrow\uparrow\uparrow\downarrow\uparrow\downarrow...\rangle \longrightarrow |\uparrow\downarrow\uparrow\uparrow\uparrow\uparrow\uparrow\downarrow...\rangle \longrightarrow |\uparrow\downarrow\uparrow\uparrow\downarrow\uparrow\uparrow\downarrow...\rangle \tag{6.12}$$

#### 6.1.4 Quantum phase transition and the phase diagram

While perturbation theory allows us to study the state of the system near the classical limits, it breaks down as we approach the critical regime. A good variational wavefunction that can capture most of the physics in the critical regime is simply a sum of all the states in the resonant subspace, i.e. all states with no neighbouring down spins [137]. For a system with an even number of spins N and periodic boundary conditions, the number of such states can be shown to be the nearest integer to  $\phi^N$  where  $\phi$  is the golden ratio  $\phi = (1 + \sqrt{5})/2$ , i.e. the critical state is a superposition of an exponentially large number of states in the system size.

Exact diagonalization studies [163] show that the transition is in the Ising universality class. For example, the energy gap  $\Delta$  at the critical g scales as  $\Delta \sim 1/N$ . This indicates that a quantum simulation that is to remain in the ground state takes

a time that scales linearly with the system size, as opposed to a classical simulation which would scale exponentially.

The phase diagram of the spin model in a homogeneous field [137, 135] ( $\delta_z^i = 0$ ) is shown in Figure 6.2(b). The mapping of the Hubbard model to the spin model is only valid  $U, J \gg t, \Delta$ , corresponding to the vicinity of the multicritical point at  $(h_z, hx) = (1,0)$ . The mapping breaks down away from that point because states with three atoms on a lattice site are not within the Hilbert space which maps to the spin model. Nevertheless, the region around the multicritical point is interesting for two reasons. First, it is a critical point, and therefore it opens the door to studying interesting critical phenomena. Second, the presence of a large longitudinal field prevents using the fermionization approach [161], which can be used to obtain an exact energy spectrum for the transverse Ising model with no longitudinal field. Since the model is non-integrable, it can be used to address interesting questions regarding the thermalization of 1D systems starting from different initial non-thermal states [12].

In the regime where the model mapping is valid, the phase diagram consists simply of a line separating the PM and AFM phases that is tangent to the curve at the multicritical point. Assuming a parent Mott insulator with n = 1, the equation of this line is  $h_z = 1 - 0.66h_x$ .

#### 6.1.5 Extracting spin observables

Our work will focus on two spin observables. The first is the expectation value of spin along the longitudinal field given by

$$\overline{\langle S_z \rangle} = \frac{1}{N} \sum_i \langle S_z^i \rangle \tag{6.13}$$

This is a quantity that can be easily extracted from local measurements. Since our microscope is sensitive only to the parity of the site occupation number, PM domains (with one atom per lattice site) should appear as entirely bright regions, and AF domains (with alternating 0-2-0-2 occupation) as entirely dark regions. By averaging the occupation of a site over multiple images, we obtain the probability of an odd occupation on the jth lattice site  $(p_{\text{odd}}^j)$ , which corresponds to the probability of having a single atom on a site within the subspace of our model. This is related to the spin observables in the effective model by  $\langle S_z^{j-1}S_z^j\rangle=\frac{1}{2}\left(p_{\text{odd}}^j-\frac{1}{2}\right)$ . We average over all the atoms in the chain to obtain  $p_{\text{odd}}=\overline{p_{\text{odd}}^j}$ , which in combination with the constraint that neighbouring down spins are not allowed permits us to relate the chain averaged mean z-projection of spin to  $p_{\text{odd}}$  according to:  $\overline{\langle S_z^j\rangle}=\frac{p_{\text{odd}}}{2}$ . This quantity varies smoothly across the transition and depends only weakly on the chain length as seen in Figure 6.3.

On the other hand, there is a second observable which depends on the chain length (Fig. 6.3) and is supposed to be non-analytic across the transition for a thermody-

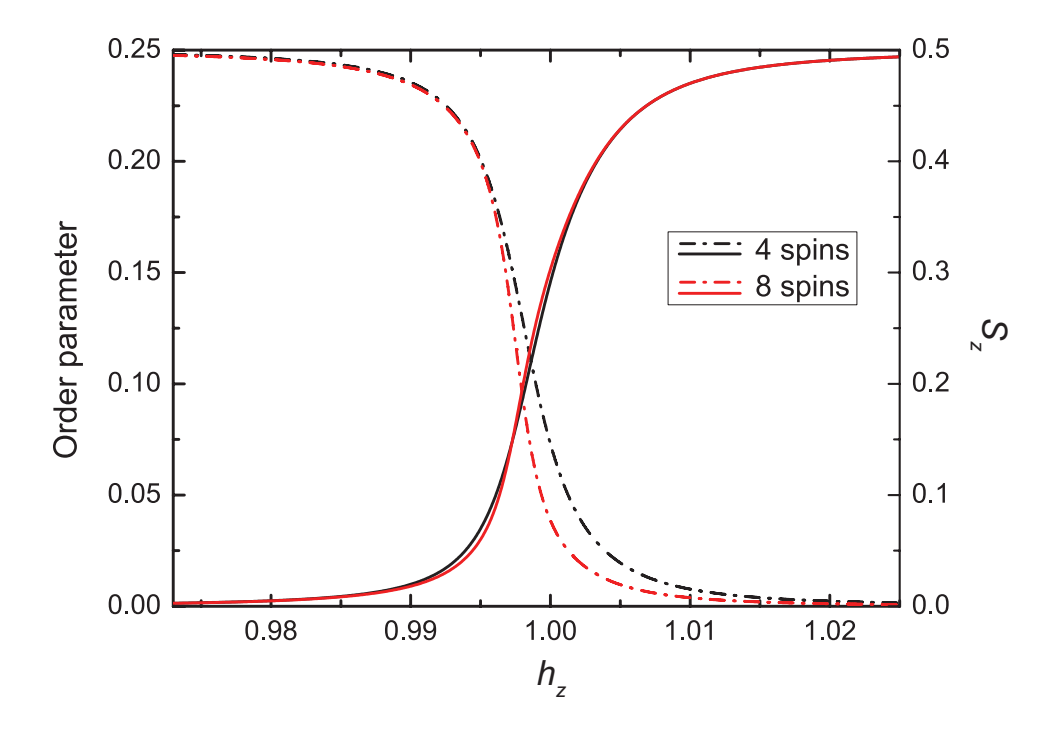


Figure 6.3: Comparing  $S_z$  to the order parameter. An exact diagonalization calculation (for  $h_x = 0.004$ ) of the ground state of a 1D chain of four (black) and eight (red) Ising spins with nearest-neighbour interactions, revealing that  $S_z$  (solid) is not sensitive to atom number, while the order parameter (dash-dotted) is. It is anticipated that the order parameter will exhibit a cusp in the large-system limit, though the exponential scaling with atom number precludes simulating substantially larger systems on a classical computer.

namic system, namely the order parameter for the transition [163] given by

$$O = \left\langle \left(\frac{1}{2} \sum_{j} (-1)^{j} S_{z}^{j}\right)^{2} \right\rangle \tag{6.14}$$

This quantity cannot be extracted directly from our in-situ measurements since it would require us to differentiate between sites containing no atoms and those containing two atoms. In principle such a measurement can be done in our system by loading a single chain and performing an expansion along the direction perpendicular

to the chain in a conservative lattice before turning on the pinning lattice. This would greatly reduce the chances of light assisted collisions between two atoms that were initially on the same site. Another approach that directly yields the order parameter, which we use in our experiments, is to use 1D quantum noise interferometry [2]. The information obtained from the noise correlation signal is identical to what can be obtained using Bragg diffraction of light off the antiferromagnetic crystal [43], analogous to neutron scattering or magnetic x-ray scattering in solids.

The amplitude of the noise correlation signal at separation d for a chain consisting of a large number of atoms is

$$C(d) = 1 + \frac{1}{N^2} \left| \sum_{j} e^{-i\frac{madj}{\hbar t}} n_j \right|^2$$

where N is the number of lattice sites, j is the lattice site index, a is the lattice spacing, m is the mass of the atom, t is the expansion time,  $n_j$  is the occupation of the jth site. It can be shown that the correlation signal at is related to the order parameter  $O = C\left(\frac{\pi\hbar t}{ma}\right) - 1$ .

The finite chain length in the chains reduces the baseline of the correlation signal from 1 by an amount on order of 1/N. In an ideal system, the width of the antiferromagnetic noise-correlation peaks can be used to infer the domain size. However, in the experiment the finite expansion time and corrugations of the potential in which the atoms expand broaden the correlation peaks.

#### 6.1.6 Exact diagonalization studies of small chains

For small chains containing less than fifteen spins, we can numerically solve the Schroedinger equation to obtain energy spectra and eigenstates of the system as well as its time evolution. Figure 6.4(a) shows a system of seven spins with open boundary conditions in the presence of additional harmonic confinement that can be present in our system. The harmonic confinement corresponds to a longitudinal magnetic field that varies linearly in space, i.e.  $\delta_z^i = Ki$ , with K = 0.01 in this case. The resulting energy spectrum exhibits a series of level crossings corresponding to flipping one spin at a time while forming the AFM. The gaps between the ground and first excited state are no longer many-body gaps which scale inversely with the system size, but rather two-body gaps on order of t. Therefore, for preparation of an AFM state, adiabaticity should be much easier to satisfy in the presence of harmonic confinement. Figure 6.4(b) shows the energy spectrum of a system of six spins with no harmonic confinement plotted vs.  $h_z$ . In this case, we have used periodic boundary conditions, and there are two degenerate states on the antiferromagnetic side of the transition.

Next we show the results of time-dependent studies. Figure 6.5(a) shows the time evolution of  $\langle S_z \rangle$  and the Neel order parameter while linearly sweeping  $h_z$  across the transition starting at 1.25 and ending at 0.85 over a time 100/J, starting with a Mott state (all spins up), as done in the experiment. The oscillations observed are due to the imperfect overlap of the initial state with the ground state of the system. Figure 6.5 shows the mean length-weighted domain length for different sweep rates across the transition.

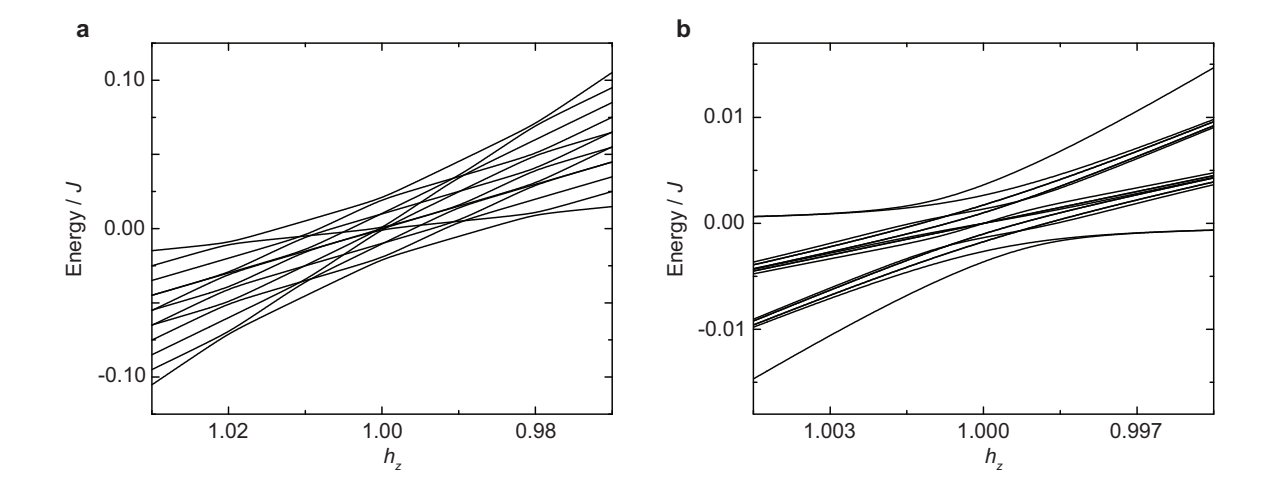


Figure 6.4: Exact diagonalization energy spectra of the magnetic Hamiltonian for small systems. (a) Energy spectrum of a 1D Ising chain in a longitudinal field gradient of 0.01 per lattice site, reflecting seven spins and open boundary conditions. As the longitudinal field is tuned across the critical point, each avoided crossing of the lowest energy state corresponds to a single spin-flip with energy gap  $h_x = 0.001$ . (b) Energy spectrum for a homogeneous 1D Ising chain of six spins, with periodic boundary conditions. In contrast to a., the single avoided crossing drives all spin-flips simultaneously, with a gap that decreases with increasing system size, as expected for the critical slowdown near a quantum phase transition.

## 6.1.7 Beyond the Ising Hamiltonian

The Ising Hamiltonian we have used to describe our system neglects several higher order processes that occur in our system. In this section, we estimate the contributions of these processes.

#### Interchain Tunneling

Tunneling between chains is excluded from the spin-mapping we have described, though under certain conditions it produces exotic transverse superfluidity, as described in Ref. [145]. For our purposes, these tunneling processes serve only to take the system out of the Hilbert space described by the spin model. Most of our experiments

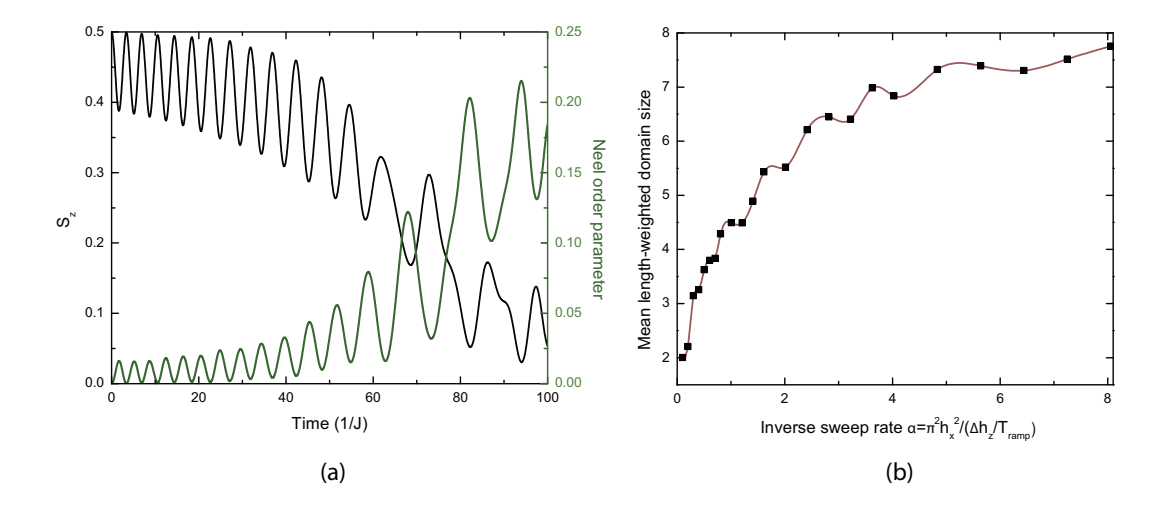


Figure 6.5: Exact diagonalization dynamics of the Ising chain for small chains. (a) The time evolution of the mean magnetization  $S_z$  and the Neel order parameter for a system of eight spins with periodic boundary conditions during a linear ramp of the longitudinal field  $h_z$  from 1.25 to 0.85. The total ramp time is 100/J and the transverse field  $h_x$  is 0.1. (b) The mean length-weighted domain length at the end of a ramp in the same system from  $h_z = 4$  to  $h_z = 0.1$ . For this initial value of  $h_z$ , the overlap with the paramagnetic state is very good and the are almost no oscillations in an adiabatic ramp.

were performed at a transverse lattice depth of 45Er, corresponding to an interchain tunneling rate of  $t_{\rm transverse} = 2\pi \times 0.07 {\rm Hz}$ . This tunneling rate is basically negligible on our experiment timescale of 250ms. Some data was taken at 35Er transverse lattice depth. At this depth the transverse tunneling rate is  $t_{\rm transverse} = 2\pi \times 0.27 {\rm Hz}$ , which is small compared to our lattice inhomogeneities, and so results in highly-suppressed, off-resonant Rabi-flopping. In practice, increasing the transverse lattice from 35Er to 45Er results in a modest  $\sim 5\%$  improvement in the quality of the Mott insulator after transitioning to the antiferromagnetic state and back.

#### Second Order Tunneling

In addition to nearest-neighbour tunneling which creates doublon-hole pairs, and proceeds at a rate  $\sqrt{2}t$  when the tilt E=U, there remains a second-order tunneling process which creates triplon-hole-hole trios at a rate  $t_{\text{s.o.}} = \sqrt{3} \frac{t^2}{U}$ . For our longitudinal lattice depth of 14Er, and interaction energy  $U=2\pi\times416\text{Hz}$ , we find  $t_{\text{s.o.}}=2\pi\times0.4$  Hz. Because our system is continuously tilted, all such transitions will be tuned through resonance. For our typical experiment,  $R_{\text{ramp}}=\frac{\frac{1}{2}U}{250\text{ms}}\approx2\pi\times840\text{Hz}^2$ , so the Landau-Zener adiabatic transition probability to the triplon state  $p_{\text{triplon}}=1-\exp\left(2\pi\frac{t_{\text{s.o.}}^2}{R_{\text{ramp}}}\right)=0.8\%$ . In future experiments with slower ramps, both this effect and the closely related second-order Stark-shift will become more of a concern. These can be further suppressed relative to the desired dynamics by increasing the longitudinal lattice depth, at the expense of slower many-body dynamics. It bears mentioning that for our experimental parameters the triplon state experiences an additional shift of approximately 22Hz, due to multi-orbital interactions [191, 100].

#### Impact of physics beyond the Hubbard Model

For a  $14E_r$  lattice, the next-nearest neighbour tunneling rate is suppressed relative to that of the nearest neighbour [98] by a factor of  $\sim 300$ , making the total rate  $t_{\text{NextNeighbour}} = 2\pi \times 0.04 \text{Hz}$ , which is negligible on present experiment timescales. The longitudinal nearest-neighbour interaction shift for one atom per lattice site is  $\sim 10^{-3} \text{Hz}$ , and interaction driven tunneling [59] occurs with a rate of  $2\pi \times 0.3 \text{Hz}$ .

## 6.2 Observation of the phase transition

Our experiments start with a single layer two-dimensional Mott insulator of  $^{87}$ Rb atoms in a  $35E_r$  lattice with 680 nm spacing. The atoms are in the  $|F=1,m_f=-1\rangle$  state and the initial fidelity of the Mott insulator is 0.95(2). We generate our effective  $h_z$  by tilting the lattice potential by E per lattice-site, which is achieved via a magnetic field gradient along the x direction (defined in Fig. 6.6(a)). This gradient is applied in two steps - first a fast ramp (in 8 ms) to E=0.7U, just below the transition point [163, 137] at E=U+1.85t ( $h_z=1-0.66h_x$ ), followed by a slow linear ramp (in 250 ms) across the transition ending at 1.2U, adiabatic on the many-body timescale. Before starting the slow gradient ramp, the lattice depth along the y direction is increased (in 2 ms) typically to  $45(7)E_r$ , while the depth along the x direction is reduced to  $14(1)E_r$ . This decouples the system into 1D chains with significant tunneling only along their lengths. Simultaneously, we compensate the tilt inhomogeneity arising from harmonic confinement, leaving only residual inhomogeneity arising from our lattice projection method [13].

We probe the state of the system at different points as it undergoes the phase transition in one of two ways. We can either perform an in-situ measurement or a 1D expansion of the chains to achieve noise correlation interferometry. In both cases, we use fluorescence imaging after pinning the atoms in a deep lattice to obtain the density distribution with single atom/single lattice-site resolution. Images far on the Mott side of the transition are used to select chains of atoms within the first shell of the insulator. The phase transition is then studied only within these chains, with quantitative curves employing data only from the single chain with lowest disorder.

Lattice depths are calibrated to 15% using Kapitza-Dirac scattering, however the width of single-site transition regions was found to be a more sensitive probe of the longitudinal tunneling rate and hence the longitudinal lattice depth and accordingly was employed throughout these experiments.

The magnetic field gradient is calibrated using lattice modulation spectroscopy. In the presence of a potential gradient E per lattice site, modulation of the lattice depth along the chains causes resonant excitation at two frequencies, U+E and U-E corresponding to an atom in the Mott insulator moving up or down gradient. We detect these excitations as a reduction in the value of  $p_{\text{odd}}$  using in-situ imaging. Using the mean of the two resonances, we obtain the interaction energy  $U=430(20)\,\text{Hz}$  at  $16E_r$  longitudinal lattice,  $45E_r$  transverse lattice (corresponding to  $U=413(19)\,\text{Hz}$  at  $14E_r$  longitudinal lattice, where the experiment operates, which agrees with a band-structure calculation of  $401(25)\,\text{Hz}$ ). The separation between the resonances as a function of applied gradient is used to calibrate E. At zero applied magnetic field gradient, we find the stray gradients to be less than 0.02U.

# 6.2.1 In-situ observation of the phase transition and its reversibility

We initiate the gradient ramp on the paramagnetic side of the phase transition (typically at E/U = 0.7), as the initial Mott state with single site occupancy of 0.95(2) has good overlap with the paramagnetic ground state (Fig. 6.6(a)i). At the end of the ramp (E/U = 1.2), we observe an even occupation with probability 0.90(2) (Fig. 6.6(a)ii), as expected for an AF phase in the magnetic model where the spin-

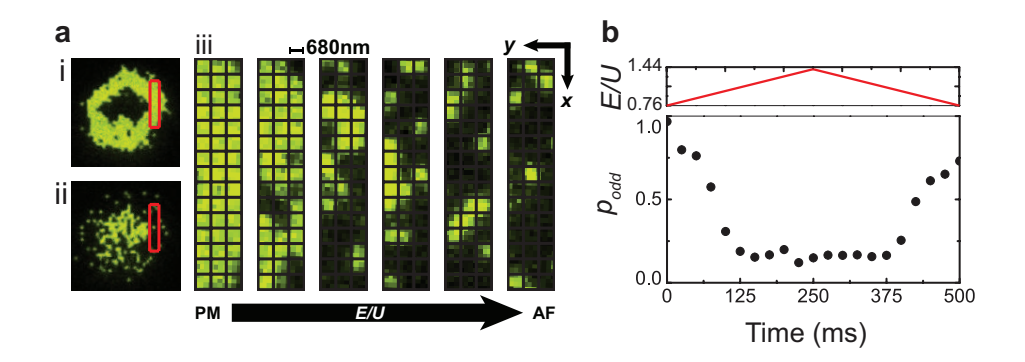


Figure 6.6: Probing the paramagnet to antiferromagnet phase transition. (a) Representative single-shot images as the tilt is swept adiabatically through the phase transition in 250 ms. The upper image (i) shows near-perfect n=1 (bright) and n=2 (center dark) Mott insulator shells in PM phase. The lower image (ii) is the inverted shell structure characteristic of the staggered ordering of the AF phase after a tilt along the x-direction. The inversion occurs because chains of sites in a shell with N atoms per site are converted into a staggered phase wherein sites alternate between N-1 and N+1 atoms, and so a shell with even occupation becomes a region of odd occupation, and vice-versa. The remaining pictures (iii) are several chains (within the red rectangles in i and ii) of the N=1 shell at various points during the sweep, t = 0, 50, 100, 150, 175 and 250 ms, showing AF domain formation. (b) To demonstrate the reversibility of the transition, we adiabatically ramp from the PM phase into the AF phase and back in 500 ms. The probability that a site in the N=1 shell has odd occupation at various points during the ramp is observed to drop, and subsequently revive, as expected when the system leaves and then returns to the PM phase.

spin interaction overwhelms the effective field  $h_z$ . In between, density-wave ordered regions begin to form, as shown in Figure 6.6(a)iii. Figure 6.7 shows  $p_{\text{odd}}$  at various times during this ramp. A crucial characteristic of an adiabatic transition is that it is reversible. Figure 6.6(b) shows  $p_{\text{odd}}$  during a ramp from a PM to an AF and back. The recovery of the singly occupied sites is evidence of the reversibility of the process, and hence that the intermediate state is in fact an antiferromagnet.

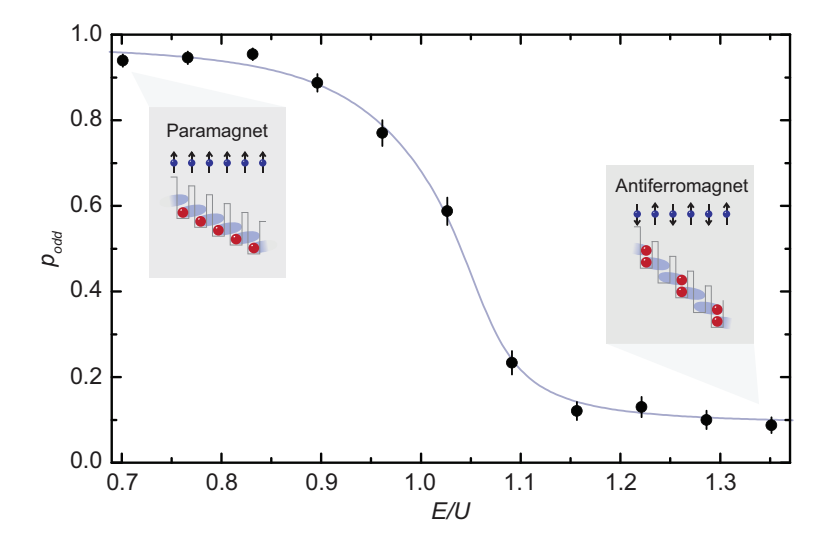


Figure 6.7: A closer look at the PM to AF quantum phase transition within an N = 1 shell, showing  $p_{\text{odd}}$  vs. tilt. Errorbars reflect  $1\sigma$  statistical errors in the region-averaged mean  $p_{\text{odd}}$ . The blue curve is a guide for the eye.

#### 6.2.2 Noise correlation detection of long-range order

We directly verify the existence of staggered ordering in the AF phase via a 1D quantum noise correlation measurement [2]. We perform this measurement by increasing the lattice depth along the chains to  $35E_r$  within 5ms and then rapidly switching off that lattice to realize a 1D expansion. After an expansion time of 8 ms, the atoms are pinned for imaging. To extract information about density wave ordering in the chains, several hundred images (250 for paramagnetic, 500 for antiferromagnetic phase) each containing 15 chains, are fitted to extract the atom positions, and then spatially autocorrelated and averaged as described in Ref. [60].

The resulting spatial autocorrelation is plotted in Figure 6.8 at both the beginning (i) and end (ii) of the ramp from the PM phase to the AF phase. In the PM phase the spectrum exhibits peaks at momentum difference P = h/a, characteristic of

a Mott insulator [60]. In the AF phase peaks at P = h/2a appear, indicative of the emergence of a spatial ordering with twice the wavelength. In principle the mean domain size can be extracted from the P = h/2a peak width, however our measurement is broadened by both finite expansion time and aberration arising from the fact that the 1D expansion is performed not in free space but in slightly corrugated confining tubes.

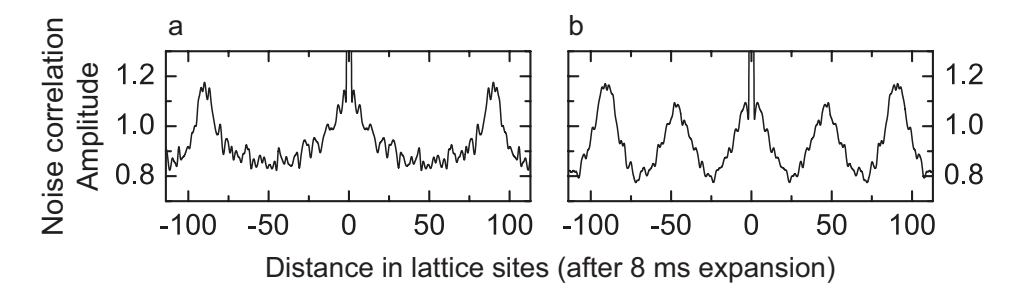


Figure 6.8: Noise correlation measurement after 8 ms time of flight expansion along the chains. (a) In the PM phase, peaks at momentum h=a correspond to a periodicity of one lattice site before expansion, characteristic of a Mott insulator. (b) In the AF phase, additional peaks at momentum h=2a indicate the existence of staggered ordering, with a periodicity of two lattice sites.

### 6.2.3 Single-site study of the transition

In the presence of harmonic confinement, a high resolution study reveals that the spins undergo the transition sequentially due to the spatial variation of the effective longitudinal field. Figure 6.9(a) shows  $p_{\text{odd}}$  vs. tilt for two different rows of a harmonically confined Mott insulator, separated by seven lattice sites. These two rows tune through resonance at different tilts, as can be understood from the energy level diagram Figure 6.4(a). This regime, described by an inhomogeneous field Ising model, presents a number of new possibilities. For example, Schroedinger cat states [118]

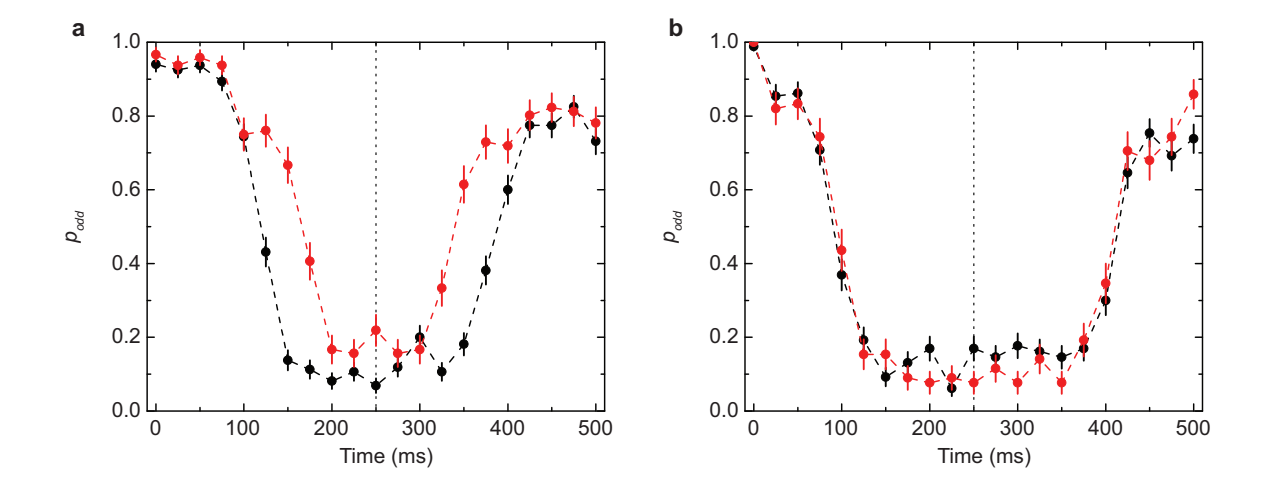


Figure 6.9: Impact of harmonic confinement. For a ramp across the transition (in 250 ms) and back, (a) harmonic confinement broadens the transition, inducing rows of the cloud seven lattice sites apart to undergo the transition at different applied tilts. (b) Once the confinement has been properly compensated, the average transition curves from the two rows overlap. Not apparent from these averaged curves is a small amount of residual tilt inhomogeneity. All errorbars are  $1\sigma$  statistical uncertainties derived from the mean of  $p_{\text{odd}}$  averaged over a region.

could be created by preparing the first spin in the chain in a superposition of up and down states and then sequentially ramping through the remaining spins. We next realize a homogeneous field Ising model by eliminating the harmonic confinement immediately before the slow ramp into the AF phase. Figure 6.9(b) demonstrates that in this case different rows transition almost simultaneously, as anticipated theoretically (Fig. 6.4(b)).

After compensating the harmonic confinement, we are able to resolve residual site-to-site tilt inhomogeneities, caused by lattice beam disorder. For the rest of this work we will focus on a single six-site chain with particularly low inhomogeneity. We identify such a chain by imaging individual lattice sites as the system is tuned across the PM-AF transition. Figure 6.10 shows  $p_{\text{odd}}$  across the transition for one of the sites

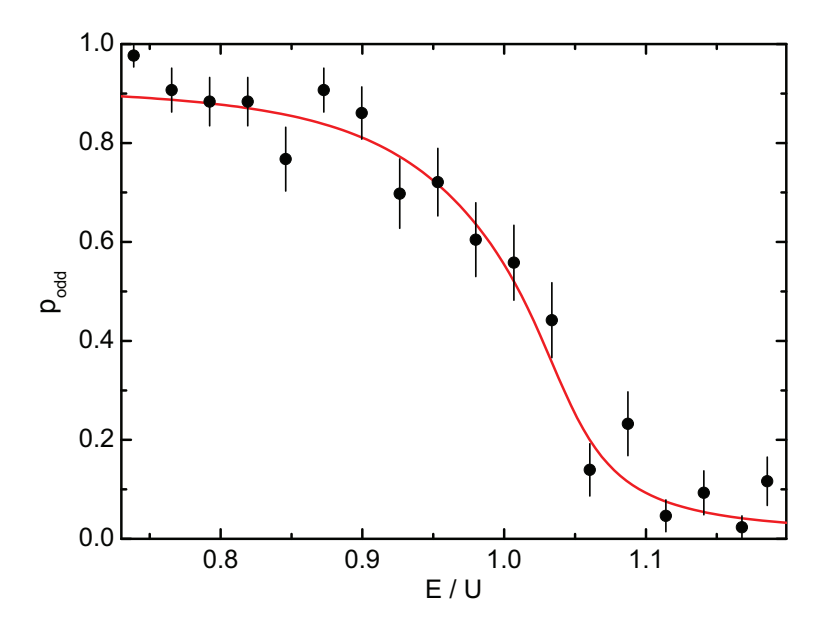


Figure 6.10: Single-site transition curve. The theory curve reflects a zero temperature exact diagonalization calculation of the ground state of a chain of six Ising spins (the shape of the  $p_{\text{odd}}$  curve is insensitive to chain length) with periodic boundary conditions. The curve has been offset and rescaled vertically to account for defects arising from both the initial MI, and heating during the ramp. The theory allows us to extract a lattice depth of  $14(1)E_r$ . We attribute the residual fluctuations around the expected curve to residual oscillations reflecting non-adiabaticity arising from that fact that the ramp was initiated too close to the transition. The error bars are  $1\sigma$  statistical uncertainties.

fitted with a theory curve, while Figure 6.11 shows  $p_{\text{odd}}$  for all the six adjacent sites (black curves), versus tilt, as the system is ramped across the transition. The r.m.s. variation in the fitted centers is 6Hz, significantly less than their mean 10% - 90% width of 105(30)Hz, corresponding to the effective transverse field  $2^{3/2}t = 28$ Hz.

By quickly jumping across the transition with tunneling inhibited, and then ramping slowly across the transition in reverse with tunneling allowed (red curves, taken under slightly different conditions), we are able to rule out large, localized potential steps that would otherwise prevent individual spins from flipping. The curves in Fig-

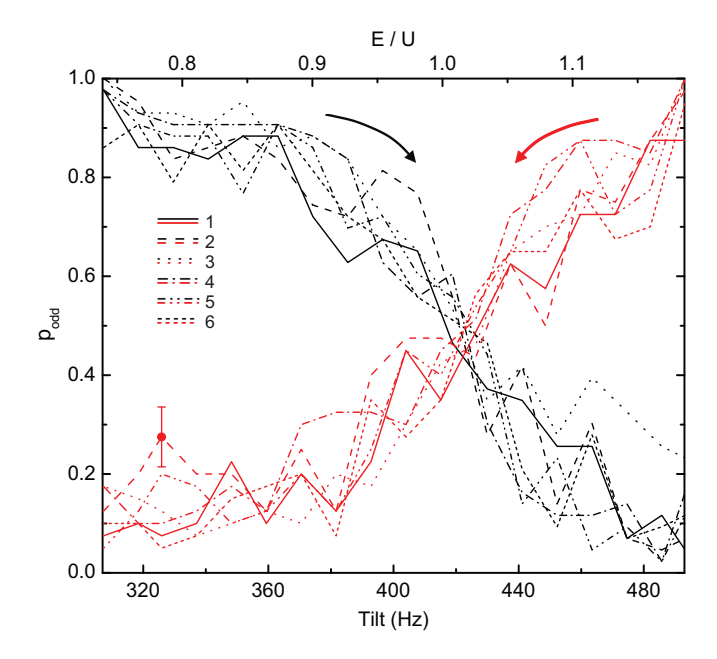


Figure 6.11: Site-resolved transition in near-homogeneous Ising model.  $p_{\text{odd}}$  of six individual lattice sites forming a contiguous 1D chain, versus the tilt, shown for both forward (black) and reverse (red) ramps. The spins transition at the same applied field to within the curve width, set by quantum fluctuations. A typical  $1\sigma$  statistical errorbar is shown. The single-site widths are consistent with a longitudinal lattice depth of  $14(1)E_r$ , in agreement with a Kapitza-Dirac measurement of  $15(2)E_r$ . The reverse curve demonstrates our ability to adiabatically prepare the highest energy state of the restricted spin Hamiltonian.

ure 6.11 provide our best estimate of the inhomogeneity. However, exact determination of the site-to-site disorder using this technique is complicated by the many-body nature of the observed transition. Accordingly, a technique such as site-resolved modulation spectroscopy would have to be used to ensure that the inhomogeneities are small enough to study criticality in long, homogeneous Ising chains.

## 6.3 Domain formation and adiabaticity timescales

The magnetic interactions should produce even-length domains of dark sites, corresponding to AF spin domains. To quantify the length of these AF domains we study the length of the measurable dark domains, defining a dark domain as a contiguous string of dark sites that is bounded either by a site with an atom or an edge of the region of interest. We then calculate the mean length-weighted dark chain length from this data. The length-weighting is necessary because the quantity of interest is how many spins in the AFM participate in a domain of a given size. For example, Bragg diffraction experiments would also give a signal that is proportional to the length-weighted domain size, and the Scherrer formula [140] used in X-ray crystallography gives a volume-weighted domain size.

Defects in the initial Mott insulator (MI) reduce the effective system size. Their appearance can produce an overestimate of the dark chain length by either connecting two dark chains, or appearing on the end of a dark chain. The initial MI defect probability is typically 4% per site over an entire n=1 shell, after correcting for losses during imaging.

Atom-losses during the ramp can have similar consequences for the observed dark domain length, and can also suppress the observed dark domain length by knocking atoms out near the end of the ramp once the AF has already formed. This atom-loss rate is estimated from the MI 1/e lifetime in the tilted lattice, measured to be 3.3 seconds. To perform this measurement we first ramp to a tilt of 300Hz per lattice site and tune the lattice depths to 45Er and 14Er for transverse and longitudinal lattices, respectively. We then hold for a variable time, and measure the remaining

atom number.

A worst-case estimate for the impact of missing atoms can be reached from the fraction of the time that the system is missing no atoms at the end of the ramp. The six-site chain analyzed in the main text is initially fully occupied 79% of the time. During the time it takes the dark-domain length to grow to 4 lattice sites (60ms), heating only reduces this number to 73%.

We start by studying the domain size vs. the applied gradient when the system is prepared adiabatically. Figure 6.12(a) shows the observed mean length-weighted dark domain length extracted from 43 single-shot images per tilt, as the system is ramped from the PM phase into the AF phase. The dark domain length is here defined as the number of contiguous dark sites. On the AF side of the transition, this mean dark domain length grows to 4.9(2) sites, on the order of the system size of six sites.

We next investigate the impact of ramp rate on the transition from the PM phase into the AF phase in the homogeneous chain. The red curve in Figure 6.12(b) shows  $p_{\text{odd}}$  as a function of ramp speed across the transition, which may be understood qualitatively as the fraction of the system that has not transitioned into AF domains of any size. The time required to flip the spins is  $\sim 50$ ms, consistent with tunneling induced quantum fluctuations driving the transition. The black curve in Figure 6.12(b) is the mean length-weighted dark domain length as a function of ramp rate. As above, the mean dark domain length saturates near 4.8(2) sites. The remaining defects likely result from imperfect overlap of the initial MI with the PM state at finite  $\tilde{\Delta}$ , as well as defects of the initial MI and heating during the ramp.

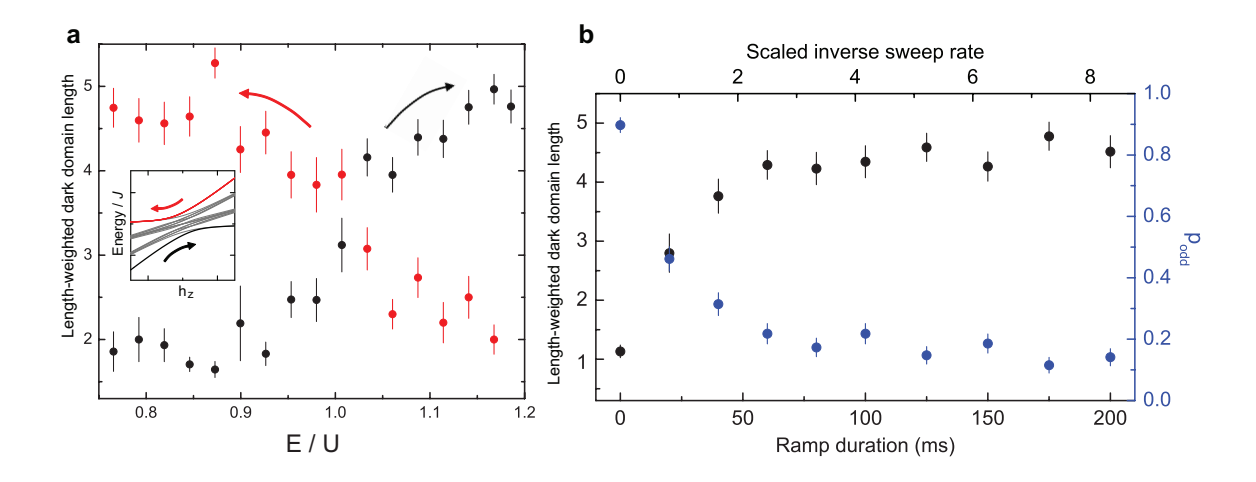


Figure 6.12: Dynamics of antiferromagnetic domain formation. Within a single sixsite chain with low disorder, (a) shows the mean dark-domain length as a function of the tilt in units of U, for both forward (black) and reverse (red) ramps. As the system enters the AF phase the mean dark domain length grows until it approaches the chain length. Domain formation in the reverse ramp, beginning on the AF side of the transition, demonstrates the adiabatic generation of AF domains on the PM side of the transition, corresponding to the highest energy state of the spin Hamiltonian (inset). Within the same chain, (b) shows  $p_{\text{odd}}$  (blue) and dark domain length (black) versus the duration  $T_{\text{ramp}}$  of the ramp from E/U = 0.7 to E/U = 1.2. The top axis shows the scaled inverse sweep rate  $\alpha = 8\pi^2 t^2/(\Delta E/T_{\text{ramp}})$ , where  $\Delta E$  is the sweep range in Hz, and t is the tunneling rate, in Hz, along the chain. The characteristic timescale for domain formation is  $\alpha \approx 2$ , or  $T_{\text{ramp}} \approx 50$  ms, indicating that tunneling along the chain is the source of the quantum fluctuations that drive domain formation. Errorbars for the dark chain lengths are  $1\sigma$  statistical uncertainties, arising from the number of detected domains of each length. Those for  $p_{odd}$  are the  $1\sigma$  statistical uncertainty in the mean of the six-site chain.

## 6.4 Preparation of the highest energy state

While the antiferromagnetic domain formation discussed thus far occurs in spinchains that remain in a quantum state near the many-body ground state, we can also produce antiferromagnetic domains that correspond to the highest energy state of the restricted spin Hamiltonian. This is achieved by starting with the Mott insulator and rapidly ramping the field gradient through the transition point with tunneling inhibited, then adiabatically ramping back with tunneling permitted, as described in the previous section. This prepares a PM on the AF side of the transition, and adiabatically converts it into an AF on the PM side. The resulting dark domain length data are shown in Figure 6.12(a) (red curve), demonstrating that these high energy states are sufficiently long-lived to support domain formation. Similar ideas have been proposed for preparation of difficult-to-access many-body states using the highest energy states of Hamiltonians with easily prepared ground states [176].

#### 6.4.1 Entropy and thermalization in the spin chains

One source of much confusion in the literature is the picokelvin range temperatures often quoted as necessary for the observation of magnetic ordering in optical lattice systems [36]. Therefore it might be surprising to the reader that we have achieved such ordering without additional cooling in the lattice [189, 129, 128]. To clarify this issue, it is important to realize that ultracold gases in optical lattices are effectively isolated from their environment, and as such it is entropy and not temperature which is constant as system parameters are tuned. We have demonstrated spin polarized Mott insulators with defect rates at the percent level, corresponding to a configurational entropy far below the spin entropy required for magnetic ordering even with traditional superexchange interactions. In our scheme, we have used the Mott insulator to initialize a magnetic system with low spin entropy and then engineered a magnetic Hamiltonian whose paramagnetic ground state possesses good overlap with the initial Mott state, which we subsequently tune through a quantum phase transition to produce the antiferromagnetic state. This is a general recipe [63]

Mott fidelity $p_{\text{odd}}$	Entropy $(S/Nk_B)$	LW mean size (thermalized)	LW mean chain length (unther- malized)
0.95	0.23	22	39
0.975	0.13	52	79
0.99	0.063	144	199

Table 6.1: Configurational entropy per particle for various Mott fidelities. If the spin degrees of freedom thermalize efficiently with the Mott degrees of freedom, the spin entropy will then be equal to the Mott entropy. The corresponding mean AF domain size is then computed for each Mott entropy. In the absence of thermalization, the Mott defects break the spin chain into disconnected subsystems, whose mean size is computed in the fourth column, and is comparable to the mean chain length in the presence of thermalization.

and the main challenge, rather than further cooling, is the necessity of performing sufficiently slow adiabatic ramps to minimize diabatic crossings of manybody energy gaps.

We now proceed to study entropy and thermalization in our system more quantitatively. Table 6.1 shows the entropy per particle  $(S/Nk_B)$  for several different Mott insulator fidelities  $(p_{\text{odd}})$ , assuming a chemical potential  $\mu = U/2$ , as well as the mean length-weighted AF domain size D in an infinite 1D magnetic system with the same entropy per particle. Here  $D = 2(2 - \epsilon)/\epsilon$ , where the spin-dislocation probability in the AF  $\epsilon$  is defined by  $S/Nk_B \approx (\epsilon/2) \left[1 + \log(1/\epsilon)\right]$ . Spin defects are ignored as they are both dynamically and thermodynamically unlikely. The entropy per particle can be related to the Mott insulator fidelity by:  $S/Nk_B = \log\left[\frac{2}{1-p_{\text{odd}}}\right] - p_{\text{odd}}\log\left[\frac{2p_{\text{odd}}}{1-p_{\text{odd}}}\right]$ . If such thermalization took place in our finite length chain of six sites (with initial fidelity 97.5%), the mean domain size would be limited by the system size to 5.3 sites.

Experimentally, we find most Mott defects to be unbound doublons and holes, which do not directly map to excitations in the spin model. The large energy gap

present in our tilted lattice, combined with conservation of particle number, make it difficult for these Mott defects to thermalize with spin degrees of freedom. Such thermalization would require, for example, migration of a doublon to a hole, or decay via a very high order process into several spin defects- quite unlikely within the experimental timescale. Consequently, these nearly static defects act as fixed boundary conditions that limit the effective length of the simulated spin chains. Table 6.1 also provides the expected uninterrupted chain length, computed as  $L_{\text{sys}} = (1+p_{\text{odd}})/(1-p_{\text{odd}})$ .

# 6.5 Prospects for studying criticality

It is clear from the previous section that entropy does not currently limit the length of the Ising chains in our system. Rather, the current limitation on studying critical physics in longer chains is the presence of inhomogeneities in the longitudinal field ( $\delta_z^i \neq 0$ ). This impacts the critical behaviour by breaking the translational symmetry, inducing different sites to transition at different applied tilts. Accordingly, the resulting many-body energy gaps, dynamical timescales [50, 92], and entropy of entanglement [186] are different from the homogeneous case.

The next challenge in extending the chain length is the higher order processes not included in the Ising Hamiltonian discussed in Sec. 6.1.7. These processes are weaker by a factor of t/U than the transverse field. However, for studying criticality in a chain of length N, we need to consider the many-body gap that is on order t/N, and for large enough N, the higher order processes cannot be ignored. Larger chain lengths can be achieved by reducing t, but eventually more fundamental limits of lattice heating (Sec. 3.2.1) or background gas collision lifetime are encountered. A

better approach would be to increase U, either by using a Feshbach resonance or using a lighter species such as bosonic lithium. Critical physics can be probed by measuring the scaling of domain formation with ramp speed (Sec. 6.3) or the sharpening of the order parameter for increasing chain length as has been recently demonstrated with ion trap quantum magnetism experiments [94].

# 6.6 Manipulation of individual spins

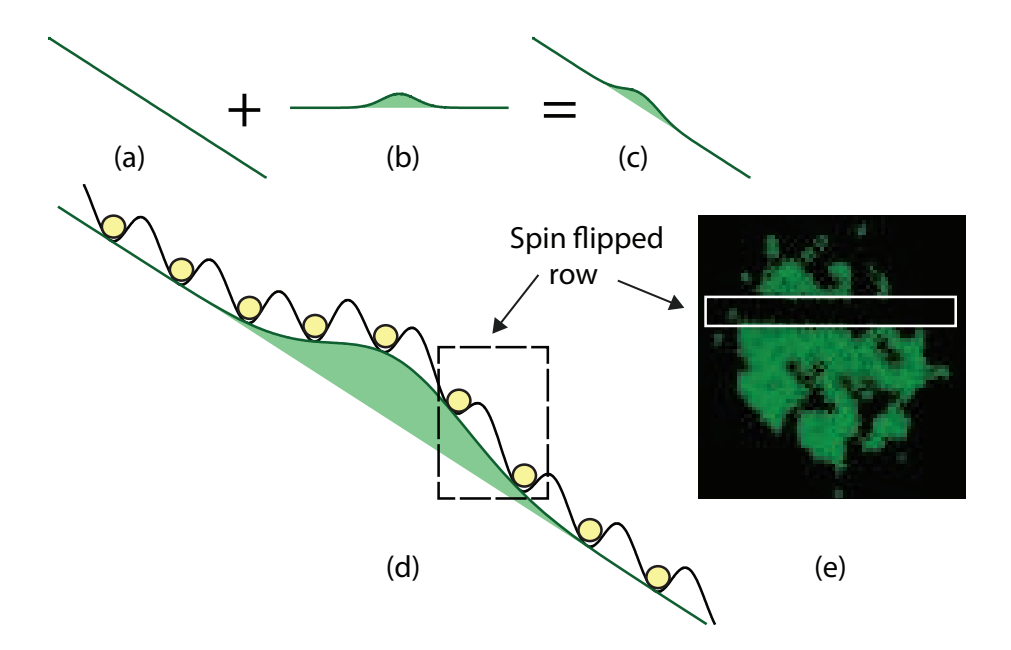


Figure 6.13: Manipulation of the spin state in the chains. The potential due to the magnetic gradient shown in (a) is combined with a projected Gaussian optical potential (b) created with a spatial light modulator. This gives the total potential in (c). The pair of atoms at the steepest point of the potential, shown within the box in (d), will transition first as the gradient is increased. This is seen in the raw image (e) as two dark rows in the uncoupled vertically oriented chains.

The manipulation of the state of individual atoms in an optical lattice is an important goal for optical lattice-based quantum computation. Single site manipulation

of the hyperfine state in a Mott insulator has been recently demonstrated, with only a small perturbation to the external state [188]. In our system, we have demonstrated the manipulation of single pseudospins using light patterns created with a spatial light modulator. While this could find applications as a single-qubit gate, it opens the path to more immediate interesting experiments on spin transport in a strongly interacting system (see [34] for transport of domain wall excitations in our spin Hamiltonian). For example, a single flipped spin in the paramagnetic state or a domain wall excitation in the antiferromagnet can be created to observe its diffusion dynamics, or multiple excitations can be created to study their interaction.

We start with chains on the PM side in a gradient below the transition point and use a spatial light modulator (Sec. 4.7) to project light with a Gaussian profile along the direction of the chain, with width corresponding to a few sites, and a flat profile along the direction perpendicular to the chains, as seen in Fig. 6.13(a-d). The dipole potential due to the light reduces  $h_z$  on one side of the Gaussian profile, bringing the spins closer to the transition point and increases it on the other. We then ramp the magnetic gradient to the lowest point that induces spin flips, which causes the spins in a single row to flip as seen in Fig. 6.13(e).

# Chapter 7

# Outlook

Quantum gas microscopy opens many possibilities for studying ultracold atoms in optical lattices. We have demonstrated its potential for microscopic studies of quantum phase transitions. In this section, we summarize ideas for further experimental work.

An interesting extension of our work on studying density correlations in Mott insulators would be to look at these correlations in strongly interacting one-dimensional gases, also known as Tonks gases. An ensemble of Tonks gases can be prepared in our system by turning off one of the lattice axes, or reducing it substantially [104, 139]. In the Tonks regime, the bosons cannot pass through each other because of the strong interactions, and their motion is strongly correlated. The density correlations in such as a gas should be long-range compared to the exponentially decaying correlations in the Mott insulator.

We have looked at the dynamics in our system during quick ramps from the superfluid to the insulator. It would be interesting to study the response of the system to sudden jumps of the lattice depth in the superfluid regime. In addition to the familiar gapless Bogoliubov mode, the superfluid also has another type of excitation that is gapped, known as the amplitude or Higgs mode. This mode corresponds to oscillations in the magnitude of the order parameter, or in other words oscillations of the number squeezing at constant average density. In two dimensions, it is predicted that this mode is strongly damped [90] because of coupling to Bogoliubov modes, but that is not the case in 3D.

While we have worked hard on reducing disorder in our lattice, several intriguing phases can explored by introducing disorder in a controlled way, e.g. Anderson [23] and Bose glass [54] phases. The use of the spatial light modulator in combination with the high resolution optics allows us to create arbitrary disorder patterns with spatial periodicities down to the micron range, leading to large a mobility edge for localization. In addition, it should be easy to change the disorder on each experimental cycle to average over disorder patterns. By exploring disorder with different power spectra, comparisons to theory should be possible.

The optical lattice tilting technique we have used to study quantum magnetism in an Ising model can be extended in several ways. Tilting by the band gap can realize the transverse Ising model without a longitudinal field [147]. Tilting by the interaction in a 2D geometry can lead to different interesting phases depending on the tilt direction [145]. For example, if the tilt is along one of the lattice axes, the ground state has alternating rows of double occupancy and no occupancy along the tilt direction, an ordering that is stabilized by second order processes. Tilting along the diagonal leads to a checkerboard of doubly occupied sites and empty sites. In

kagome and decorated square lattices, frustrated models appear including quantum clock and dimer models, with quantum liquid [15] and solid phases.

Within the magnetic model we studied, we have demonstrated flipping single spins. It would be interesting to study spin diffusion in the system, or create packets with momentum and study their interaction. An exciting prospect is studying longer chains where critical physics can be observed, e.g. measurements of critical exponents or observation of critical slowdown near the transition point. There have been recent suggestions on using time of flight methods to put lower bounds on the entanglement of an arbitrary state of ultracold atoms in a lattice [44]. A direct demonstration of the "quantum" aspect of quantum magnetism would be measurement of such entanglement monotones across the transition to verify that entanglement builds up in the critical regime.

A current limitation of our imaging technique is that it is currently insensitive to the hyperfine state of the atoms and measures only the parity of the atom number. Sensitivity to the internal state would be desirable for proposals to study magnetism using superexchange [49]. In principle, this issue can be addressed to some extent by "blowing away" atoms in one of the hyperfine states using resonant light before imaging [188]. For alkaline earth atoms, the situation is easier because of the presence of metastable states for shelving one of the hyperfine states. Another possibility that is implementable in our microscope is to have the atoms in the different hyperfine states also be in different magnetic states that can be separated spatially using a magnetic gradient along the direction perpendicular to the 2D plane. If the spin states are in different planes, they can be distinguished because of the short depth of

focus of our imaging system. For experiments with a single spin state, similar ideas can be used to circumvent the parity imaging problem. For example, if we start with two atoms in the same spin state on a site, they can be made to undergo spin-changing collisions [190] that put them in different magnetic states that can then be imaged as just described.

The ability to engineer the potential landscape of the atoms in the lattice should open new possibilities for lattice cooling. Entropy in lattice systems is usually distributed in a non-uniform way across the sample because of spatial variations in the specific heat capacity. For example, gapless superfluid regions can usually store more entropy than gapped insulating regions, and while increasing the lattice depth, entropy is expelled into the superfluid regions, a process in which the dynamical issues are important. It may be possible to engineer the potential landscape to have reservoirs of superfluid regions distributed across the sample to allow for fast thermalization [150, 38].

Using a lower resolution lens setup, we have demonstrated in the same apparatus the use of projection techniques to create vortices in a Bose-Einstein condensate. This was achieved by transferring angular momentum from a light beam to the atoms using a Raman transition [29, 4]. The light beam with angular momentum was created using a phase hologram, which allowed the engineering of vortex patterns with arbitrary geometry and charge. With our high resolution objective, it should be possible to project a much denser vortex pattern onto the atoms. Because of the analogy to quantum Hall physics, the low filling factor regime of atoms to vortices is interesting to reach [167, 177, 65]. Another exciting related prospect would be the

direct observation of the binding/unbinding of thermally activated vortex-antivortex pairs in the two-dimensional gas expected in a Berezinskii-Kosterlitz-Thouless phase transition [110, 83].

Finally, the quantum gas microscope is a step along the path towards quantum computation with neutral atoms in optical lattices [30]. Compared to other quantum computing architectures such as ion traps, optical lattices have the advantage of scalability. Preparation of a Mott insulator in a definite hyperfine state meets the initialization requirement. The ability to use quantum gas microscopes to manipulate the hyperfine state of individual atoms [188] or the spin state in the one-dimensional chains demonstrated in this work satisfies the requirement of single-qubit gates. Two-qubits gates can be achieved using recently demonstrated Rydberg dipole-dipole interactions [185, 62, 164]. Alternatively, the one-way computation model [153] can be implemented, utilizing entangled states created through controlled collisions in a spin-dependent lattice [125]. In both schemes, single-site addressability in a lattice is necessary.

- [1] Ehud Altman and Assa Auerbach. Oscillating superfluidity of bosons in optical lattices. *Phys. Rev. Lett.*, 89(25):250404, Dec 2002.
- [2] Ehud Altman, Eugene Demler, and Mikhail D. Lukin. Probing many-body states of ultracold atoms via noise correlations. *Physical Review A*, 70(1):013603+, Jul 2004.
- [3] Ehud Altman, Walter Hofstetter, Eugene Demler, and Mikhail D. Lukin. Phase diagram of two-component bosons on an optical lattice. *New Journal of Physics*, 5(1):113+, September 2003.
- [4] M. F. Andersen, C. Ryu, Pierre Cladé, Vasant Natarajan, A. Vaziri, K. Helmerson, and W. D. Phillips. Quantized rotation of atoms from photons with orbital angular momentum. *Phys. Rev. Lett.*, 97(17):170406, Oct 2006.
- [5] M. H. Anderson, J. R. Ensher, M. R. Matthews, C. E. Wieman, and E. A. Cornell. Observation of Bose-Einstein Condensation in a Dilute Atomic Vapor. Science, 269(5221):198–201, July 1995.
- [6] P. W. Anderson. Antiferromagnetism. theory of superexchange interaction. *Phys. Rev.*, 79(2):350–356, Jul 1950.
- [7] P. W. Anderson. Localized magnetic states in metals. *Phys. Rev.*, 124(1):41–53, Oct 1961.
- [8] P. W. Anderson. The Resonating Valence Bond State in La2CuO4 and Super-conductivity. *Science*, 235(4793):1196–1198, March 1987.
- [9] P. W. Anderson. The Theory of Superconductivity in the High-Tc Cuprate Superconductors. Princeton University Press, 1997.
- [10] V. Anisimov and Y. Izyumov. *Electronic structure of strongly correlated mate*rials. Springer-Verlag, Berlin Heidelberg, 2010.
- [11] N. W. Ashcroft and N. D. Mermin. *Solid State Physics*. Saunders College Publishing, Fort Worth, TX, 1976.

[12] M. C. Bañuls, J. I. Cirac, and M. B. Hastings. Strong and weak thermalization of infinite nonintegrable quantum systems. *Phys. Rev. Lett.*, 106(5):050405, Feb 2011.

- [13] W. S. Bakr, A. Peng, M. E. Tai, R. Ma, J. Simon, J. I. Gillen, S. Fölling, L. Pollet, and M. Greiner. Probing the SuperfluidtoMott Insulator Transition at the Single-Atom Level. *Science*, 329(5991):547–550, July 2010.
- [14] Waseem S. Bakr, Jonathon I. Gillen, Amy Peng, Simon Foelling, and Markus Greiner. A quantum gas microscope detecting single atoms in a Hubbard regime optical lattice. Aug 2009.
- [15] Leon Balents. Spin liquids in frustrated magnets. Nature, 464(7286):199–208, March 2010.
- [16] V. I. Balykin, V. S. Letokhov, Yu. B. Ovchinnikov, and A. I. Sidorov. Quantum-state-selective mirror reflection of atoms by laser light. *Phys. Rev. Lett.*, 60(21):2137–2140, May 1988.
- [17] B. Barbara, Y. Imry, G. Sawatzky, and P.C.E. Stamp. Quantum Magnetism: Proceedings of the NATO Advanced Study Institute on Quantum Magnetism. Springer Science, Dordrecht, The Netherlands, 2008.
- [18] J. Bardeen, L. N. Cooper, and J. R. Schrieffer. Theory of superconductivity. *Phys. Rev.*, 108(5):1175–1204, Dec 1957.
- [19] T. Basché, W. E. Moerner, M. Orrit, and U. P. Wild. Single-Molecule Optical Detection, Imaging and Spectroscopy. Wiley-VCH, Cambridge, 1997.
- [20] G. G. Batrouni, V. Rousseau, R. T. Scalettar, M. Rigol, A. Muramatsu, P. J. H. Denteneer, and M. Troyer. Mott domains of bosons confined on optical lattices. *Phys. Rev. Lett.*, 89(11):117203, Aug 2002.
- [21] H. Bender, P. Courteille, C. Zimmermann, and S. Slama. Appl. Phys. B, 96:275, 2009.
- [22] Silvia Bergamini, Benoît Darquié, Matthew Jones, Lionel Jacubowiez, Antoine Browaeys, and Philippe Grangier. Holographic generation of microtrap arrays for single atoms by use of a programmable phase modulator. *J. Opt. Soc. Am. B*, 21(11):1889–1894, November 2004.
- [23] Juliette Billy, Vincent Josse, Zhanchun Zuo, Alain Bernard, Ben Hambrecht, Pierre Lugan, David Clement, Laurent Sanchez-Palencia, Philippe Bouyer, and Alain Aspect. Direct observation of Anderson localization of matter waves in a controlled disorder. *Nature*, 453(7197):891–894, June 2008.

[24] K. Binder and A. P. Young. Spin glasses: Experimental facts, theoretical concepts, and open questions. *Rev. Mod. Phys.*, 58(4):801–976, Oct 1986.

- [25] G. Binnig, H. Rohrer, Ch. Gerber, and E. Weibel. Surface studies by scanning tunneling microscopy. *Phys. Rev. Lett.*, 49(1):57–61, Jul 1982.
- [26] D. Bitko, T. F. Rosenbaum, and G. Aeppli. Quantum critical behavior for a model magnet. Phys. Rev. Lett., 77(5):940–943, Jul 1996.
- [27] Immanuel Bloch, Jean Dalibard, and Wilhelm Zwerger. Many-body physics with ultracold gases. *Reviews of Modern Physics*, 80(3):885–964, July 2008.
- [28] N. Bogoliubov. On the theory of superfluidity. J. Phys., 11:23, 1947.
- [29] J. F. S. Brachmann, W. S. Bakr, J. Gillen, A. Peng, and M. Greiner. Inducing vortices in a Bose-Einstein condensate using holographically produced light beams. arXiv:1102.3373, 2011.
- [30] G. K. Brennen, C. M. Caves, P. S. Jessen, and I. H. Deutsch. Quantum logic gates in optical lattices. *Phys. Rev. Lett.*, 82(5):1060–1063, Feb 1999.
- [31] K. Brickman-Soderberg, N. Gemelke, and C. Chin. Ultracold molecules: vehicles to scalable quantum information processing. New J. Phys., 11:055022, 2009.
- [32] G. M. Bruun, O. F. Syljuåsen, K. G. L. Pedersen, B. M. Andersen, E. Demler, and A. S. Sørensen. Antiferromagnetic noise correlations in optical lattices. *Phys. Rev. A*, 80(3):033622, Sep 2009.
- [33] H. P. Büchler, E. Demler, M. Lukin, A. Micheli, N. Prokof'ev, G. Pupillo, and P. Zoller. Strongly correlated 2d quantum phases with cold polar molecules: Controlling the shape of the interaction potential. *Phys. Rev. Lett.*, 98(6):060404, Feb 2007.
- [34] Z. Cai, L. Wang, X. C. Xie, U. Schollwock, X. R. Wang, M. DiVentra, and Y. Wang. Quantum Spinon Oscillations. arXiv:1103.2400, 2011.
- [35] Gretchen K. Campbell, Jongchul Mun, Micah Boyd, Patrick Medley, Aaron E. Leanhardt, Luis G. Marcassa, David E. Pritchard, and Wolfgang Ketterle. Imaging the Mott Insulator Shells by Using Atomic Clock Shifts. *Science*, 313(5787):649–652, 2006.
- [36] B. Capogrosso-Sansone, Ş. G. Söyler, N. V. Prokof'ev, and B. V. Svistunov. Critical entropies for magnetic ordering in bosonic mixtures on a lattice. *Phys. Rev. A*, 81(5):053622, May 2010.

[37] Barbara Capogrosso-Sansone, Evgeny Kozik, Nikolay Prokof'ev, and Boris Svistunov. On-site number statistics of ultracold lattice bosons. *Phys. Rev. A*, 75(1):013619, Jan 2007.

- [38] Barbara Capogrosso-Sansone, Şebnem Güne ş Söyler, Nikolay Prokof'ev, and Boris Svistunov. Monte carlo study of the two-dimensional bose-hubbard model. *Phys. Rev. A*, 77(1):015602, Jan 2008.
- [39] K. A. Chao, J. Spałek, and A. M. Oleś. Canonical perturbation expansion of the hubbard model. *Phys. Rev. B*, 18(7):3453–3464, Oct 1978.
- [40] P. Cladé, C. Ryu, A. Ramanathan, K. Helmerson, and W. D. Phillips. Observation of a 2d bose gas: From thermal to quasicondensate to superfluid. *Phys. Rev. Lett.*, 102(17):170401, Apr 2009.
- [41] S. R. Clark and D. Jaksch. Dynamics of the superfluid to mott-insulator transition in one dimension. *Phys. Rev. A*, 70(4):043612, Oct 2004.
- [42] R. Coldea, D. A. Tennant, E. M. Wheeler, E. Wawrzynska, D. Prabhakaran, M. Telling, K. Habicht, P. Smeibidl, and K. Kiefer. Quantum Criticality in an Ising Chain: Experimental Evidence for Emergent E8 Symmetry. *Science*, 327(5962):177–180, January 2010.
- [43] T. A. Corcovilos, S. K. Baur, J. M. Hitchcock, E. J. Mueller, and R. G. Hulet. Detecting antiferromagnetism of atoms in an optical lattice via optical bragg scattering. *Phys. Rev. A*, 81(1):013415, Jan 2010.
- [44] M. Cramer, M. B. Plenio, and H. Wunderlich. Measuring entanglement in condensed matter systems. *Phys. Rev. Lett.*, 106(2):020401, Jan 2011.
- [45] P. A. Crowell, F. W. Van Keuls, and J. D. Reppy. Onset of superfluidity in <sup>4</sup>he films adsorbed on disordered substrates. Phys. Rev. B, 55(18):12620–12634, May 1997.
- [46] Fernando M. Cucchietti, Bogdan Damski, Jacek Dziarmaga, and Wojciech H. Zurek. Dynamics of the bose-hubbard model: Transition from a mott insulator to a superfluid. *Phys. Rev. A*, 75(2):023603, Feb 2007.
- [47] K. B. Davis, M. O. Mewes, M. R. Andrews, N. J. van Druten, D. S. Durfee, D. M. Kurn, and W. Ketterle. Bose-Einstein Condensation in a Gas of Sodium Atoms. *Physical Review Letters*, 75(22):3969–3973, November 1995.
- [48] Marshall T. DePue, Colin McCormick, S. Lukman Winoto, Steven Oliver, and David S. Weiss. Unity occupation of sites in a 3d optical lattice. *Phys. Rev. Lett.*, 82(11):2262–2265, Mar 1999.

[49] L. M. Duan, E. Demler, and M. D. Lukin. Controlling Spin Exchange Interactions of Ultracold Atoms in Optical Lattices. *Physical Review Letters*, 91(9):090402+, Aug 2003.

- [50] J. Dziarmaga. Dynamics of a quantum phase transition in the random ising model: Logarithmic dependence of the defect density on the transition rate. *Phys. Rev. B*, 74(6):064416, Aug 2006.
- [51] A. Einstein, B. Podolsky, and N. Rosen. Can quantum-mechanical description of physical reality be considered complete? *Phys. Rev.*, 47(10):777–780, May 1935.
- [52] Rolf Erni, Marta D. Rossell, Christian Kisielowski, and Ulrich Dahmen. Atomic-resolution imaging with a sub-50-pm electron probe. *Phys. Rev. Lett.*, 102(9):096101, Mar 2009.
- [53] Tilman Esslinger, Immanuel Bloch, and Theodor W. Hänsch. Bose-einstein condensation in a quadrupole-ioffe-configuration trap. *Phys. Rev. A*, 58(4):R2664–R2667, Oct 1998.
- [54] L. Fallani, J. E. Lye, V. Guarrera, C. Fort, and M. Inguscio. Ultracold atoms in a disordered crystal of light: Towards a bose glass. *Phys. Rev. Lett.*, 98(13):130404, Mar 2007.
- [55] Richard Feynman. Simulating physics with computers. *International Journal of Theoretical Physics*, 21(6):467–488, June 1982.
- [56] Matthew P. A. Fisher, Peter B. Weichman, G. Grinstein, and Daniel S. Fisher. Boson localization and the superfluid-insulator transition. *Physical Review B*, 40(1):546–570, Jul 1989.
- [57] S. Foelling. Ph.D. thesis, Universitat Innsbruck, 2006.
- [58] S. Foelling. Probing strongly correlated states of ultracold atoms in optical lattices. *PhD Thesis, Johannes-Gutenberg-Universitat Mainz*, 2008.
- [59] S. Fölling, S. Trotzky, P. Cheinet, M. Feld, R. Saers, A. Widera, T. Müller, and I. Bloch. Direct observation of second-order atom tunnelling. *Nature*, 448(7157):1029–1032, August 2007.
- [60] Simon Folling, Fabrice Gerbier, Artur Widera, Olaf Mandel, Tatjana Gericke, and Immanuel Bloch. Spatial quantum noise interferometry in expanding ultracold atom clouds. *Nature*, 434(7032):481–484, March 2005.

[61] Simon Fölling, Artur Widera, Torben Müller, Fabrice Gerbier, and Immanuel Bloch. Formation of spatial shell structure in the superfluid to mott insulator transition. *Phys. Rev. Lett.*, 97(6):060403, Aug 2006.

- [62] Alpha Gaetan, Yevhen Miroshnychenko, Tatjana Wilk, Amodsen Chotia, Matthieu Viteau, Daniel Comparat, Pierre Pillet, Antoine Browaeys, and Philippe Grangier. Observation of collective excitation of two individual atoms in the Rydberg blockade regime. *Nature Physics*, 5(2):115–118, January 2009.
- [63] J. J. García-Ripoll, M. A. Martin-Delgado, and J. I. Cirac. Implementation of spin hamiltonians in optical lattices. *Phys. Rev. Lett.*, 93(25):250405, Dec 2004.
- [64] L. J. Geerligs, M. Peters, L. E. M. de Groot, A. Verbruggen, and J. E. Mooij. Charging effects and quantum coherence in regular josephson junction arrays. *Phys. Rev. Lett.*, 63(3):326–329, Jul 1989.
- [65] N. Gemelke, E. Sarajlic, and S. Chu. Rotating Few-body Atomic Systems in the Fractional Quantum Hall Regime. arXiv:1007.2677, 2010.
- [66] Nathan Gemelke, Xibo Zhang, Chen-Lung Hung, and Cheng Chin. In-situ observation of incompressible Mott-insulating domains in ultracold atomic gases. Nature, 460(7258):995–998, August 2009.
- [67] Fabrice Gerbier. Boson Mott Insulators at Finite Temperatures. *Physical Review Letters*, 99(12):120405+, Sep 2007.
- [68] Fabrice Gerbier and Yvan Castin. Heating rates for an atom in a far-detuned optical lattice. *Phys. Rev. A*, 82(1):013615, Jul 2010.
- [69] Fabrice Gerbier, Simon Fölling, Artur Widera, Olaf Mandel, and Immanuel Bloch. Probing number squeezing of ultracold atoms across the superfluid-mott insulator transition. *Phys. Rev. Lett.*, 96(9):090401, Mar 2006.
- [70] Fabrice Gerbier, Artur Widera, Simon Fölling, Olaf Mandel, Tatjana Gericke, and Immanuel Bloch. Phase coherence of an atomic mott insulator. *Phys. Rev. Lett.*, 95(5):050404, Jul 2005.
- [71] Tatjana Gericke, Peter Wurtz, Daniel Reitz, Tim Langen, and Herwig Ott. High-resolution scanning electron microscopy of an ultracold quantum gas. *Nat Phys*, 4(12):949–953, December 2008.
- [72] J. I. Gillen. Ph.D. thesis, Harvard University, 2009.
- [73] J. I. Gillen, W. S. Bakr, A. Peng, P. Unterwaditzer, S. Fölling, and M. Greiner. Two-dimensional quantum gas in a hybrid surface trap. *Phys. Rev. A*, 80(2):021602, Aug 2009.

[74] Roy J. Glauber. Coherent and incoherent states of the radiation field. *Phys. Rev.*, 131(6):2766–2788, Sep 1963.

- [75] A. Görlitz, J. M. Vogels, A. E. Leanhardt, C. Raman, T. L. Gustavson, J. R. Abo-Shaeer, A. P. Chikkatur, S. Gupta, S. Inouye, T. Rosenband, and W. Ketterle. Realization of bose-einstein condensates in lower dimensions. *Phys. Rev. Lett.*, 87(13):130402, Sep 2001.
- [76] M. Greiner, C. A. Regal, J. T. Stewart, and D. S. Jin. Probing pair-correlated fermionic atoms through correlations in atom shot noise. *Phys. Rev. Lett.*, 94(11):110401, Mar 2005.
- [77] Markus Greiner, Immanuel Bloch, Theodor W. Hänsch, and Tilman Esslinger. Magnetic transport of trapped cold atoms over a large distance. *Phys. Rev. A*, 63(3):031401, Feb 2001.
- [78] Markus Greiner, Olaf Mandel, Tilman Esslinger, Theodor W. Hänsch, and Immanuel Bloch. Quantum phase transition from a superfluid to a Mott insulator in a gas of ultracold atoms. *Nature*, 415(6867):39–44, January 2002.
- [79] Markus Greiner, Olaf Mandel, Theodor W. Hänsch, and Immanuel Bloch. Collapse and revival of the matter wave field of a Bose—[ndash]—Einstein condensate. *Nature*, 419(6902):51–54, September 2002.
- [80] David G. Grier. A revolution in optical manipulation. *Nature*, 424(6950):810–816, August 2003.
- [81] S. A. Grigera, R. S. Perry, A. J. Schofield, M. Chiao, S. R. Julian, G. G. Lonzarich, S. I. Ikeda, Y. Maeno, A. J. Millis, and A. P. Mackenzie. Magnetic field-tuned quantum criticality in the metallic ruthenate sr3ru2o7. *Science*, 294(5541):329–332, 2001.
- [82] R. Grimm, M. Weidemller, and Y. B. Ovchinnikov. Adv. At. Mol., Opt. Phys., 42:95, 2000.
- [83] Zoran Hadzibabic, Peter Kruger, Marc Cheneau, Baptiste Battelier, and Jean Dalibard. BerezinskiiKosterlitzThouless crossover in a trapped atomic gas. *Nature*, 441(7097):1118–1121, June 2006.
- [84] Elmar Haller, Russell Hart, Manfred J. Mark, Johann G. Danzl, Lukas Reichsollner, Mattias Gustavsson, Marcello Dalmonte, Guido Pupillo, and Hanns-Christoph Nagerl. Pinning quantum phase transition for a Luttinger liquid of strongly interacting bosons. *Nature*, 466(7306):597–600, July 2010.

[85] M. Hammes, D. Rychtarik, B. Engeser, H.-C. Nägerl, and R. Grimm. Evanescent-wave trapping and evaporative cooling of an atomic gas at the crossover to two dimensions. *Phys. Rev. Lett.*, 90(17):173001, Apr 2003.

- [86] M. Hammes, D. Rychtarik, H.-C. Nägerl, and R. Grimm. Cold-atom gas at very high densities in an optical surface microtrap. *Phys. Rev. A*, 66(5):051401, Nov 2002.
- [87] Rolf Heidemann, Ulrich Raitzsch, Vera Bendkowsky, Björn Butscher, Robert Löw, Luis Santos, and Tilman Pfau. Evidence for Coherent Collective Rydberg Excitation in the Strong Blockade Regime. *Physical Review Letters*, 99(16):163601+, Oct 2007.
- [88] A. Hewson. The Kondo problem to heavy fermions. Cambridge University Press, 1993.
- [89] J. Hubbard. Electron Correlations in Narrow Energy Bands. *Proceedings of the Royal Society of London. Series A. Mathematical and Physical Sciences*, 276(1365):238–257, November 1963.
- [90] S. D. Huber, B. Theiler, E. Altman, and G. Blatter. Amplitude mode in the quantum phase model. *Phys. Rev. Lett.*, 100(5):050404, Feb 2008.
- [91] Chen-Lung Hung, Xibo Zhang, Nathan Gemelke, and Cheng Chin. Slow mass transport and statistical evolution of an atomic gas across the superfluid–mottinsulator transition. *Phys. Rev. Lett.*, 104(16):160403, Apr 2010.
- [92] Y. Imry and S.-k. Ma. Random-field instability of the ordered state of continuous symmetry. *Phys. Rev. Lett.*, 35(21):1399–1401, Nov 1975.
- [93] S. Inouye, M. R. Andrews, J. Stenger, H. J. Miesner, D. M. Stamper-Kurn, and W. Ketterle. Observation of Feshbach resonances in a BoseEinstein condensate. *Nature*, 392(6672):151–154, March 1998.
- [94] R. Islam, E. E. Edwards, K. Kim, S. Korenblit, C. Noh, H. Carmichael, G.-D. Lin, L.-M. Duan, C.-C. Joseph Wang, J. K. Freericks, and C. Monroe. Onset of a Quantum Phase Transition with a Trapped Ion Quantum Simulator. arXiv:1103.2400, 2011.
- [95] A. Itah, H. Veksler, O. Lahav, A. Blumkin, C. Moreno, C. Gordon, and J. Steinhauer. Direct observation of a sub-poissonian number distribution of atoms in an optical lattice. *Phys. Rev. Lett.*, 104(11):113001, Mar 2010.
- [96] D. Jaksch. Ph.D. thesis, Leopold-Franzens-Universitat Innsbruck, Austria, 1999.

[97] D. Jaksch, C. Bruder, J. I. Cirac, C. W. Gardiner, and P. Zoller. Cold Bosonic Atoms in Optical Lattices. *Physical Review Letters*, 81(15):3108–3111, Oct 1998.

- [98] D. Jaksch and P. Zoller. The cold atom Hubbard toolbox. *Annals of Physics*, 315(1):52–79, January 2005.
- [99] G.-B. Jo, Y.-R. Lee, J.-H. Choi, C. A. Christensen, T. H. Kim, J. H. Thywissen, D. E. Pritchard, and W. Ketterle. Itinerant Ferromagnetism in a Fermi Gas of Ultracold Atoms. *Science*, 325(5947):1521–1524, 2009.
- [100] P. R. Johnson, E. Tiesinga, J. V. Porto, and C. J. Williams. Effective three-body interactions of neutral bosons in optical lattices. New Journal of Physics, 11(9):093022+, September 2009.
- [101] Robert Jordens, Niels Strohmaier, Kenneth Gunter, Henning Moritz, and Tilman Esslinger. A Mott insulator of fermionic atoms in an optical lattice. Nature, 455(7210):204–207, September 2008.
- [102] M. Karski, L. Förster, J. M. Choi, W. Alt, A. Widera, and D. Meschede. Nearest-Neighbor Detection of Atoms in a 1D Optical Lattice by Fluorescence Imaging. Feb 2009.
- [103] K. Kim, M. S. Chang, S. Korenblit, R. Islam, E. E. Edwards, J. K. Freericks, G. D. Lin, L. M. Duan, and C. Monroe. Quantum simulation of frustrated Ising spins with trapped ions. *Nature*, 465(7298):590–593, June 2010.
- [104] Toshiya Kinoshita, Trevor Wenger, and David S. Weiss. Observation of a One-Dimensional Tonks-Girardeau Gas. *Science*, 305(5687):1125–1128, August 2004.
- [105] A. Kitaev. Anyons in an exactly solved model and beyond. *Annals of Physics*, 321(1):2–111, January 2006.
- [106] C. Kittel. Quantum Theory of Solids. John Wiley and Sons, New York, 1963.
- [107] M. Köhl, H. Moritz, T. Stöferle, C. Schori, and T. Esslinger. Superfluid to Mott insulator transition in one, two, and three dimensions. *Journal of Low Temperature Physics*, 138(3):635–644, February 2005.
- [108] C. Kollath, U. Schollwöck, J. von Delft, and W. Zwerger. Spatial correlations of trapped one-dimensional bosons in an optical lattice. *Phys. Rev. A*, 69(3):031601, Mar 2004.

[109] Corinna Kollath, Andreas M. Läuchli, and Ehud Altman. Quench dynamics and nonequilibrium phase diagram of the bose-hubbard model. *Phys. Rev. Lett.*, 98(18):180601, Apr 2007.

- [110] J. M. Kosterlitz and D. J. Thouless. Ordering, metastability and phase transitions in two-dimensional systems. *Journal of Physics C: Solid State Physics*, 6(7):1181–1203, 1973.
- [111] H. A. Kramers. L'interaction entre les atomes magntognes dans un cristal paramagntique. *Physica*, 1(1-6):182 192, 1934.
- [112] Werner Krauth, Michel Caffarel, and Jean-Philippe Bouchaud. Gutzwiller wave function for a model of strongly interacting bosons. *Phys. Rev. B*, 45(6):3137–3140, Feb 1992.
- [113] A. Landragin, G. Labeyrie, C. Henkel, R. Kaiser, N. Vansteenkiste, C. I. Westbrook, and A. Aspect. Specular versus diffuse reflection of atoms from an evanescent-wave mirror. *Opt. Lett.*, 21:1591, 1996.
- [114] K. M. Lang. Imaging the granular structure of high-T\$\_c\$ superconductivity in underdoped \$Bi\_2Sr\_2CaCu\_2O\_8+ delta\$. Nature, bf 415(6870):412-416, January 2002.
- [115] R. B. Laughlin. Anomalous quantum hall effect: An incompressible quantum fluid with fractionally charged excitations. *Phys. Rev. Lett.*, 50(18):1395–1398, May 1983.
- [116] P. J. Lee, M. Anderlini, B. L. Brown, J. Sebby Strabley, W. D. Phillips, and J. V. Porto. Sublattice Addressing and Spin-Dependent Motion of Atoms in a Double-Well Lattice. *Physical Review Letters*, 99(2):020402+, Jul 2007.
- [117] Patrick A. Lee, Naoto Nagaosa, and Xiao-Gang Wen. Doping a mott insulator: Physics of high-temperature superconductivity. *Rev. Mod. Phys.*, 78(1):17–85, Jan 2006.
- [118] D. Leibfried, E. Knill, S. Seidelin, J. Britton, R. B. Blakestad, J. Chiaverini, D. B. Hume, W. M. Itano, J. D. Jost, C. Langer, R. Ozeri, R. Reichle, and D. J. Wineland. Creation of a six-atom 'Schrödinger cat' state. *Nature*, 438(7068):639–642, December 2005.
- [119] Maciej Lewenstein, Anna Sanpera, Veronica Ahufinger, Bogdan Damski, Aditi Sen, and Ujjwal Sen. Ultracold atomic gases in optical lattices: mimicking condensed matter physics and beyond. *Advances in Physics*, 56(2):243–379, 2007.

[120] J. Liang, J. Kohn, M. F. Becker, and D. J. Heinzen. 1.5% root-mean-square flat-intensity laser beam formed using a binary-amplitude spatial light modulator. *Appl. Opt.*, 48:1955, 2009.

- [121] E. M. Lifshitz and L. P. Pitaevskii. Course of Theoretical Physics, Volume IX: Statistical Physics (Part 2). Butterworth-Heinemann, January 1980.
- [122] E. M. Lifshitz and L. P. Pitaevskii. Statistical Physics. Pergamon Press, Oxford, 1980.
- [123] M. D. Lukin, M. Fleischhauer, R. Cote, L. M. Duan, D. Jaksch, J. I. Cirac, and P. Zoller. Dipole Blockade and Quantum Information Processing in Mesoscopic Atomic Ensembles. *Physical Review Letters*, 87(3):037901+, Jun 2001.
- [124] L. Mandel and E. Wolf. *Optical coherence and quantum optics*. Cambridge University Press, 1995.
- [125] Olaf Mandel, Markus Greiner, Artur Widera, Tim Rom, Theodor W. Hansch, and Immanuel Bloch. Controlled collisions for multi-particle entanglement of optically trapped atoms. *Nature*, 425(6961):937–940, October 2003.
- [126] S. M. Mansfield and G. S. Kino. Solid immersion microscope. *Applied Physics Letters*, 57(24):2615–2616, 1990.
- [127] J. M. McGuirk, D. M. Harber, J. M. Obrecht, and E. A. Cornell. Alkali-metal adsorbate polarization on conducting and insulating surfaces probed with bose-einstein condensates. *Phys. Rev. A*, 69(6):062905, Jun 2004.
- [128] D. McKay and B. DeMarco. Cooling in strongly correlated optical lattices: prospects and challenges. arxiv:1010.0198, 2010.
- [129] P. Medley, D. Weld, H. Miyake, D. E. Pritchard, and W. Ketterle. Spin Gradient Demagnetization Cooling of Ultracold Atoms. arxiv:1006.4674, 2010.
- [130] H. Metcalf and P. van der Straten. Laser Cooling and Trapping. Springer, New York, 1999.
- [131] Karl D. Nelson, Xiao Li, and David S. Weiss. Imaging single atoms in a three-dimensional array. *Nat Phys*, 3(8):556–560, 2007.
- [132] R. Newell, J. Sebby, and T. G. Walker. Dense atom clouds in a holographic atom trap. *Opt. Lett.*, 28(14):1266–1268, July 2003.
- [133] K. K. Ni, S. Ospelkaus, M. H. G. de Miranda, A. Pe'er, B. Neyenhuis, J. J. Zirbel, S. Kotochigova, P. S. Julienne, D. S. Jin, and J. Ye. A High Phase-Space-Density Gas of Polar Molecules. *Science*, 322(5899):231–235, October 2008.

[134] K.-K. Ni, S. Ospelkaus, D. Wang, G. Quemener, B. Neyenhuis, M. H. G. de Miranda, J. L. Bohn, J. Ye, and D. S. Jin. Dipolar collisions of polar molecules in the quantum regime. *Nature*, 464:1324–1328, 2010.

- [135] M. A. Novotny and D. P. Landau. Zero temperature phase diagram for the d=1 quantum Ising antiferromagnet. J. Mag. and Mag. Mat., 54:685–686, 1986.
- [136] J. M. Obrecht, R. J. Wild, and E. A. Cornell. Measuring electric fields from surface contaminants with neutral atoms. *Phys. Rev. A*, 75(6):062903, Jun 2007.
- [137] A. A. Ovchinnikov, D. V. Dmitriev, V. Ya. Krivnov, and V. O. Cheranovskii. Antiferromagnetic ising chain in a mixed transverse and longitudinal magnetic field. *Phys. Rev. B*, 68(21):214406, Dec 2003.
- [138] Yu. B. Ovchinnikov, I. Manek, and R. Grimm. Surface trap for cs atoms based on evanescent-wave cooling. *Phys. Rev. Lett.*, 79(12):2225–2228, Sep 1997.
- [139] Belen Paredes, Artur Widera, Valentin Murg, Olaf Mandel, Simon Folling, Ignacio Cirac, Gora V. Shlyapnikov, Theodor W. Hansch, and Immanuel Bloch. Tonks—[ndash]—Girardeau gas of ultracold atoms in an optical lattice. *Nature*, 429(6989):277–281, May 2004.
- [140] A. L. Patterson. The scherrer formula for x-ray particle size determination. *Phys. Rev.*, 56(10):978–982, Nov 1939.
- [141] A. Peng. Ph.D. thesis, Harvard University, 2010.
- [142] C. Pethick and H. Smith. *Bose-Einstein condensation in dilute gases*. Cambridge University Press, 2002.
- [143] D. S. Petrov, M. Holzmann, and G. V. Shlyapnikov. Bose-einstein condensation in quasi-2d trapped gases. *Phys. Rev. Lett.*, 84(12):2551–2555, Mar 2000.
- [144] H. Pichler, A. J. Daley, and P. Zoller. Nonequilibrium dynamics of bosonic atoms in optical lattices: Decoherence of many-body states due to spontaneous emission. *Phys. Rev. A*, 82(6):063605, Dec 2010.
- [145] S. Pielawa, T. Kitagawa, E. Berg, and S. Sachdev. Correlated phases of bosons in tilted, frustrated lattices. arxiv:1101.2897, 2010.
- [146] P. W. H. Pinkse, A. Mosk, M. Weidemüller, M. W. Reynolds, T. W. Hijmans, and J. T. M. Walraven. Adiabatically changing the phase-space density of a trapped bose gas. *Phys. Rev. Lett.*, 78(6):990–993, Feb 1997.

[147] P. Plotz, P. Schlagheck, and S. Wimberger. Effective spin model for interband transport in a wannier-stark lattice system. *The European Physical Journal D - Atomic, Molecular, Optical and Plasma Physics*, pages 1–7, 2010. 10.1140/epjd/e2010-10554-7.

- [148] L. Pollet, C. Kollath, K. Van Houcke, and M. Troyer. Temperature changes when adiabatically ramping up an optical lattice. N. J. Phys., 10:065001, 2008.
- [149] Lode Pollet, Kris V. Houcke, and Stefan M. Rombouts. Engineering local optimality in quantum Monte Carlo algorithms. *Journal of Computational Physics*, 225(2):2249–2266, August 2007.
- [150] M. Popp, J.-J. Garcia-Ripoll, K. G. Vollbrecht, and J. I. Cirac. Ground-state cooling of atoms in optical lattices. *Phys. Rev. A*, 74(1):013622, Jul 2006.
- [151] N. V. Prokof'ev, B. V. Svistunov, and I. S. Tupitsyn. Worm algorithm in quantum monte carlo simulations. *Physics Letters A*, 238(4-5):253–257, 1998.
- [152] A. Ramirez. Colossal magnetoresistance. J. Phys: Condens. Matter, 9(39):8171, 1997.
- [153] Robert Raussendorf and Hans J. Briegel. A One-Way Quantum Computer. Physical Review Letters, 86(22):5188–5191, May 2001.
- [154] M. Rigol, A. Muramatsu, G. G. Batrouni, and R. T. Scalettar. Local quantum criticality in confined fermions on optical lattices. *Phys. Rev. Lett.*, 91(13):130403, Sep 2003.
- [155] Marcos Rigol and Alejandro Muramatsu. Quantum monte carlo study of confined fermions in one-dimensional optical lattices. Phys. Rev. A, 69(5):053612, May 2004.
- [156] Daniel S. Rokhsar and B. G. Kotliar. Gutzwiller projection for bosons. *Phys. Rev. B*, 44(18):10328–10332, Nov 1991.
- [157] T. Rom, Th Best, D. van Oosten, U. Schneider, S. Folling, B. Paredes, and I. Bloch. Free fermion antibunching in a degenerate atomic Fermi gas released from an optical lattice. *Nature*, 444(7120):733–736, December 2006.
- [158] Ch. Rüegg, A. Furrer, D. Sheptyakov, Th. Strässle, K. W. Krämer, H.-U. Güdel, and L. Mélési. Pressure-induced quantum phase transition in the spin-liquid *tlcucl*<sub>3</sub>. *Phys. Rev. Lett.*, 93(25):257201, Dec 2004.
- [159] D. Rychtarik, B. Engeser, H.-C. Nägerl, and R. Grimm. Two-dimensional boseeinstein condensate in an optical surface trap. *Phys. Rev. Lett.*, 92(17):173003, Apr 2004.

- [160] S. Sachdev and B. Keimer. Quantum criticality. *Physics Today*, 2011.
- [161] Subir Sachdev. *Quantum Phase Transitions*. Cambridge University Press, new edition edition, April 2001.
- [162] Subir Sachdev. Quantum magnetism and criticality. *Nature Physics*, 4(3):173–185, March 2008.
- [163] Subir Sachdev, K. Sengupta, and S. M. Girvin. Mott insulators in strong electric fields. *Phys. Rev. B*, 66(7):075128, Aug 2002.
- [164] M. Saffman, T. G. Walker, and K. Mølmer. Quantum information with rydberg atoms. Rev. Mod. Phys., 82(3):2313–2363, Aug 2010.
- [165] U. Schneider, L. Hackermuller, S. Will, Th Best, I. Bloch, T. A. Costi, R. W. Helmes, D. Rasch, and A. Rosch. Metallic and Insulating Phases of Repulsively Interacting Fermions in a 3D Optical Lattice. *Science*, 322(5907):1520–1525, December 2008.
- [166] Christian Schori, Thilo Stöferle, Henning Moritz, Michael Köhl, and Tilman Esslinger. Excitations of a superfluid in a three-dimensional optical lattice. *Phys. Rev. Lett.*, 93(24):240402, Dec 2004.
- [167] V. Schweikhard, I. Coddington, P. Engels, V. P. Mogendorff, and E. A. Cornell. Rapidly rotating bose-einstein condensates in and near the lowest landau level. *Phys. Rev. Lett.*, 92(4):040404, Jan 2004.
- [168] V. Schweikhard, S. Tung, and E. A. Cornell. Vortex proliferation in the berezinskii-kosterlitz-thouless regime on a two-dimensional lattice of bose-einstein condensates. *Phys. Rev. Lett.*, 99(3):030401, Jul 2007.
- [169] Rajdeep Sensarma, David Pekker, Mikhail D. Lukin, and Eugene Demler. Modulation spectroscopy and dynamics of double occupancies in a fermionic mott insulator. *Phys. Rev. Lett.*, 103(3):035303, Jul 2009.
- [170] Jacob F. Sherson, Christof Weitenberg, Manuel Endres, Marc Cheneau, Immanuel Bloch, and Stefan Kuhr. Single-atom-resolved fluorescence imaging of an atomic Mott insulator. *Nature*, 467(7311):68–72, August 2010.
- [171] K. Sheshadri, H. R. Krishnamurthy, R. Pandit, and T. V. Ramakrishnan. Superfluid and insulating phases in an interacting-boson model: Mean-field theory and the rpa. *Europhys. Lett.*, 2:257, 1993.
- [172] M. Shotter. Large photon number extraction from individual atoms trapped in an optical lattice. arXiv:1011.5426, 2010.

[173] Qimiao Si and Frank Steglich. Heavy Fermions and Quantum Phase Transitions. *Science*, 329(5996):1161–1166, September 2010.

- [174] N. L. Smith, W. H. Heathcote, G. Hechenblaikner, E. Nugent, and C. J. Foot. Quasi-2d confinement of a bec in a combined optical and magnetic potential. J. Phys. B: At. Mol. Opt. Phys., 38:223, 2005.
- [175] P. Soltan-Panahi, J. Struck, P. Hauke, A. Bick, W. Plenkers, G. Meineke, C. Becker, P. Windpassinger, M. Lewenstein, and K. Sengstock. Multi-Component Quantum Gases in Spin-Dependent Hexagonal Lattices. arXiv:1005.1276, 2010.
- [176] Anders S. Sørensen, Ehud Altman, Michael Gullans, J. V. Porto, Mikhail D. Lukin, and Eugene Demler. Adiabatic preparation of many-body states in optical lattices. *Phys. Rev. A*, 81(6):061603, Jun 2010.
- [177] Anders S. Sørensen, Eugene Demler, and Mikhail D. Lukin. Fractional quantum hall states of atoms in optical lattices. *Phys. Rev. Lett.*, 94(8):086803, Mar 2005.
- [178] A. S. Sorenson. Time dependent mean field (and slightly beyond) for the superfluid to mott insulator transition. *private communication*.
- [179] I. B. Spielman, W. D. Phillips, and J. V. Porto. Mott-insulator transition in a two-dimensional atomic bose gas. *Phys. Rev. Lett.*, 98(8):080404, Feb 2007.
- [180] D. M. Stamper-Kurn, H.-J. Miesner, A. P. Chikkatur, S. Inouye, J. Stenger, and W. Ketterle. Reversible formation of a bose-einstein condensate. *Phys. Rev. Lett.*, 81(11):2194–2197, Sep 1998.
- [181] Sabine Stock, Zoran Hadzibabic, Baptiste Battelier, Marc Cheneau, and Jean Dalibard. Observation of phase defects in quasi-two-dimensional bose-einstein condensates. *Phys. Rev. Lett.*, 95(19):190403, Nov 2005.
- [182] H. L. Stormer. Nobel lecture: The fractional quantum hall effect. Rev. Mod. Phys., 71(4):875–889, Jul 1999.
- [183] S. Trotzky, P. Cheinet, S. Fölling, M. Feld, U. Schnorrberger, A. M. Rey, A. Polkovnikov, E. A. Demler, M. D. Lukin, and I. Bloch. Time-Resolved Observation and Control of Superexchange Interactions with Ultracold Atoms in Optical Lattices. *Science*, 319(5861):295–299, January 2008.
- [184] S. Trotzky, L. Pollet, F. Gerbier, U. Schnorrberger, I. Bloch, N. V. Prokof'ev, B. Svistunov, and M. Troyer. Suppression of the critical temperature for superfluidity near the Mott transition. *Nature Physics*, 6:998–1004, October 2010.

[185] E. Urban, T. A. Johnson, T. Henage, L. Isenhower, D. D. Yavuz, T. G. Walker, and M. Saffman. Observation of Rydberg blockade between two atoms. *Nature Physics*, 5(2):110–114, January 2009.

- [186] G. Vidal, J. I. Latorre, E. Rico, and A. Kitaev. Entanglement in Quantum Critical Phenomena. *Physical Review Letters*, 90(22):227902+, Jun 2003.
- [187] Hendrik Weimer, Markus Muller, Igor Lesanovsky, Peter Zoller, and Hans P. Buchler. A Rydberg quantum simulator. *Nature Physics*, 6(5):382–388, March 2010.
- [188] C. Weitenberg, M. Endres, J. F. Sherson, M. Cheneau, P. Schaub, T. Fukuhara, I. Bloch, and S. Kuhr. Single-Spin Addressing in an Atomic Mott Insulator. arXiv:1101.2076, 2011.
- [189] David M. Weld, Patrick Medley, Hirokazu Miyake, David Hucul, David E. Pritchard, and Wolfgang Ketterle. Spin Gradient Thermometry for Ultracold Atoms in Optical Lattices. *Physical Review Letters*, 103(24):245301+, Dec 2009.
- [190] Artur Widera, Fabrice Gerbier, Simon Fölling, Tatjana Gericke, Olaf Mandel, and Immanuel Bloch. Coherent collisional spin dynamics in optical lattices. *Phys. Rev. Lett.*, 95(19):190405, Nov 2005.
- [191] S. Will, T. Best, U. Schneider, L. Hackermueller, D. Luhmann, and I. Bloch. Time-resolved observation of coherent multi-body interactions in quantum phase revivals. *Nature*, 465(7295):197–201, 2010.
- [192] Kenneth G. Wilson. The renormalization group: Critical phenomena and the kondo problem. *Rev. Mod. Phys.*, 47(4):773–840, Oct 1975.
- [193] D. J. Wineland, J. Dalibard, and C. Cohen-Tannoudji. Sisyphus cooling of a bound atom. J. Opt. Soc. Am. B, 9:32–42, 1992.
- [194] S. Lukman Winoto, Marshall T. DePue, Nathan E. Bramall, and David S. Weiss. Laser cooling at high density in deep far-detuned optical lattices. *Phys. Rev. A*, 59(1):R19–R22, Jan 1999.
- [195] Peter Würtz, Tim Langen, Tatjana Gericke, Andreas Koglbauer, and Herwig Ott. Experimental demonstration of single-site addressability in a two-dimensional optical lattice. *Phys. Rev. Lett.*, 103(8):080404, Aug 2009.
- [196] K. Yamada. Electron correlation in metals. Cambridge University Press, 2004.
- [197] X. Zhang, C.-L. Hung, S.-K. Tung, N. Gemelke, and C. Chin. Exploring quantum criticality based on ultracold atoms in optical lattices. arXiv:1101.0284, 2010.

[198] X. Zhuang, L. E. Bartley, H. P. Babcock, R. Russell, T. Ha, D. Herschlag, and S. Chu. A single-molecule study of RNA catalysis and folding. *Science*, 288(5473):2048–2051, June 2000.

## Appendix A

## Beyond hyperfine encoding of spins

The proposal of Ref. [49] generated a lot of interest in the optical lattice community by providing a path for the realization of localized spin Hamiltonians using cold atoms. The starting point of this proposal is a Mott insulator with one atom per lattice site, and the spins are encoded in the internal hyperfine state of the atoms. The spins interact through superexchange with a characteristic energy scale  $t^2/U$ . In rubidium, where the scattering lengths for interactions of atoms in the hyperfine ground states are all approximately equal, the magnetic model realized is a ferromagnetic Heisenberg model. It is difficult to study quantum magnetism in this model because most easily constructed additional terms in the Hamiltonian, e.g.  $S_x^i$ , commute with  $\vec{S}^i \cdot \vec{S}^j$ . Introducing anisotropy into rubidium's Heisenberg model can be achieved with spin-dependent lattices, but heating rates in such lattice are rather high, making this path incompatible with the low temperatures required for superexchange ordering. The encoding of the spins in an external degree freedom in Chapter 6 allowed simulating an Ising spin Hamiltonian instead, and achieving interactions at

a much higher energy scale. In this appendix, we describe other ideas we have considered to simulate anisotropic quantum Heisenberg models in magnetic fields using external atomic degrees of freedom.

## A.1 Double well ladder systems

The system we consider is a one-dimensional chain of double-wells shown in Figure A.1(a). We study the case where there is only one atom in each double-well and define a quantum spin-1/2 on each double-well by the position of the atom: an up (down) spin is represented by the atom on the left (right) side of the double-well. The tunneling matrix element  $t_{DW}$  of an atom in the double-well system, controlled by the barrier height, maps to an effective transverse field that allows spin flips, contributing a term to the Hamiltonian of the form  $-h\sum_i S_x^i$  with  $h=2t_{DW}$ .

We work in a regime where the tunneling along the chain,  $t_C$  is weak; we shall precisely define what this means shortly. In addition, a potential gradient with strength  $\Delta$  between neighbouring sites is applied along the chain. Because the tunneling is weak, atoms remain localized in their double-wells, and only explore neighbouring sites in the chain virtually in second-order processes, where an atom hops to a neighbouring site and back to lower its energy. This gives rise to a superexchange interaction between neighbouring spins. The resulting energy shifts for pairs of neighbouring spins in different states can be deduced using second order perturbation theory from the diagrams shown in Figure A.1(b-c), and are given by  $\Delta E_{\uparrow\uparrow} = \Delta E_{\downarrow\downarrow} = -4t_C^2 U/(U^2 - \Delta^2)$  and  $\Delta E_{\uparrow\downarrow} = \Delta E_{\downarrow\uparrow} = 0$ . The validity of the perturbation theory requires  $t_C \ll |\Delta|, |U - \Delta|$ , which can achieved for example by

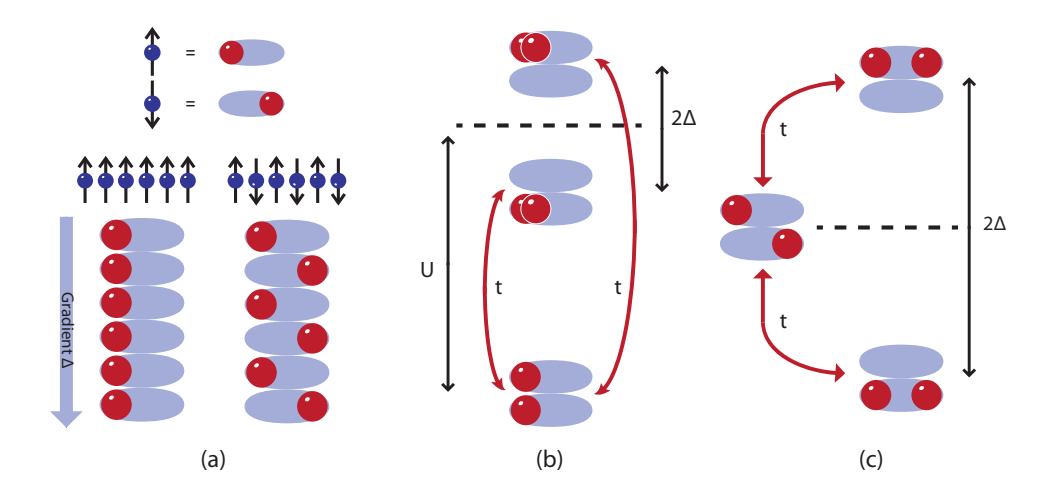


Figure A.1: Realization of transverse Ising model in a ladder system. (a) Top: mapping of location in the double well to a spin-1/2. Bottom: Ferromagnetic (left) and antiferromagnetic (right) states. (b) Energy level diagram for calculating superexchange energy shift for two neighbouring up spins, and (c) and for neighbouring up and down spins.

picking  $\Delta = U/2$  and  $t \ll U$ . The total resulting Hamiltonian is that of an Ising chain in a transverse field:

$$H = \sum_{i} -JS_{z}^{i}S_{z}^{i+1} - hS_{x}^{i}$$
 (A.1)

with  $J = 8t_C^2 U / (U^2 - \Delta^2)$ .

This system has two advantages compared to a one-dimensional version of the model proposed in Ref. [49]. First, the spin detection is already possible with our quantum gas microscope because it is based on the location of the atoms rather than the internal state. Second, the sign of the spin-spin coupling can be varied between ferromagnetic and antiferromagnetic interactions by appropriately choosing  $\Delta$ . The two ground states are shown in Figure A.1(a). The quantum phase transition can be

studied by starting with a large transverse field obtained with a low barrier within the double-wells, which is increased gradually to make the spin-spin coupling dominate, leading to (anti-)ferromagnetic states with spontaneously broken symmetry.

Finally, we describe how such a system can be experimentally prepared. The starting point is a Mott insulator of rubidium atoms in the  $|F = 1, m_F = -1\rangle$  in our 2D lattice. A holographically projected superlattice along one dimension is used to decouple the system into an ensemble of ladder systems. Using the techniques described in [183] involving spin-changing collisions, each double-well can be prepared to have an atom in  $|F = 1, m_F = -1\rangle$  on one side and  $|F = 1, m_F = +1\rangle$  on the other, and one of these states can be subsequently be removed by microwave transfer to  $|F = 2\rangle$ , followed by a resonant light pulse. We start with a magnetic gradient along the chain and negligible  $t_C$ . At this point, the system has been initialized with atoms with all pseudospins pointing up. To prepare an eigenstate of  $-h \sum S_x^i$ , a gradient along the double-well axis is applied,  $t_{DW}$  is increased from zero to a finite value and finally the gradient is adiabatically lowered.

## A.2 Encoding spin in vibrational states

In a second scheme, we replace the ensemble of tilted ladder systems with tilted chains where the spin is now encoded in the lowest two vibrational levels of the axial lattice. The effective transverse field can be achieved in this case using a Raman laser. Restriction to the lowest two vibrational levels can be achieved by utilizing anharmonicity of the onsite potential. The nearest neighbour spin interaction is again obtained from a superexchange mechanism. In this case, the difference in the

interaction energy for different nearest neighbour configurations is a consequence of the dependence of the Wannier function overlap integrals on the vibrational level of the atoms. There are three possible interaction energies  $U_{00}$ ,  $U_{11}$  and  $U_{01} = U_{10}$  where the indices denote the lowest two vibrational levels and

$$U_{ij} = \frac{4\pi\hbar^2 a_s}{m} \int \alpha |\psi_i(\mathbf{r})|^2 |\psi_j(\mathbf{r})|^2 d\mathbf{r}.$$
 (A.2)

Here  $\psi_i(\mathbf{r})$  is a wavefunction of an atom that is in the ground vibrational state of the 2D lattice and in the *i*th vibrational state of the axial lattice, and  $\alpha$  is a degeneracy factor ( $\alpha = 2$  for  $i \neq j$  and  $\alpha = 1$  otherwise.) The axial lattice wavefunctions are those of a quantum harmonic oscillator, which gives  $U_{11}/U_{00} = 3/4$  and  $U_{01} = U_{00}$ . The matrix elements connecting the states are

$$\Delta E_{ii} = -\frac{4t^2 U_{ii}}{U_{ii}^2 - \Delta^2} \tag{A.3}$$

$$\Delta E_{01} = \Omega_{01,10} = -\frac{2t^2 U_{01}}{U_{01}^2 - \Delta^2} \tag{A.4}$$

with  $i \in \{0, 1\}$  in the first equation,  $\Delta E$  denotes an energy shift and  $\Omega_{01,10}$  allows Rabi flopping between  $|01\rangle$  and  $|10\rangle$ . The resulting Hamiltonian can be written in the form of an anisotropic Heisenberg model in transverse and longitudinal fields

$$H = \sum_{i} -J_{z} S_{z}^{i} S_{z}^{i+1} - J_{\perp} S_{\perp}^{i} S_{\perp}^{i+1} - h_{x} S_{x}^{i} - h_{z} S_{z}^{i}$$
(A.5)

with  $h_z = \frac{1}{2}(\Delta E_{11} - \Delta E_{00}), J_{\perp} = -2\Delta E_{01}$  and  $J_z = 2(\Delta E_{01} - \Delta E_{00} - h_z)$ . The coupling parameter ratios are shown in Figure A.2. The perturbation theory used to

obtain these parameters is only valid away from the resonances at  $\Delta = U_{00}, U_{11}$  and  $U_{01}$ .

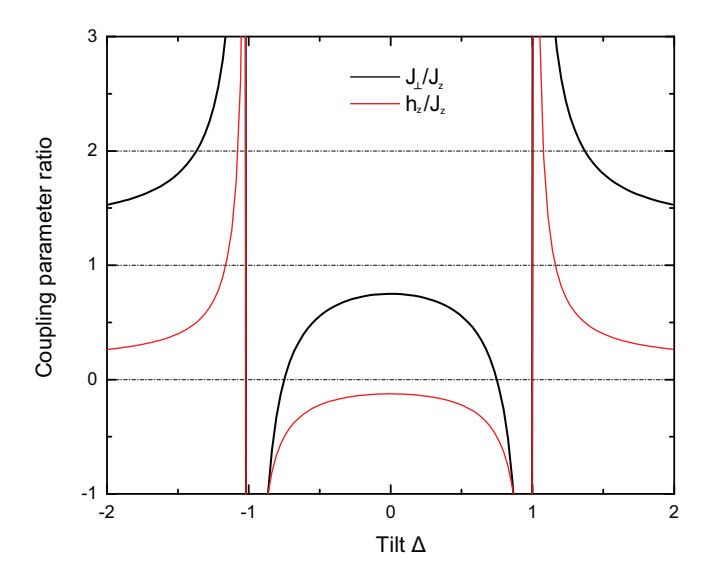


Figure A.2: Dependence of the anisotropic Heisenberg model parameters on the lattice tilt. The black (red) curve is the ratio of  $J_{\perp}$  ( $h_z$ ) to  $J_z$ . These ratios are only valid in the perturbative regime away from any resonances. The transverse field  $h_x$  is controlled by the Raman coupling strength.